Montanuniversität Leoben

Characterization of β-solidifying γ-TiAl alloy variants using advanced in- and ex-situ investigation methods

by

Laura Melanie Drössler

This thesis was conducted at the Department of Physical Metallurgy and Materials Testing at the Montanuniversität Leoben.

Leoben, October 2008

Affidavit

I declare in lieu of oath, that I wrote this thesis and performed the associated research myself, using only the literature cited in this volume.

Leoben, October 2008 Laura Melanie Drössler

Acknowledgements

In the first place I would like to express my gratitude to Prof. Helmut Clemens, Head of Department of Physical Metallurgy and Materials Testing at the Montanuniversität Leoben, for giving me the great opportunity to write this thesis within his project and under his supervision. I am thankful for his support and encouragement during my work. Our countless discussions and his valuable advice made for a crucial contribution of this thesis.

I would like to thank Prof. Arno Bartels and his PhD student Andreas Stark, Technical University Hamburg-Harburg, for fruitful discussions. Special thanks to Andreas Stark for his general approach and for sharing his experience that helped me with problems in the evaluation of my diffraction patterns.

I would also like to thank Dr. Klaus-Dieter Liss, Australian Nuclear Science and Technology Organisation, for his valuable contribution and stimulating talks during the neutron diffraction experiments.

I am grateful to Dr. Gerald Zickler for the organization of our experiments at the ESRF in Grenoble and the FRM II in Munich and to our local contacts, Dr. Thomas Buslaps and Dr. Markus Hölzel.
This research project has been supported by the European Commission under the 6th Framework Programme through the Key Action: Strengthening the European Research Area, Research Infrastructures. Contract n°: RII3-CT-2003-505925.

I am thankful to Thomas Schmölzer who supported me not only as a colleague but also as a friend.

Thank you to my colleagues at the Department, who helped me throughout the time of my work and created a pleasant working atmosphere.

My particular gratitude is to my family for their constant support. My dad for always believing in me, my grandparents for creating a second home for me, and Luis, who makes me find new strength.

Table of Contents

Abbreviations III

1 Introduction 1

2 The TNM Alloy System 3
2.1 Basics 3
2.2 TNM Alloy Variants A, B and C 6
2.3 TNM-B1 Alloy 8
2.3.1 Cellular Reaction (Discontinuous Precipitation) 9
2.4 Experimental 11
2.5 Results and Discussion 12
2.5.1 Alloys A, B and C 12

3 Synchrotron and Neutron Diffraction in Materials Science 26
3.1 Historical Review of Synchrotron Radiation 26
3.2 Physics of Photons and Neutrons 27
3.3 Interactions 28
3.3.1 Photons 28
3.3.2 Neutrons 29
3.4 The Generation of Synchrotron Radiation 30
3.5 The Generation of Neutron Radiation 32
3.5.1 Nuclear Reactors 32
3.5.2 Spallation Sources 32
3.6 The Rietveld Method 33
3.6.1 Quantitative Phase Analysis by the Rietveld Method 34
3.7 TNM Structure Factor Considerations 35
3.8 Experimental 36
3.8.1 Synchrotron 36
3.8.2 Neutrons 37
3.8.3 Material and Temperature Programs 37
3.9 Results and Discussion 39
3.9.1 Synchrotron Data – Alloys A, B and C 39
3.9.2 Neutron Data – Alloy TNM-B1 50
3.9.3 Comparison of Synchrotron and Neutron Data 52

4 Electron Backscatter Diffraction for Orientation Analysis 55
4.1 Formation of Kikuchi Lines 55
4.2 Comparison of Kikuchi Patterns in TEM and SEM 59
4.3 Evaluation of EBSD Patterns 59
4.4 Experimental Setup in the SEM 60
4.5 Operating Conditions 61

4.5.1 Material and Sample Preparation 61
4.5.2 SEM Geometry 62
4.5.3 Microscope Setting 62
4.6 Lamellar Structure Formation in TiAl 63
4.7 EBSD Experimental Setup and Sample Preparation 64
4.8 Results and Discussion 65

5 Microstructure and Properties 72

6 Summary and Outlook 78

7 References 81

Abbreviations

AC	air cooling
BSE	backscattered electron
CCD	charge coupled device
DSC	differential scanning calorimetry
DP	discontinuous precipitation
EBSD	electron backscatter diffraction
ESRF	European Synchrotron Radiation Facility, Grenoble, France
FC	furnace cooling
FRM II	Forschungsneutronenquelle Heinz Maier-Leibnitz, Munich, Germany
FWHM	full width at half maximum
SEM	scanning electron microscope
T_{α}	α-transus temperature [°C]
TEM	transmission electron microscope
T_{eu}	eutectoid temperature [°C]
TNM	titanium aluminide alloy with high Nb and Mo content
VAR	vacuum arc remelting
WQ	water quenching
XRD	X-ray diffraction
XRF	X-ray fluorescence

1 Introduction

Research interests on intermetallic γ-TiAl based alloys have been increasing over the last decades. γ-TiAl alloys are light-weight structure materials that can be applied up to operating conditions of 800°C. Due to their low density of about 4 g/cm^3 and high specific strength they are promising candidates for high temperature applications in aeronautics and the automotive industry. Apart from their excellent high temperature properties TiAl alloys are very brittle at room temperature [1,2]. Peritectic alloys that solidify via the hexagonal α-phase are prone to segregations and exhibit local differences in microstructure and mechanical properties [3].

In an attempt to develop a γ-TiAl alloy that exhibits a homogeneous microstructure and can be forged at nearly conventional conditions, a new alloy was designed by Clemens et al. showing a baseline composition of Ti-(42-45)Al-5Nb-1Mo-0.1B [2], called TNM-alloy. Nb is a β-stabilizing element that retards diffusion processes and reduces the stacking fault energy in γ-TiAl. Mo also slows down diffusion, it has a higher partition coefficient than Nb and is an even stronger β-stabilizer. The formation of borides is an effective inhibitor of grain coarsening. Due to their solidification via the β-phase TNM-alloys exhibit very homogeneous microstructures [2].

The bcc lattice of the β-phase provides sufficient slip systems and facilitates the deformability at elevated temperatures. Through elaborate heat treatments the β-phase content is adjustable and can almost entirely be removed for the application. Thermodynamic calculations were conducted by Chladil [3] to predict the phase contents at thermodynamic equilibrium depending on temperature. In the present work TNM alloys with Al-contents between 42 and 43 at% were investigated using several methods. Quantitative phase analysis of samples after different heat treatments was carried out on scanning electron microscope (SEM) micrographs. High temperature in-situ synchrotron measurements were conducted to determine the composition of the microstructure depending on temperature. The results were evaluated using the Rietveld method and compared to the results obtained from the quantitative analysis of the micrographs and those calculated by Chladil [3]. To determine the ordering temperatures of the α- and β-phases, neutron diffraction experiments were performed at several temperatures.

For a better understanding of the formation and transformation of the microstructure EBSD measurements were conducted and analyzed with respect to orientation relationships and microstructure stability.

TEM investigations and hardness measurements were carried out in order to describe the formation of primary γ-lamellae from supersaturated α_2-grains as a function of temperature and to relate the interlamellar spacing to mechanical properties.

2 The TNM Alloy System

2.1 Basics

In order to increase the workability of intermetallic TiAl-alloys for aero-engine and automotive applications without having to sacrifice their excellent mechanical properties numerous investigations have been conducted [2,4]. Previously developed high Nb containing alloys show good oxidation resistance and improved ductility and strength compared to alloys with low Nb content [3,5]. However, conventional TiAl alloys with high Nb contents are prone to segregations. Their anisotropic microstructure and texture can be ascribed to the peritectic solidification path via the hexagonal α-phase [4,6,7]. Generally, a higher homogeneity can be achieved with alloys that solidify through the body centered cubic β-phase, thereby avoiding the peritectic reaction [6,7]. The alloys investigated in this work have been developed by Clemens et al. [2] and show the following solidification path

$$L \rightarrow L + \beta \rightarrow \beta \rightarrow .. \qquad \text{(Equ. 1)}$$

instead of the peritectic solidification

$$L \rightarrow L + \beta \rightarrow \alpha \rightarrow .. \qquad \text{(Equ. 2)}$$

Figure 1 shows the quasi binary phase diagram for this new alloy with a composition of Ti-(30-55) Al-4 Nb-1 Mo-0.1 B (at%) [8].

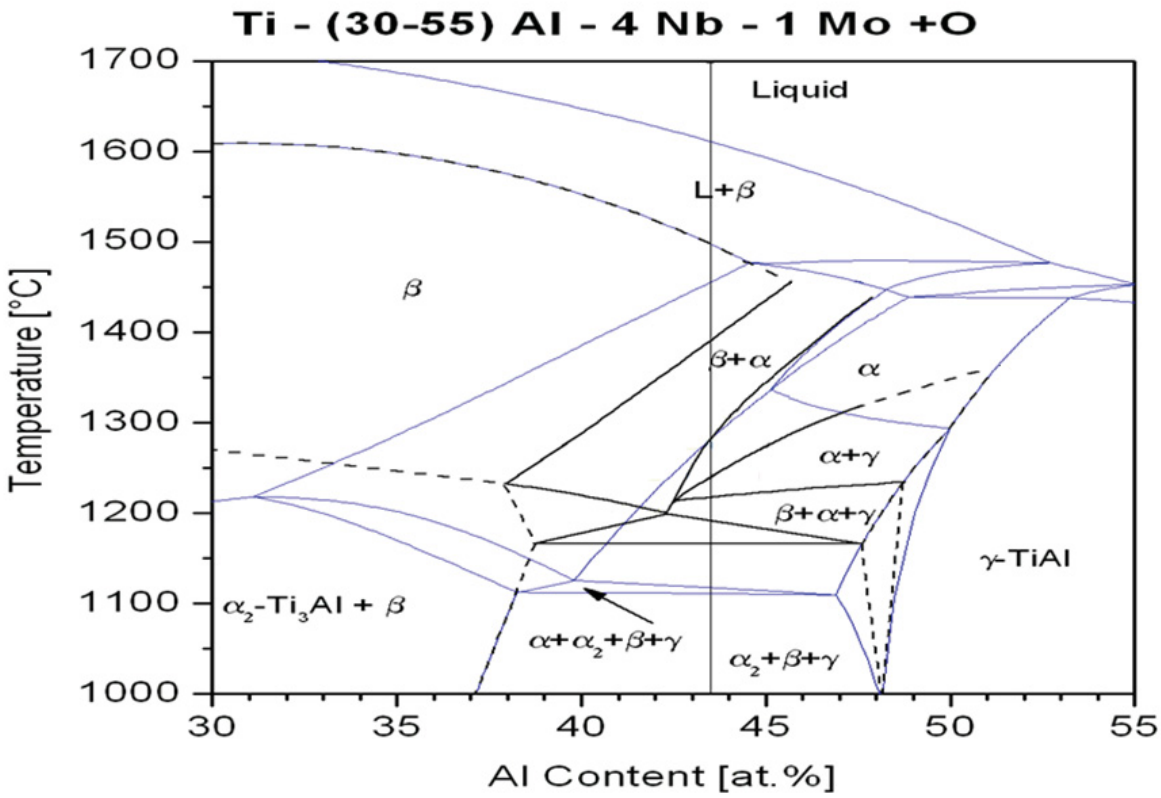

Fig. 1: Phase diagram for the TiAl alloy with composition Ti-(30-55)Al-4Nb-1Mo. The blue lines show the calculated diagram, the black lines indicate the experimentally determined phase diagram according to Böck [8].

The blue lines show the phase diagram published by Clemens et al. [9]. The black and dashed lines represent the corrected data and the extrapolated values, respectively, as experimentally found by Böck through DSC measurements [8]. The β-phase is stabilized by the alloying elements obviating a peritectic solidification via the α-phase. The solidification path via the β-phase is marked by a vertical line for the relevant composition investigated in this diploma thesis.

Nb is added as alloying element to reduce the stacking fault energy in γ-TiAl and to considerably increase the activation energy of diffusion [2]. The existence of a second phase inhibits grain growth. Therefore, the α-grains emerging from the β-phase are stabilized against grain growth in this two-phase region [2,4]. Due to its high partition coefficient Mo exhibits an even stronger β-stabilizing effect than Nb [3]. The β-phase is the most ductile component of the TNM alloy and important for the hot-workability of the material. A small amount of B effectuates the precipitation of borides that are known to be grain refining agents and restrict grain growth upon heating due to the Zener-drag effect [1]. Additionally, borides favor the α + γ-microstructure over massive α → γ-transformation through heterogeneous nucleation of γ-lamellae [4].

The disordered β-phase that is hence stabilized at elevated temperatures offers a sufficient number of slip systems and improves the formability of the material [7 and references therein].
Three intermetallic phases occur in this alloy system, namely

- The γ-TiAl phase with a tetragonal $L1_0$-structure,
- The α_2-Ti_3Al with a hexagonal $D0_{19}$-structure,

both are present in all γ-based titanium aluminides,

- The β_O-TiAl phase, which is the ordered modification (B1-structure) of the unordered body centered cubic β-phase.

The disordered variant of α_2, i.e. the α-phase, is present at temperatures above the eutectoid temperature T_{eu} at ca. 1170°C (see Fig. 1). The ratio of the lattice parameters c/a in the tetragonal γ-TiAl is very close to 1 and, therefore, apart from its chemical order, the γ-phase differs only insignificantly from a face centered cubic structure [10]. The temperature where γ first precipitates from the α-phase upon cooling will be referred to as T_α. In lamellar colonies consisting of α_2- and γ-lamellae the two phases show the Blackburn orientation relationship [11]:

$$(111)\gamma \parallel (0001)\alpha_2 \quad \text{and} \quad [-101]\gamma \parallel [11\text{-}20]\alpha_2. \qquad \text{(Equ. 3)}$$

Due to the two main alloying elements this new alloy was named TNM, where T stands for TiAl, N for Nb and M for Mo. Consequently, the variant additionally alloyed with B was named TNM-B1.

2.2 TNM Alloy Variants A, B and C

Thermodynamic calculations have been conducted by Chladil [3] for alloys similar to the TNM-B1 alloy. In the present work those alloys are termed A, B and C. Buttons of 150 g were produced by GfE (Nuremberg, Germany) in a vacuum arc remelting process (VAR) and were remelted three times to assure adequate chemical homogeneity. The manufacturing process is described in detail by Böck [8]. The nominal compositions of the three alloys are compared in Table 1.

Tab. 1: Nominal chemical compositions of alloys A, B and C

	Al [at%]	Nb [at%]	Mo [at%]	B [at%]
A	43	4	1	0.1
B	43	4	1.5	0.1
C	43	5	1	0.1

Alloy A has a nominal composition of Ti–43Al–4Nb–1Mo–0.1B (at%) very similar to the TNM-B1 alloy, the only difference being its Al content of 43 at%, which is 43.9 at% in TNM-B1. For all three alloys A, B and C the Al content is kept constant at 43 at% whereas the Nb and Mo contents vary for alloys B and C. Alloy B has an increased Mo content of 1.5 at% and is expected to exhibit the largest phase fraction of β, since the β-stabilizing effects of Mo are twice as strong as those of Nb [3]. With 5 at% Nb, alloy C is predicted to lie between alloy A and B in terms of its β-phase fraction. Figure 2 shows the results of the thermodynamic calculations conducted via the CALPHAD (Calculation of Phase Diagrams) method using a commercially available database [12].

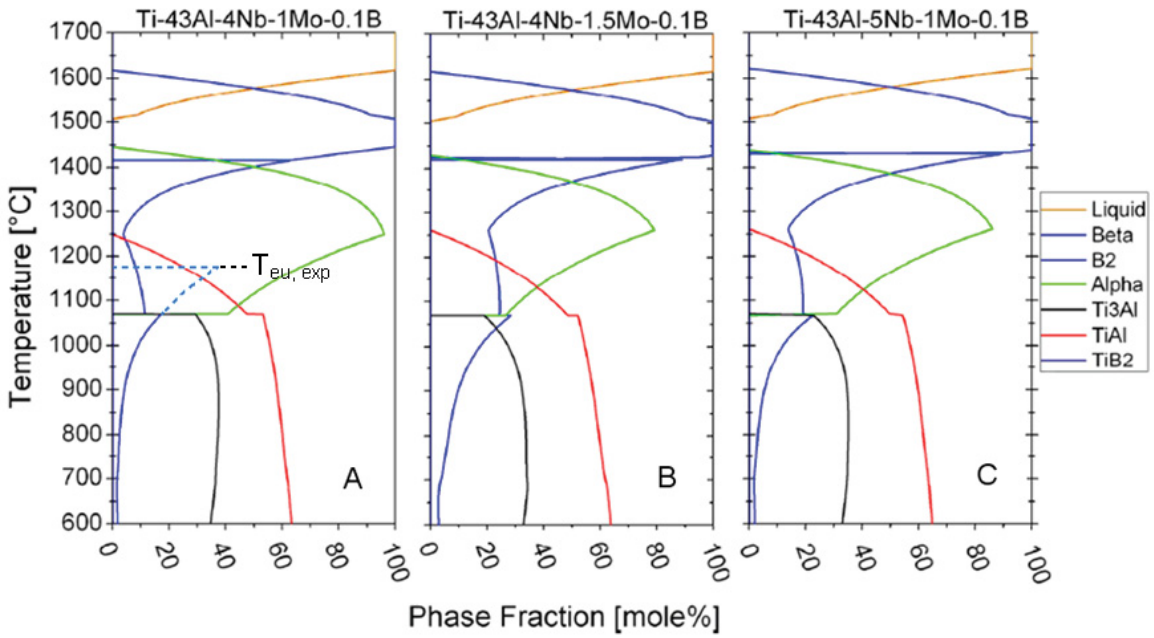

Fig. 2: Thermodynamic calculations of the phase fractions as a function of temperature for the alloys A, B and C that exhibit different contents of β-stabilizing elements. In the phase diagram of alloy A the experimentally determined T_{eu} is indicated. Additionally, the possible course of the β-phase is shown [3].

It can be seen from the calculations that the overall β-content in alloy C is predicted to be higher than in alloy A and the β-content in alloy B is even higher. All three alloys show a minimum in β-content at T_α with the most pronounced minimum found in alloy A. Above T_α the β-phase content increases rapidly with temperature. Below T_α the β-content increases slightly towards the eutectoid temperature T_{eu}. Below T_{eu} the β-content is reduced for all three alloying variants. This strong temperature dependence enables an adjustment of the β-phase fraction through adequate heat treatments. For all three alloys the $\beta \rightarrow \beta_O$ ordering occurs at about 1410°C, T_α is at ca. 1250°C and T_{eu} at ca. 1070°C. T_α calculated via CALPHAD was proven to be quite accurate, whereas T_{eu} was found to be at 1176°C in DSC measurements conducted by Chladil [3] on an alloy exhibiting a composition comparable to alloy A. Since the Thermocalc database showed difficulties handling high Nb and Mo containing alloys, corrected values using a modified database were calculated resulting in higher temperatures for all transitions:

- T_{eu}=1117°C
- T_α=1264°C and
- T_β=1445°C [3].

2.3 TNM-B1 Alloy

The investigated material emanates from heat 73300 and was designated FD_MTU03 by the manufacturer. It was produced by a VAR process and remelted three times to assure an adequate chemical homogeneity [3]. The material was hot extruded at 1230°C from a diameter of 200 mm down to 54 mm. A subsequent stress relieve heat treatment was performed at 980°C for 4 h under Ar atmosphere. After turning the extruded rod to a diameter of 40 mm it was side pressed to 20 mm in a single forging step. Its chemical composition was determined to 51,19Ti–43.92(+/-0.3)Al–3.8Nb–1.01Mo–0.09 B (at%) as the average value of four X-ray fluorescence (XRF) analyses. This material will hereafter be referred to as TNM-B1.

The material's microstructural evolution is similar to those of the ABC alloys and also shows an adjustable β-phase fraction. Short term heat treatments of 1 h conducted by Wallgram [13] show a β-minimum at 1260°C and 1240°C for alloys containing 43.9 at% and 43.4 at% Al, respectively. Figure 3 shows the β-phase fraction dependent on temperature for those two TNM alloys. These results are in accordance with the calculated and measured phase diagram [8] showing an increase of T_α with increasing Al content (see Fig. 1).

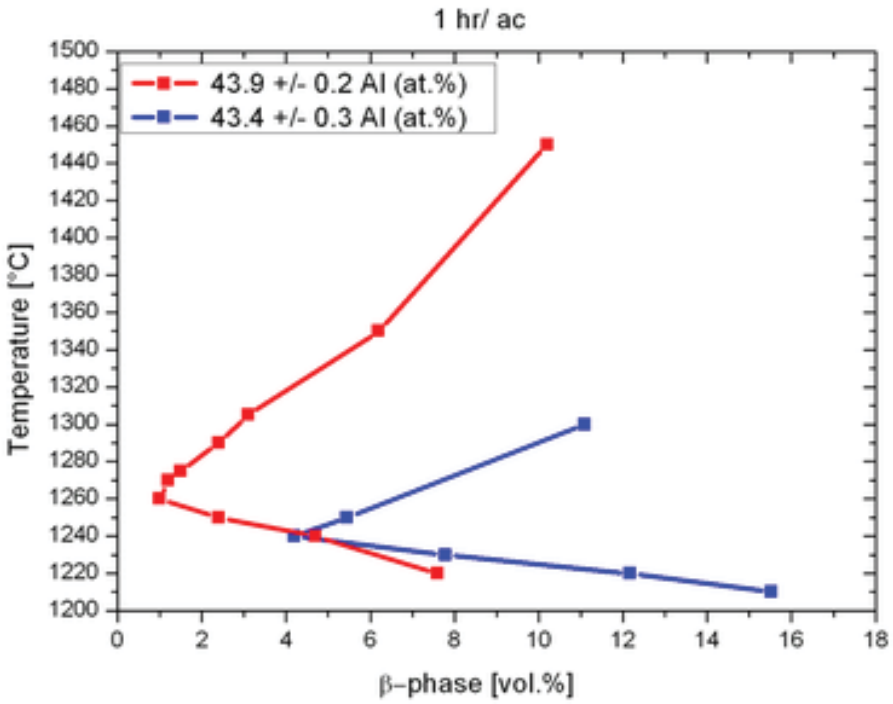

Fig. 3: Dependence of the β-phase fraction after short term heat treatments (1 h) performed on TNM-alloys containing 43.9 at% and 43.4 at% Al. After annealing the samples were air cooled to room temperature [13].

2.3.1 Cellular Reaction (Discontinuous Precipitation)

Due to the low energy of the semicoherent $(0001)_{\alpha_2} / \{111\}_{\gamma}$ interfaces the lamellar colonies in TiAl alloys are stable [14]. Those primary lamellae that form upon cooling from the α-phase region, i.e. below T_α, exhibit extremely flat interfaces. Their diffusion controlled thickening slows down with the decrease of supersaturation as well as an increase of cooling rate and is eventually brought to completion.

Since the solute flow between the highly coherent lamellar interfaces is very difficult, diffusion-assisted growth of the lamellae is widely suppressed for a specimen quenched from the α-single phase region and subsequently aged at a temperature below T_{eu}. Therefore, a different process occurs in this microstructure resulting in the coarsening of the lamellae [15]. Here, the formation of the very fine primary γ-lamellae is a precipitation process in the supersaturated α_2-matrix. Note that the $\alpha \rightarrow \alpha_2$ ordering reaction cannot be suppressed by quenching [16].

At the grain boundaries, consisting of the edges of α_2- and γ-lamellae, the solubility according to the Gibbs-Thomson relationship is generally high [15]. At high annealing or service temperature, however, the lamellar colony boundaries are sufficiently mobile, so that by their migration across the lamellar colony, the high density of interfaces is reduced by grain boundary diffusion along the transformation front. The microstructure is hence transformed into a coarser lamellar structure [14]. The resulting secondary lamellae remain in the initial grain and their orientation and orientation relationship is maintained, although the lamellar interfaces are much less regular [15]. This reaction has been described in several publications for TiAl [14,15] and other alloys [17,18] and is called cellular reaction, discontinuous precipitation or discontinuous coarsening, because the composition of the matrix changes discontinuously as the cell front passes [19].

The grain boundary becomes sinuous during discontinuous precipitation, thus increasing the total grain boundary energy. This can be compensated for by the formation of a coarser lamellar structure which reduces the number of interfaces. It has been observed that the finer the initial lamellar structure, the coarser the secondary lamellar structure becomes, which suggests the influence of interface energy as a driving force of discontinuous coarsening [15,20]. This influence has been quantified by Talach-Dumanska et al. [18]:

$$\Delta G = \frac{2\sigma\nu}{\lambda} \qquad \text{(Equ. 4)}$$

with ΔG being the Gibbs free energy, σ the interfacial free energy per unit area of the lamellae, v the molar volume of the colony and λ the interlamellar spacing. For

materials quenched from the α-phase field that are far from thermodynamic equilibrium, the contribution from the chemical disequilibrium may become more important as demonstrated in Figure 4.

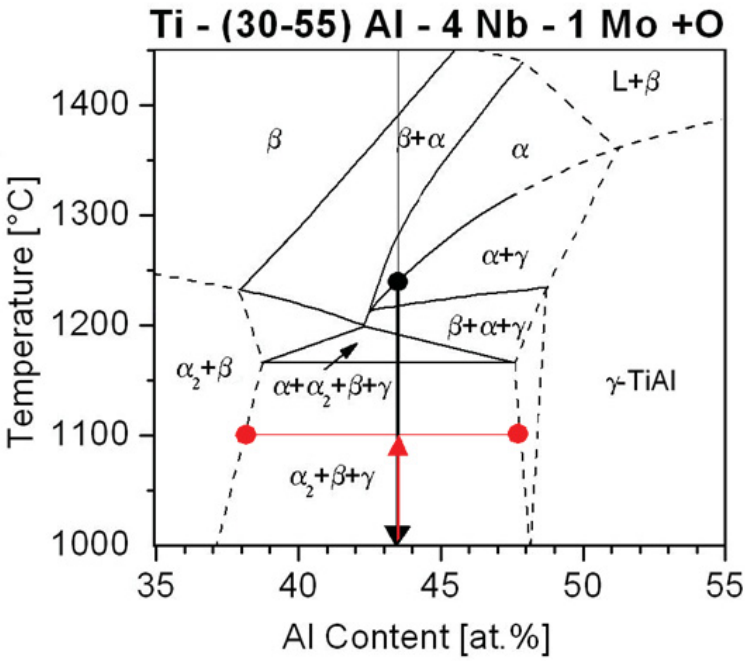

Fig. 4: Phase diagram indicating the first heat treatment step at 1230°C (black) und the second heat treatment step at 1100°C (red) showing the chemical disequilibrium [8].

During a subsequent heat treatment of the quenched material, the discontinuous reaction can occur almost simultaneously with primary lamellae formation to shift the system closer towards equilibrium [15,20]. It is also suggested by Denquin et al. [15] that the formation of monolithic γ-grains takes place at interfaces and colony boundaries for heat treatments at higher temperatures.

2.4 Experimental

Different heat treatments were performed on all alloys for microstructural investigations using a high temperature chamber furnace RHF 16/15. The goal of this study was an experimental quantification of the β-phase content as a function of the annealing temperature and to investigate the extent of the microstructure transformed via a cellular reaction. The dimensions of the heat treated samples were about 2 x 2 x 3 cm^3. After the heat treatment the specimens were cut in half, mounted in conductive material and grinded and polished for observation in the Scanning Electron Microscope (SEM) using standard metallographic techniques. To visualize the different phases the images were recorded in the backscatter mode. An SEM micrograph of alloy A can be seen in Figure 5.

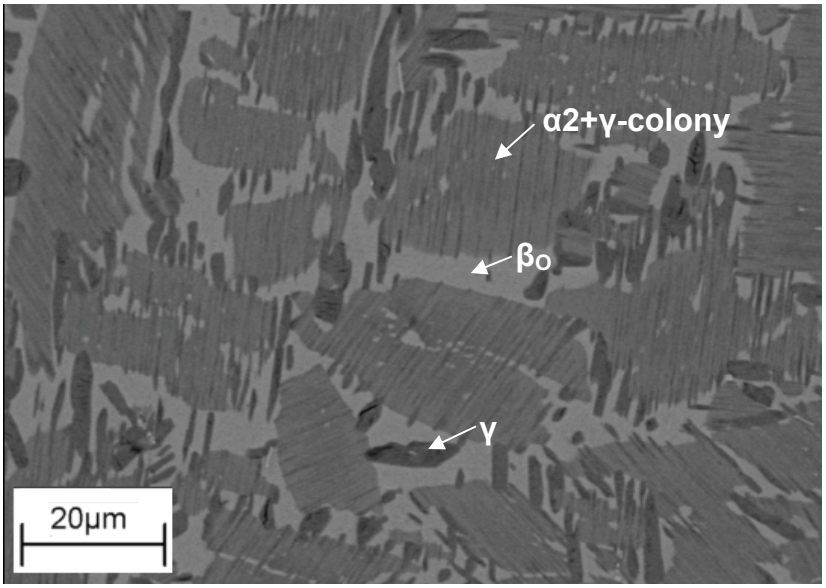

Fig. 5: SEM micrograph of alloy A in backscatter mode. The bright contrast is β, the grey contrast represents α_2+γ-colonies and the dark contrast are γ-grains.

In the phase contrast seen in SEM the phase with the brightest contrast is β, the grey contrast represents α_2+γ-colonies that form upon cooling and the dark grey contrasted phase is γ. The flaws that are present in some of the large γ-grains in the SEM images result from metallographic sample preparation and do not represent micro-cracks. Tables 2 and 3 show the heat treatments conducted for the alloys A, B and C as well as the TNM-B1 alloy. The samples with a two step heat treatment were air cooled (AC) after the first heat treatment and furnace cooled (FC) after the second one. After a one-step heat treatment the samples were water quenched (WQ).

Tab. 2: One- and two-step heat treatments conducted for alloys A, B and C.

1st step				2nd step		
1230°C	1h	AC	+	900°C	6h	FC
1230°C	1h	AC	+	1000°C	6h	FC
				1170°C	1h	WQ
				1270°C	1h	WQ
				1350°C	1h	WQ

Tab. 3: Two-step heat treatments conducted for alloy TNM-B1.

1st step				2nd step		
1230°C	1h	AC	+	900°C	1h	FC
1230°C	1h	AC	+	900°C	10h	FC
1230°C	1h	AC	+	900°C	100h	FC
1230°C	1h	AC	+	1000°C	1h	FC
1230°C	1h	AC	+	1000°C	10h	FC
1230°C	1h	AC	+	1000°C	100h	FC
1230°C	1h	AC	+	1100°C	1h	FC
1230°C	1h	AC	+	1100°C	10h	FC
1230°C	1h	AC	+	1100°C	100h	FC
1230°C	1h	AC				

The images for the extruded material TNM-B1 were recorded in extrusion direction, for the buttons A, B and C in radial direction. The obtained SEM images were evaluated using the software package Analysis by Olympus Soft Imaging Solutions GmbH. The images of the alloys A, B and C were analyzed regarding the volume fraction of the β-phase. For alloy TNM-B1 the images were also investigated with respect to the amount of β-phase and the microstructure transformed via the cellular reaction.

2.5 Results and Discussion

2.5.1 Alloys A, B and C

The heat treatments conducted for the alloys A, B and C are summarized in Table 2. The main emphasis in this investigation was put on the determination of the β-phase volume fraction as a function of temperature. SEM images of the heat treated samples of alloy A are shown in Figure 6.

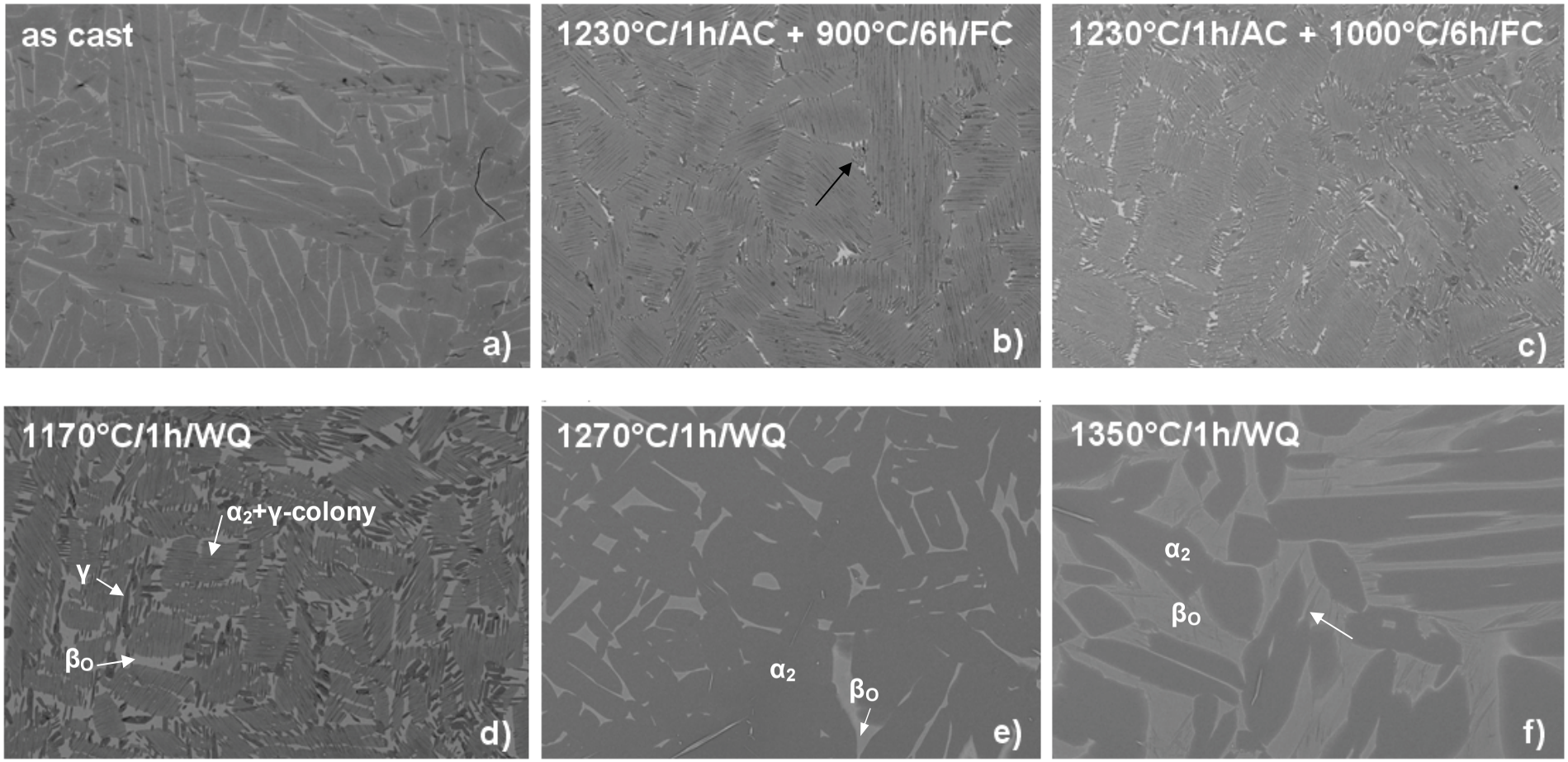

Fig. 6: SEM images (BSE mode) of samples of alloy A after different heat treatments as indicated. The phase with the brightest contrast is β, the grey grains are α_2+γ-colonies that cannot be resolved in the SEM, the dark grey particles are γ-grains.

In the as cast state, shown in Figure 6a, alloy A consists of elongated α_2-grains surrounded by a β_O-seam.
Figure 6b shows the material after a two-step heat treatment at 1230°C for 1 h with following air cooling and annealing at 900°C for 6 h and furnace cooling. The first heat treatment step in the temperature region of the β-minimum (see Fig. 2) reduces the fraction of β in the microstructure. The γ-grains almost completely disappear and γ-lamellae form within the α-grains during cooling. The α-phase that remains in the colonies orders to α_2 at the eutectoid temperature T_{eu}.
In the second step the material is heated to a temperature below T_{eu}, hence staying in the $\alpha_2+\gamma+\beta_O$-phase field (see Fig. 1). Coarsening of the γ-lamellae occurs in order to increase the γ-phase fraction to approach thermodynamic equilibrium. The beginning of a cellular reaction can be observed at some of the colony boundaries as indicated by the black arrow in Figure 6b. This process will be discussed in detail on alloy TNM-B1 in the following section.
For Figure 6c the first heat treatment step was the same as for Figure 6b. However, the second step was performed at 1000°C for 6 h with subsequent furnace cooling. It can be seen from the SEM image that a higher fraction of the lamellar microstructure has decomposed via a cellular reaction during the second heat treatment step.
Figures 6d, e and f show the material after 1 h one-step heat treatments at different annealing temperatures with subsequent water quenching to analyze the trend in the progression of the β-phase content with temperature. The first heat treatment (see Fig. 6d) was conducted at 1170°C, close to the eutectoid temperature of 1176°C as experimentally determined by Chaldil [3]. As expected, the β_O-phase fraction is higher than after the previously discussed heat treatments. The β_O-phase is arranged along the lamellar colonies. The γ-lamellae have coarsened and additional γ-grains can be found at the grain boundaries and within the β_O-grains. Figure 6e shows the material after heating to 1270°C, close to T_α and the β-minimum. The microstructure exclusively consists of α- and β_O-grains. At this temperature γ is completely dissolved. As expected for annealing at T_α, α is the predominant phase, seamed by β-grains. Upon cooling α orders to α_2 so that the grains seen in the SEM image are ordered α_2-grains. Above T_α the β-volume fraction increases, which can be seen in Figure 6f. The lath shaped structures within the β-grains represent α-phase (α_2 at room temperature), which is indicated by laths connected to the surrounding α-grains (see arrow Fig. 6f).

A comparison of a two-step and a one-step heat treatment for the three alloys can be seen in Figure 7.

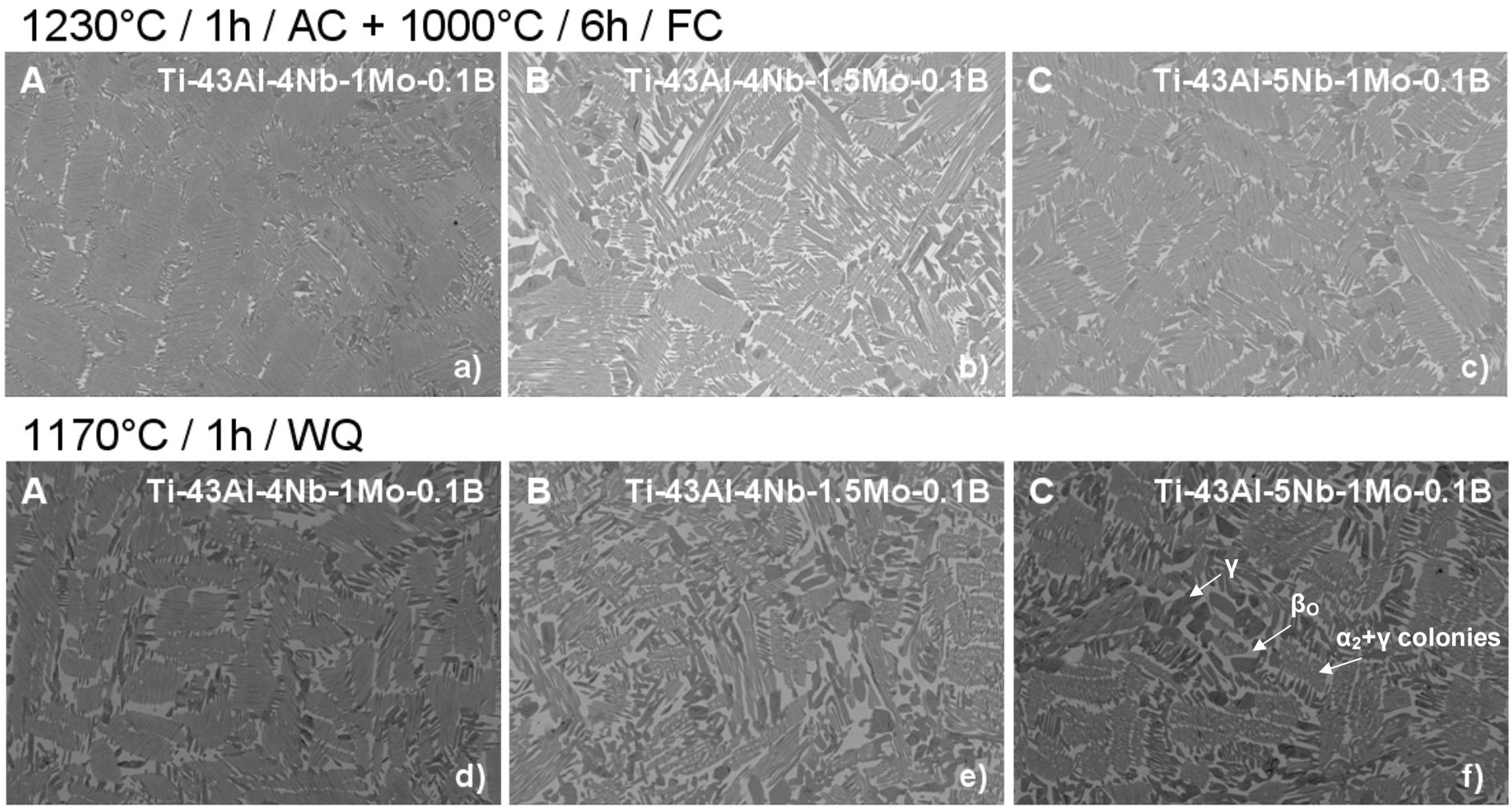

Fig. 7: Comparison of a two-step and a one-step heat treatment for the alloys A, B and C. The β-content is the smallest for alloy A, higher for alloy C and the highest for alloy B after both heat treatments. The phase with the brightest contrast is β, the grey grains are α_2+γ-colonies, the dark grey particles are γ-grains. All SEM images were taken is BSE mode.

Figures 7a, b and c compare one of the two-step heat treatments already discussed for alloy A in Figure 6c. After a first step at 1230°C for 1 h with subsequent air cooling the samples were heated to 1000°C for 6 h followed by furnace cooling. Alloy C, which contains 1 at% more Nb than alloy A, shows a higher β-content on the expense of lamellar colonies. The β-content is the highest for alloy B, that contains the most of the strongly β-stabilizing element Mo. The same tendency can be observed for a heat treatment at 1170°C for 1 h with subsequent water quenching, shown in Figures 7d, e and f. β also starts to form within the colonies and a higher amount of γ-grains can be found for variants C and B, all at the expense of the lamellar colonies. From Figure 7 it is clearly evidenced that the volume fraction of the β-phase is higher when annealing is conducted at 1170°C than at 1000°C. This result is in agreement with the data predicted from thermodynamic calculations, but only if the course of the β-phase is extrapolated according to Figure 2 (alloy A).
In order to quantitatively evaluate the progression of the β-phase fraction in the three discussed alloys, metallographic phase analyses were performed using the software package Analysis. The results are shown in Figure 8.

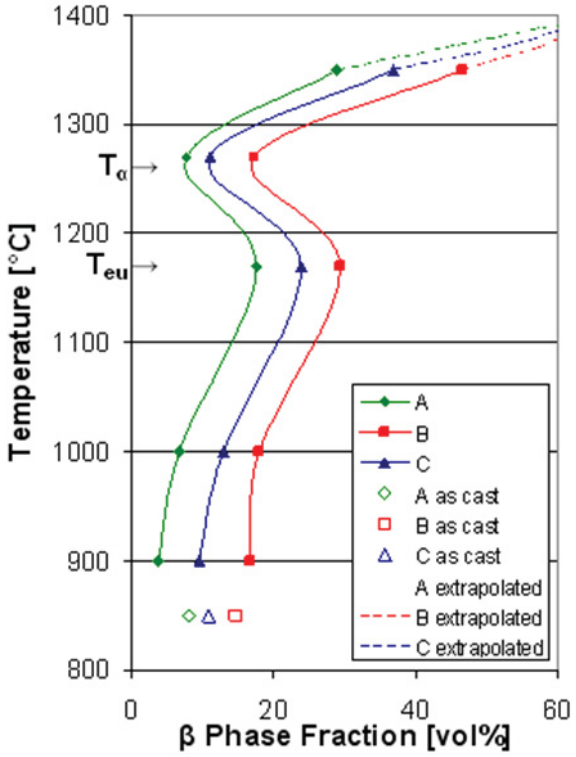

Fig. 8: Volume fractions of the β-phase for alloys A, B and C as a function of temperature, experimentally determined by applying quantitative phase analysis on the SEM images using the software package Analysis. The T_{eu} and T_α temperatures for an alloy similar to A as determined by DSC are indicated by arrows.

A clear tendency for higher β-contents in alloy C than in A and the highest β-contents in alloy B is confirmed by those results. Compared to the thermodynamic calculations in Figure 2 the same trend can be observed concerning the β-maximum around T_{eu} and the minimum around T_{α}, calculated at 1117°C and 1264°C, respectively by Chladil [3]. The absolute temperature value for T_{eu} seems to be higher in the experimental data which is in agreement with DSC measurements conducted on an alloy with a composition similar to that of alloy A, as indicated by the arrows. Since only very few data points could be obtained for the experimental curve it is not possible at this point to draw a conclusion about the exact temperature of T_{eu}. Further investigations will be documented in this work to find the accurate value.

2.5.2 TNM-B1

The two-step heat treatments listed in Table 3 were conducted on alloy TNM-B1. The first heat treatment is performed to minimize the amount of β-phase by heating the specimens to 1230°C for 1 h with subsequent air cooling. The second steps of the heat treatments were performed at 900°C, 1000°C and 1100°C for 1, 10 and 100 h, respectively. During the second heat treatment a decomposition of the microstructure in form of a cellular reaction occurs (see section 2.3.1).
An example of a β-grain decomposing into β and γ and an α_2+γ-colony dissolving into α_2, γ and β during the second heat treatment step can be seen in Figure 9 as observed by Wallgram [13].

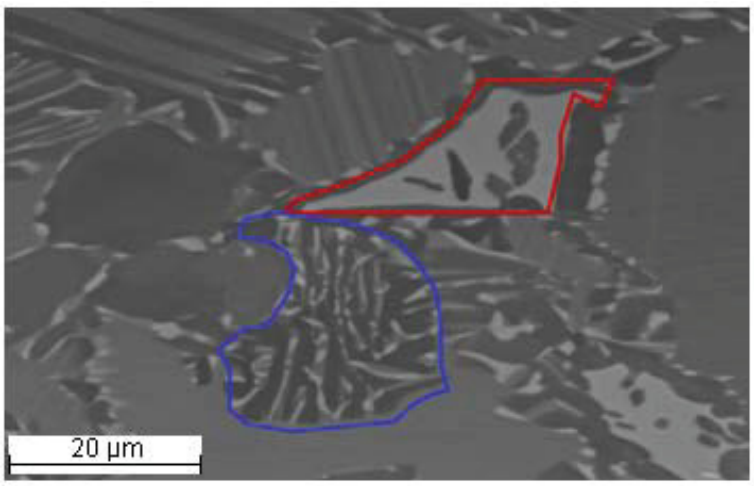

Fig. 9: Decay of a β-grain into β and γ (red) and cellular decomposition of a lamellar colony (blue) during a two step heat treatment conducted on alloy TMB-B1. SEM image taken in BSE mode [13].

In-situ experiments performed by Liss et al. [21] show the beginning of the discontinuous precipitation for a Ti-45Al-7.5Nb sample previously quenched from the α-phase field. The images were recorded via laser scanning confocal microscopy. Upon heating, discontinuous coarsening was triggered at 1100°C. Figure 10 shows micrographs of the in-situ experiment. The start of the cellular reaction is elevated to higher temperatures than observed in the heat treatments (Fig. 6b), which can be ascribed to the finite heating rate and is indicated by an arrow in Figure 10. Although the composition of this alloy deviates from the investigated one, a comparable decomposition behavior is expected.

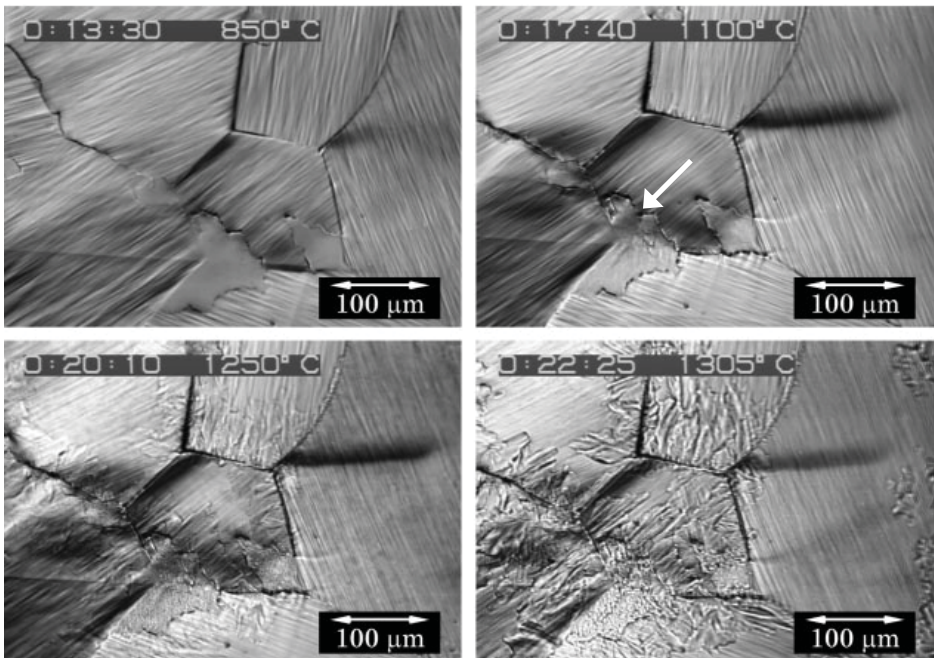

Fig. 10: Micrographs of a Ti-45Al-7.5Nb alloy from in-situ experiments recorded via laser scanning confocal microscopy. The discontinuous precipitation is triggered at 1100°C as indicated by the arrow [21].

A micrograph of the as-forged state of the TNM-B1 material is shown in Figure 11. A fair amount of secondary α_2- and γ-lamellae can be observed that were formed during forging. Figure 11 represents the prevailing microstructure on which the various two-step heat treatments were conducted.

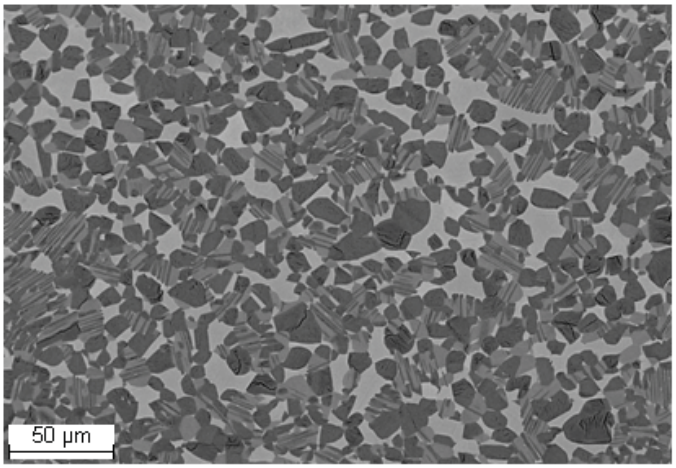

Fig. 11: As forged microstructure of the TNM-B1 alloy. SEM image taken in BSE mode.

Most of those secondary lamellae dissolve upon the first heat treatment step conducted at 1230°C, close to T_α, with subsequent air cooling (see Figs. 12a, 13a and 14a).

Figures 12, 13 and 14 show SEM images for TNM-B1 heat treated at 900°C, 1000°C and 1100°C, respectively. After the second heat treatment step the specimens were furnace cooled to room temperature.

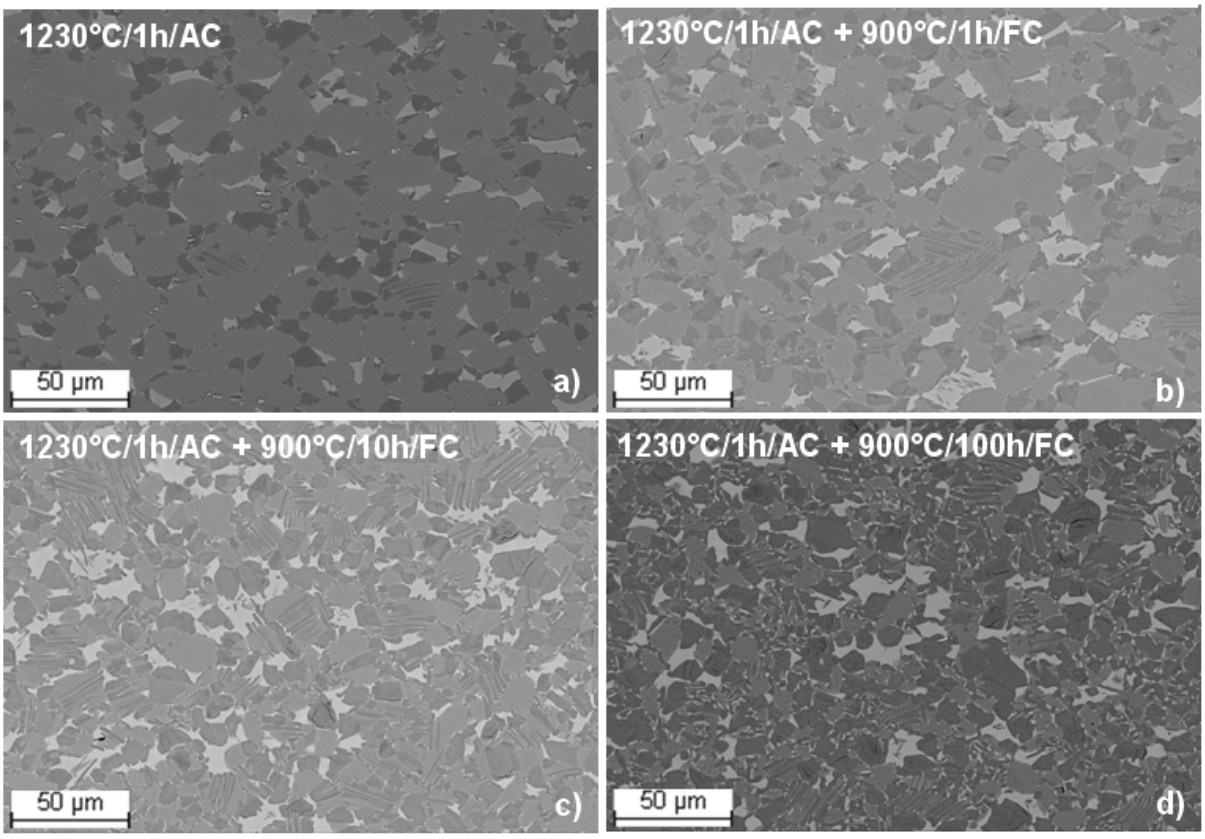

Fig. 12: SEM-BSE images of TNM-B1 after two-step heat treatments. The second annealing step is conducted at 900°C. The holding time varies from 1 to 100 h, followed by furnace cooling.

Figure 12a shows the microstructure in the initial state after the first heat treatment. The microstructure rapidly cooled from 1230°C contains only small amounts of γ and β. TEM investigations showed that in this state only few very fine γ-lamellae have precipitated in the α_2-matrix during air cooling. A few grains already show coarse α_2+γ-lamellae from a discontinuous precipitation at high temperatures that occurs in order to approach the thermodynamic equilibrium by formation of γ-phase.
Figure 12b shows the material after the second heat treatment at 900°C for 1 h. Primary γ-lamellae precipitate within the supersaturated α_2-grains upon heating. Since these γ-lamellae form at temperatures below T_{eu} they are extremely fine. Extremely fine primary γ-laths, however, result in a very high density of interfaces and thus, along with the chemical disequilibrium represent the driving force for a discontinuous precipitation. The SEM image (Fig. 12b) shows the onset of the discontinuous precipitation at many colony boundaries. Also a decomposition of the β-grains is triggered by the precipitation of γ-phase inside the β-grains. Those precipitation reactions increase the γ-content in the sample and shift the material's phase composition towards the thermodynamic equilibrium at 900°C. After 10 h at 900°C, as displayed in Figure 12c, the percentage of former colonies transformed via the cellular reaction has increased considerably. In order to approach the thermodynamic equilibrium at 900°C the β-content also has to be increased and thus β precipitates along with γ during discontinuous coarsening. In this stadium, and even better after 100 h at the same temperature (Fig. 12d), it can be observed that the secondary γ-lamellae grow into directions other than that parallel to the primary lamellae. This can be explained by the possibility of the γ-lamellae to grow along the four {111} tetrahedron planes, whereas only one of them is aligned parallel to the {0001} basal plane of the α_2-matrix [22].

The microstructures resulting from the heat treatment of TNM-B1 at 1000°C are displayed in Figure 13.

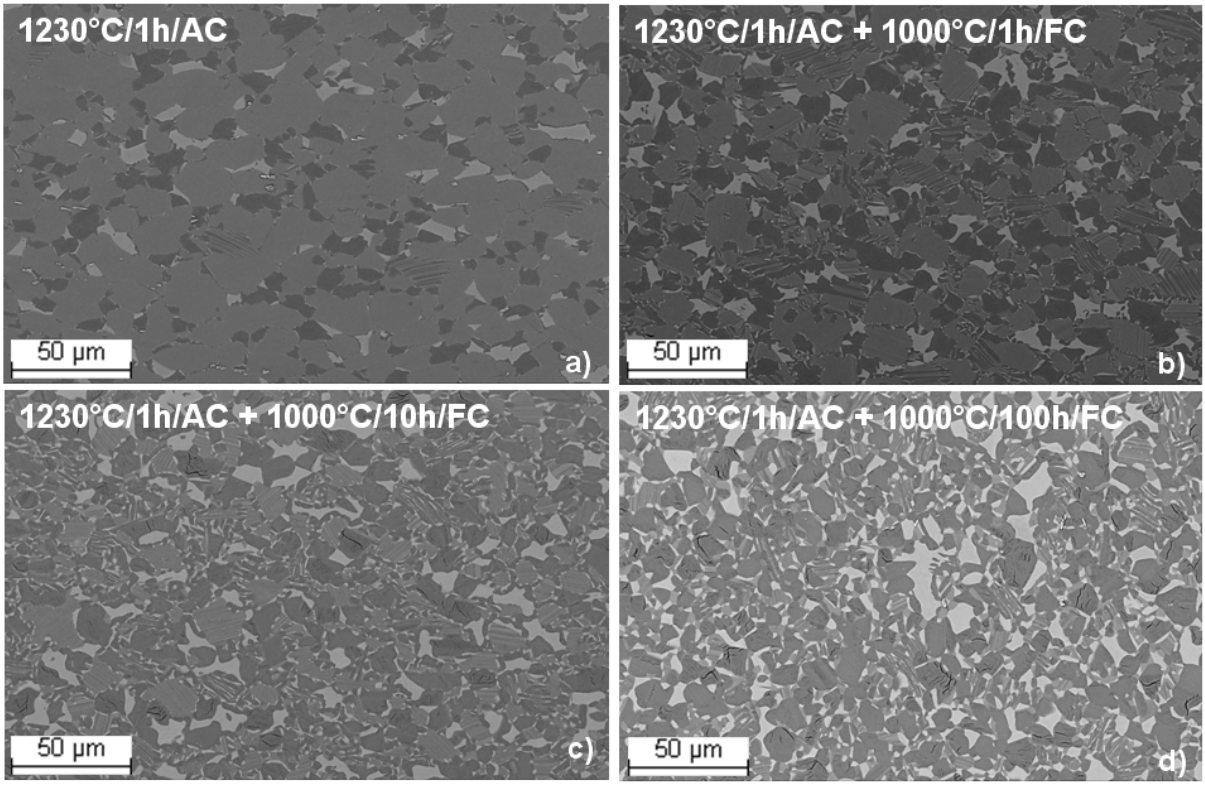

Fig. 13: SEM-BSE images of TNM-B1 after two-step heat treatments. The second annealing step is conducted at 1000°C. The holding time varies from 1 to 100 h, followed by furnace cooling.

At 1000°C the transformation of the microstructure starts earlier than at 900°C and is already advanced after one hour (Fig. 13b). Regarding the thermodynamic calculations (see section 2.2) the stable β-content for this temperature is higher than for 900°C, whereas the content of α_2 and γ decreases only minimally from 900 to 1000°C. It can be seen from the SEM images that more β forms in the cellular reaction compared to the images from the 900°C heat treatments (Fig. 12). After 10 h at 1000°C (Fig. 13c) it can be seen that the discontinuously precipitated regions have started to globulize and β starts to form within the secondary α_2- and γ-lamellae formed in the first heat treatment step. After 100 h at 1000°C (Fig. 13d) most of the microstructure consists of small globular grains and only a few grains containing secondary lamellae are left.

As already found by Chladil [3] the eutectoid temperature T_{eu}, that shows a β-maximum, as obtained from the thermodynamic calculations is too low and has been found to be above 1100°C by DSC measurements (see section 2.2). Thus, a further increase of β can be expected for heat treatments at 1100°C (see the extrapolated course of the β-phase in Fig. 2, alloy A). Figure 14 shows micrographs of samples annealed at 1100°C for various times during the second heat treatment step.

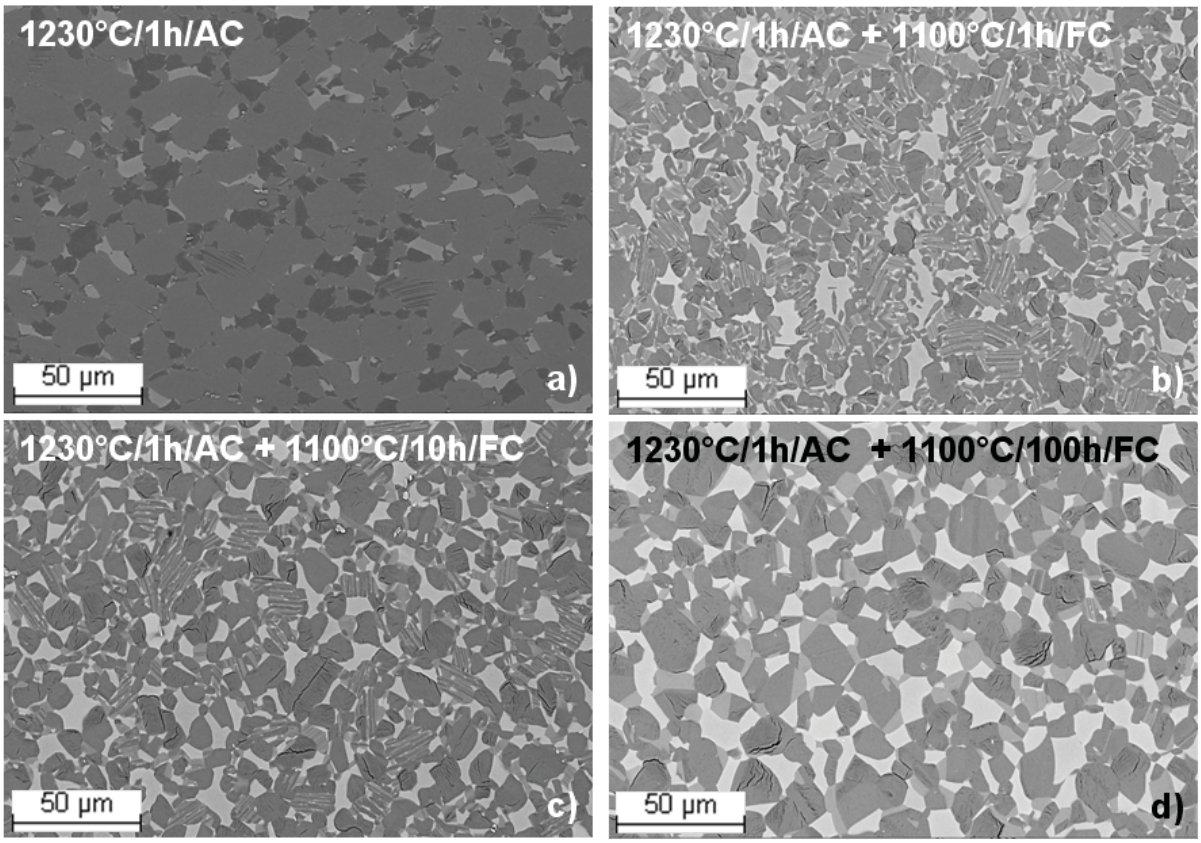

Fig. 14: SEM-BSE images of TNM-B1 after two-step heat treatments. The second annealing step is conducted at 1100°C. The holding time varies from 1 to 100 h, followed by furnace cooling.

After 1 h at 1100°C (Fig. 14b) a fair amount of the microstructure has undergone discontinuous precipitation resulting in α_2, γ and β. Furthermore, the grains have started to globulize. The state of the microstructure is comparable to the situation after a second heat treatment step at 1000°C for 10 h (Fig. 13c) with the exception that more β is present after heating to 1100°C. The presence of γ-precipitates within the β-grains is also observed. Figure 14c shows the microstructure after 10 h at 1100°C, which can be compared to the microstructure after 100 h at 1000°C (Fig. 13d). Again, with the difference that the β-phase fraction is higher at 1100°C. The grains are coarser and closer to the thermodynamic equilibrium which can also be seen from the equilibrium shapes of the constituting particles. After 100 h at 1100°C (Fig. 14d) the whole microstructure consists of globular grains and hardly any evidence is left of discontinuous precipitation the material has undergone earlier. It can be assumed that, depending on the thermodynamic equilibrium, α- or γ-grains emerge from the former secondary lamellae colonies through coarsening. Due to the high amount of globular γ-grains it is suggested that in addition to the cellular reaction the nucleation and formation of monolithic γ-grains occurs at those high temperatures, as also observed by Denquin et al. [15].

Figure 15 summarizes the result of quantitative metallography and shows the dependence of the β-phase volume fraction as a function of temperature for the three different annealing temperatures applied in the second heat treatment step.

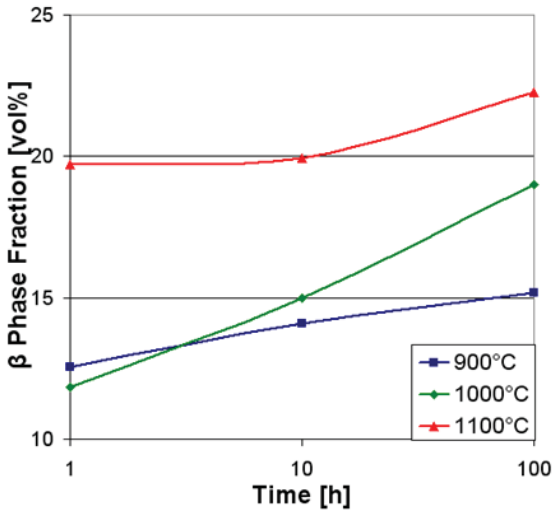

Fig. 15: Changing of the volume fraction of the β-content in the TNM-B1 alloy for the heat treatments listed in Table 3. The results are derived from quantitative metallographic analyses conducted on SEM images shown in Figures 12 to 14. The β-phase fraction increases with time and temperature as the microstructure approaches thermodynamic equilibrium.

As shown in Figure 15 the β-phase volume fraction increases with time and temperature in order to reach thermodynamic equilibrium.

Figure 16 proposes a model for the discontinuous process in the TNM-B1 alloy.

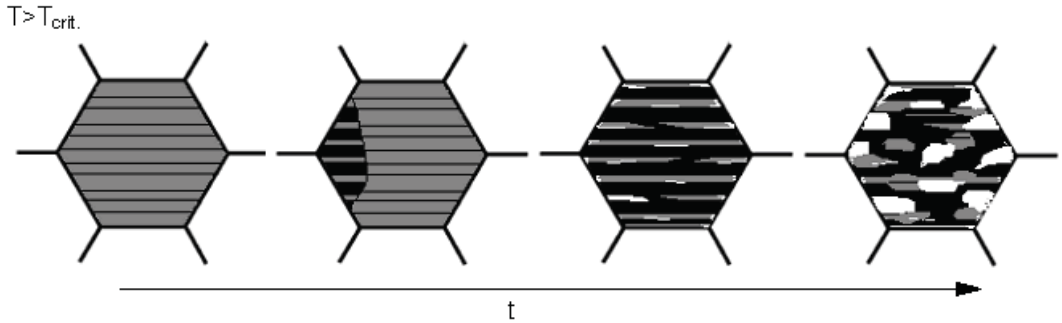

Fig. 16: Model of discontinuous precipitation in the TNM-B1 alloy. The first sketch shows a α_2-grain with very fine primary γ-lamellae. The discontinuous precipitation starts in the second sketch and has migrated across the grain forming coarse secondary α_2- and γ-lamellae (sketch three). The last sketch shows the secondary lamellae after globulization after a considerably long holding time at annealing temperature. $T_{crit.}$ denotes the temperature where discontinuous precipitation is triggered.

The first sketch shows a primary lamellar colony that was cooled rapidly from the α-phase field. The colony is heated to a critical temperature $T_{crit.}$ that is high enough to trigger the discontinuous precipitation. The reaction starts at the colony boundary which consequently migrates across the colony, as drafted in sketches 2 and 3. The resulting secondary lamellae are coarse, the lamellar interfaces are less dense and smooth and β has precipitated along with α_2 and γ. The last sketch shows the coarsened secondary α_2-, γ- and β-lamellae that finally form globular grains.

TEM investigations performed by Gopal Das [23] on a sample of the material FD_MTU04 out of the same heat as alloy TNM-B1 show a high amount of ω-phase within an ordered β_O-grain after a two step heat treatment at 1230°C for 1h followed by air cooling and 850°C for 6h and subsequent furnace cooling. Representative TEM images can be seen in Figure 17.

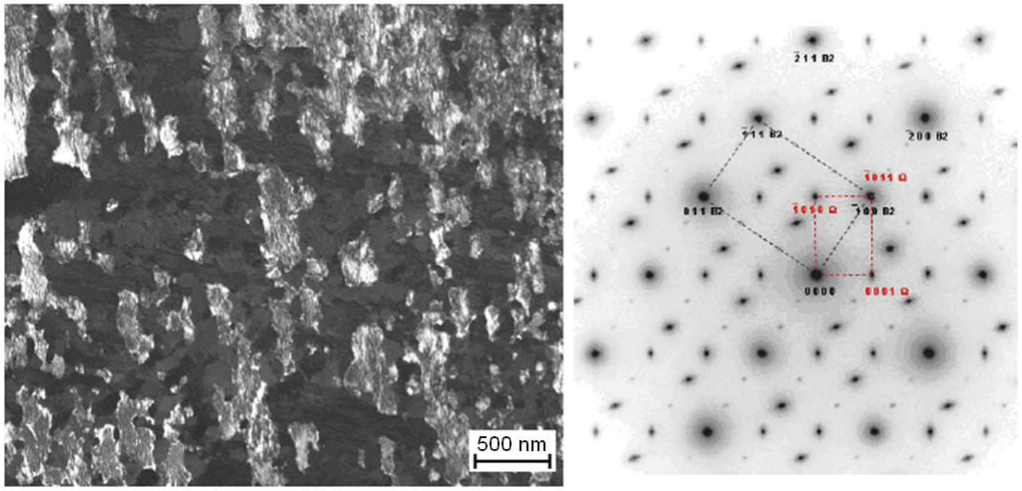

Fig. 17: TEM dark field image of an ordered β_O-grain containing ω is shown on the left. The dark contrast is β_O, the bright contrast shows ω. The right image shows selected area diffraction analyzed to contain both β_O- and ω-phases (β_O black, ω red) The zone axis is $[110]_{\beta_2} \parallel [2\bar{1}\bar{1}0]_{\omega}$ [23].

The ordered ω-phase exhibits lower crystal symmetry ($B8_2$-structure) and thus is believed to be more brittle than the ordered β_O-phase [24]. These findings have been confirmed by Cha [25] and further investigations are in progress to relate the influence of heat treatment on the formation of ω-phase. Although no evidence of the ω-phase was found in the FD_MTU05 material in the XRD-data, the presence of ω cannot be excluded. Due to the deformation texture of the β-phase it is possible that, depending on the imaging direction, the ω-phase cannot be detected in an XRD-scan.

Finally, long-term heat treatments at 800°C were performed by Wallgram [13] on a similar TNM-alloy after a first heat treatment step at 1270°C for 1h with subsequent air cooling. The SEM images of the samples after 1000 h, 2000 h and 3000 h show no indication of a cellular reaction and are displayed in Figure 18.

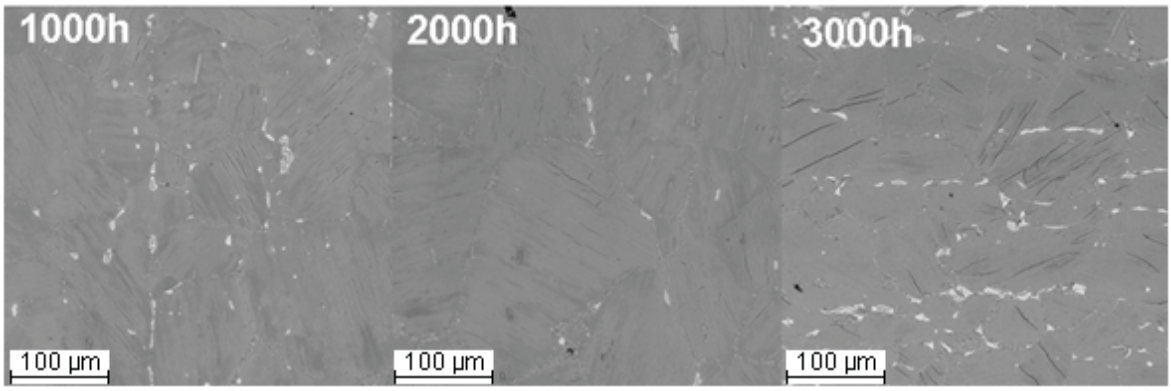

Fig. 18: SEM-BSE images for a TNM alloy after long term heat treatments at 800°C. No evidence of a cellular reaction is shown [13].

Therefore, it can be concluded that $T_{crit.}$ of the onset of a cellular reaction is above 800°C. This result is of great practical importance since the maximum service temperature of this alloy is 800°C.

3 Synchrotron and Neutron Diffraction in Materials Science

3.1 Historical Review of Synchrotron Radiation

Synchrotron radiation was first observed in 1947 in an electron synchrotron after searching for the energy losses occurring in the particle accelerator. Initially regarded a ”nuisance“, it soon became clear that synchrotron radiation was not only an adversarial side effect but could be a useful research tool in the fields of materials science, biology, medicine, and engineering [26-30].
The reason for the broad application of synchrotron radiation today is its margin of photon energies that ranges from the infrared region to hard X-rays and γ-rays. Measuring the spectral and angular distribution of the radiation was first achieved by Tomboulian and Hartman in 1956 [27], who also reported the first soft X-ray spectroscopy experiments with synchrotron radiation. The first experimental program working with synchrotron radiation was launched by the National Institute of Standards and Technology (formerly National Bureau of Standards) in 1961 through the modification of its 180 MeV electron synchrotron by including a tangent section into the vacuum system in order to allow access to the radiation. Around the world projects were started for the construction of storage rings to work with synchrotron radiation in the above mentioned fields of science. The first synchrotron radiation facilities were built in the early 1960’s in the United States, Europe and Asia. Shortly after, the first generation of storage rings was put into operation with the Tantalus I at the University of Wisconsin-Madison, showing the advantages of a beam continuously circulating for several hours, with regular injection and acceleration sequences. In this configuration higher beam currents and thus higher fluxes of radiation could be achieved, as well as a more stable beam and a reduced radiation hazard. The implementation of several other storage rings followed before the next step was taken [26,27].
Second generation facilities were sources dedicated to the production of synchrotron radiation allowing higher beam energies than the electron-positron colliding-beam machines used before. The objective was to achieve increased brightness, which at that time could only be obtained by using a more narrow focus of the beam while increasing beam divergence. Apertures that help reduce beam size and divergence but also diminish the flux were another possible solution to the problem. A proper design of the source was developed by

Chasman and Green [27]. The newly designed lattice, i.e. the arrangements and strengths of the magnets in the storage-ring lattice, where the beam size and divergence are determined, was the prototype for most of today's sources. In addition to bending magnets, that bend the electrons to keep them in a closed orbit and thereby cause the emission of radiation, insertion devices, namely undulators and wigglers, were incorporated in existing facilities. Those devices cause the electron beam to oscillate between periodically arranged magnets to enhance the radiation output [28,29].
Third generation facilities evolved with the demand for lower emittance and higher brightness. This was realized by introducing long straight sections for undulators that also entail good spatial coherence. High brightness is a requirement for experiments where spatial resolved information, temporal resolution and the combination of microscopy and spectroscopy are crucial factors, as well as for measurements that include crystallography, spectroscopy and fast data collection. The first third generation synchrotron radiation facility put into operation was the European Synchrotron Radiation Facility (ESRF) in Grenoble in 1994. The latest step in development is reached with free electron lasers that exceed synchrotron radiation sources in brightness, coherence and in pulse durations [26-30].

3.2 Physics of Photons and Neutrons

Particular physical properties make photons, at wavelengths of X-rays, and neutrons substantial tools for materials research. Their importance is based on the magnitude of their energies and wavelengths that correspond to the dimensions of atoms, molecules, chemical bonds, and lattice parameters in crystals, permitting the study of solid structures. X-rays and neutrons both penetrate into matter in a range from µm to cm, in which they differ from electrons that interact much more strongly with matter, penetrate less deeply and, therefore, allow the probing of surface near regions. X-rays and neutrons, however, enable the non destructive study of structures in bulk material [30].
From the interaction of a plane wave of the wave vector k

$$|k| = \frac{2\pi}{\lambda} \qquad \text{(Equ. 5)}$$

at wavelength λ and the amplitude ψ_0

$$\psi_0 = e^{ikz} \quad , \qquad \text{(Equ. 6)}$$

a spherical wave ψ_S

$$\psi_S = \frac{b}{r \cdot e^{ikr}} \quad , \qquad \text{(Equ. 7)}$$

is generated from the plane wave. The spherical wave is centered around the scatter at the location r where the scattering length b, a complex number, represents a repulsive interaction in the positive real part, an attractive interaction in the negative real part and the absorption in the imaginary part [28,30-32].

3.3 Interactions

3.3.1 Photons

X-rays are scattered by the electron cloud of the atom or the electronic band structure in a crystalline solid. During the interaction of an electromagnetic plane wave with an electron it causes the electron to accelerate in the direction of the oscillating field of the incident wave and as a result creates the scattered wave that is an electromagnetic dipole field as shown in Figure 19 [30].

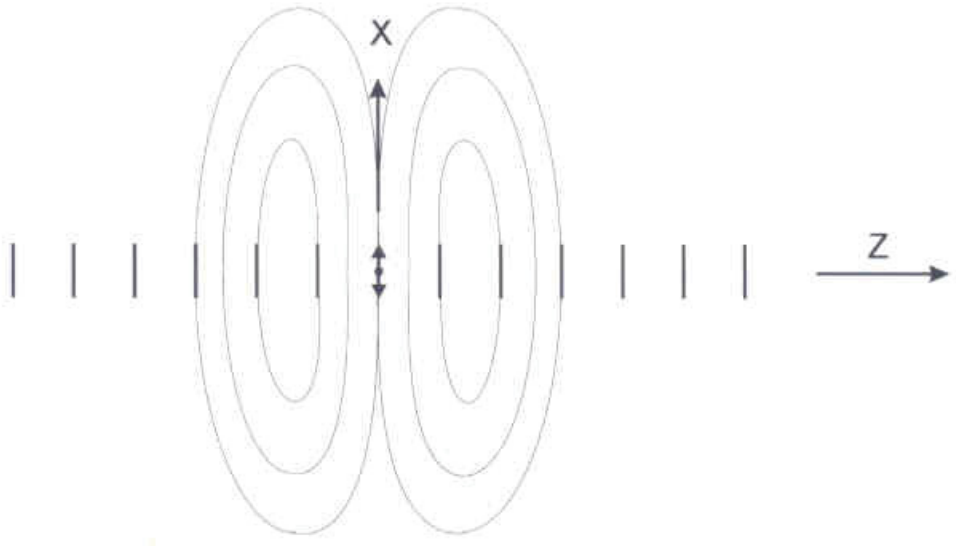

Fig. 19: Sketch of a scattered wave, the electromagnetic dipole field generated by the interaction of X-rays with the electromagnetic shell of an atom [30].

The scattering intensity is constant in the y-z plane, depends on the scattering angle in the x-z plane and is zero in x-direction, so that scattering experiments are usually performed in the y-z plane. The Thomson scattering length r_e, named after J.J. Thomson who first explained this phenomenon, depends on the electron charge c, the electron mass m_e and the velocity of light c. It can be described as follows [28]:

$$r_e = \frac{e^2}{m_e \cdot c^2} \qquad \text{(Equ. 8)}$$

With a value of 2.82 fm the Thomson scattering length is five orders of magnitude smaller than an atomic shell, so that all of the remaining electrons have to be taken into consideration for the description of scattering from the atom. The so-called form factor f_e accounts for the different locations of the electrons within the atom and the hence resulting scattering phase differences. For small scattering angles, i.e. a small scattering vector q, f_e decreases with decreasing number of electrons Z of the atom [28, 31].

3.3.2 Neutrons

Neutrons are nuclear particles and therefore interact with the nucleus of the atom, consisting of protons and neutrons, based on the strong interaction. Therefore, it is possible to determine the spacious alignment of the atoms in the solid. Protons and neutrons are very small compared to the wavelength of the neutron. Additionally, their interaction range is small so that the interaction can be described in a simplified way as a scatter of point dimension. The scattering length depends highly on Z and the mass number A of the scattering atom. Contrary to X-rays, neutron scattering lengths b_n are negative for some elements, including Ti, as can be seen in Figure 20.

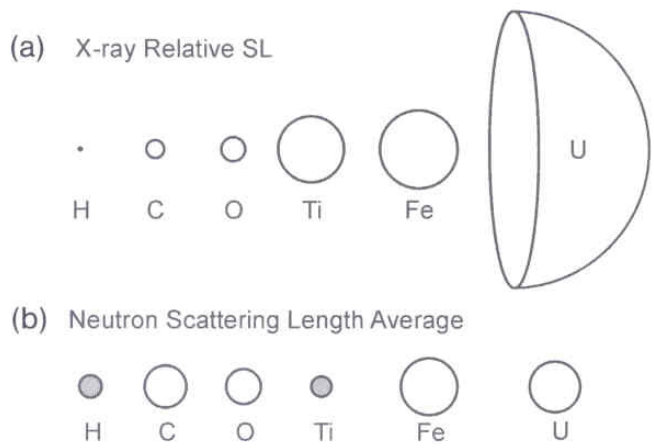

Fig.20: Comparison of scattering lengths (SL) for different elements for X-rays (a) and neutrons (b). The radii of the circles are proportional to the scattering lengths, for better presentability they are multiplied by 2 for neutrons. The shaded circles denote negative scattering lengths [30].

The neutron exhibits a magnetic dipole moment, which interacts with magnetic moments of magnetic material. Therefore, neutrons are suitable probes for the analysis of magnetic matter. They are also adequate for the investigation of large bulk specimens since they are barely absorbed and can penetrate deeply into the material [30-33].

3.4 The Generation of Synchrotron Radiation

Synchrotron radiation is nowadays produced in storage rings, by the acceleration of electrons or positrons that run around the ring at a velocity very close to the speed of light. Due to energy losses accompanying the emergence of synchrotron radiation the particles have to be reaccelerated by accelerating radio frequency cavities to remain at constant energy [28].
The particles have to be kept on the orbit and emit synchrotron radiation as they are accelerated by bending magnets. Wigglers and undulators are special insertion devices that in addition enhance the emitted radiation by forcing the electron beam on a sinusoidal trajectory through an array of alternate magnets. They are described by the wiggler parameter which is

$$K = 0.934 \cdot \lambda_0(cm) \cdot B_0(T) \qquad \text{(Equ. 9)}$$

for practical units [30]. λ_0 is the period length of the magnetic field and B_0 its peak value. The device is called wiggler for K >>1, causing an intensity enhancement of

2N, with N representing the magnetic periods in the wiggler, and emitting the radiation in forward direction with opening angles in the mrad range. For $K \leq 1$ the device is called undulator. In this case radiation from different poles interacts through constructive interference, so that the radiation enhancement follows an N^2 law. For both, wigglers and undulators, right- and lefthanded circular polarization cancel out since there is the same number of right and left turns [30].
The characteristics of radiation produced from bending magnets, wigglers, undulators and free electron lasers are compared in Figure 21 [28-31].

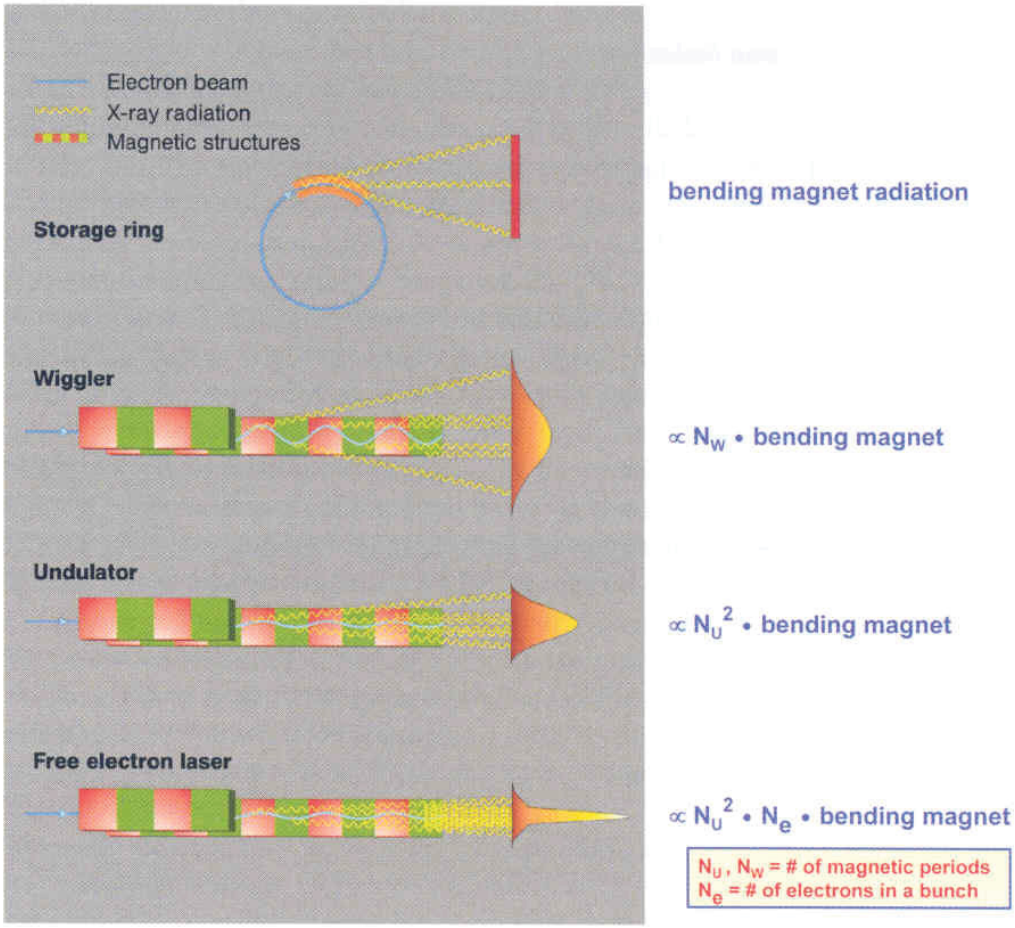

Fig. 21: Schematic illustration of synchrotron radiation sources [30].

3.5 The Generation of Neutron Radiation

The neutron decomposes to a proton, an electron and an antineutrino through the beta-decay. Neutrons can either be produced in nuclear reactors or in particle accelerators, so-called spallation sources, where neutrons are generated from the fragmentation of atomic nuclei [30].

3.5.1 Nuclear Reactors

The fission reaction taking place for the generation of thermal neutrons in nuclear reactors is

$$^{235}U + n_{therm} \rightarrow A + B + 2.3n \ , \qquad \text{(Equ. 10)}$$

where A and B are fragments of the original ^{235}U nucleus. n_{therm} is a thermal neutron and n are the resulting neutrons. Those neutrons are decelerated by a moderator and can then activate further fission by a series of reactions. A part of the neutrons is let out of the reactor and is available for the use in experimental research. The energy distribution of the neutrons leaving the reactor depends on the temperature of the moderator [30,32]. For the production of cold neutrons, the neutrons from the reactor are first moderated in liquid deuterium at a temperature of 25 K and then remitted to the experiment. An example of a moderator for hot neutrons is graphite at 2000 K [32].

3.5.2 Spallation Sources

In spallation sources neutrons are produced by the shelling of heavy elements with high energy protons leading to the following reaction [32]:

$$p + ^{238}U \rightarrow spallation\ products + xn \ . \qquad \text{(Equ. 11)}$$

Following this reaction, the number of generated neutrons depends on the proton energy and the target material and can be raised to 28 neutrons per proton for 800 MeV and uranium as a target material. When using pulsed accelerators for the spallation reaction, the resulting neutron radiation is also pulsed, which can be beneficial for time-of-flight experiments. As in nuclear reactors, the emerging neutrons must be moderated for the use in experiments, so that the two facilities work with similar principles [30,32].

3.6 The Rietveld Method

The Rietveld method is a tool for the analysis of polycrystalline materials, first developed for the interpretation of neutron diffraction data in the late 1960's by Hugo Rietveld [34]. Information on the structure of a material can be obtained from the position, height and width of the peaks in its diffraction pattern. The Rietveld method fits these diffraction patterns by a least squares approach, refining the profile until it ideally matches the measured data. At the time the method was developed, the overlapping of peaks was a problem for the evaluation of diffraction patterns, and increasing resolution could only help to improve the definition of diffraction patterns, but not to such an extent to completely resolve the peaks. Unlike methods usually applied at that time, which considered only individual Bragg reflections, the Rietveld method regarded the pattern as a whole, separating overlapping peaks by fitting profile functions. This first model used a Gaussian profile, as suitable for neutron diffraction data. For further improvement of the method Rietveld used individual intensities y_i instead of integrated intensities, as they were used for single crystal data, and the relative contributions of each peak. Later a correction of asymmetry and the options of refining structures and profile parameters were included in the method. The method refines the intensity values along the diffraction angle 2θ to match the recorded intensities adopting a least squares approach after the following principle [34-36]:

$$S = \sum_i w_i (y_i(obs) - y_i(calc))^2 = Minimum \ , \qquad \text{(Equ. 12)}$$

with w_i representing the weight of each data point and y_i (obs) and y_i (calc) the observed and calculated intensities, respectively [34].
The Rietveld method is very complex and can only slightly modify a predefined model, so that starting values must already be very close to the final parameters. A lot of different information can be obtained from the Rietveld method. The peak positions reveal the lattice parameters and space group of the investigated material, the background gives information about the amorphous fraction or local disorder in the specimen and the FWHM, the broadening of the peaks, gives information about the particle or domain size, stress and strain states and qualitative and quantitative phase analysis [34]. The latter was mainly utilized in this work.
Parameters influencing the peak shape are the spectral distribution as instrumental parameter and the crystal structure as a sample parameter. Peaks in patterns from neutron diffraction show a very strong Gaussian character, whereas

peaks obtained from X-ray or synchrotron experiments can be best fitted with a Pseudo-Voigt function. This is a summation of a Gaussian and a Lorentzian function where the contributions can be varied [34,35,37].
The peak width, described with the dimension FWHM, depends on the diffraction angle 2θ and is described by Caglioti et al. [38] as follows:

$$(FWHM) = U \cdot \tan^2 \theta + V \cdot \tan \theta + W \qquad \text{(Equ. 13)}$$

U, V and W are parameters to be adjusted in the fitting procedure. Originally introduced for the refinement of neutron data the Rietveld method is nowadays also used for X-ray and synchrotron patterns [34,37].

3.6.1 Quantitative Phase Analysis by the Rietveld Method

In the quantitative phase analysis by the Rietveld method, the percentages w_p of the constituent phases p are evaluated through their scale factors S. The scale factors are related to the masses of the phases in the analyzed material through an algorithm embracing the product of mass and volume of the unit cell of the individual phases. This algorithm has been described by Hill and Howard in 1987 and improved by Brindley in 1945 by adding the influence of the relative absorption and particle size:

$$w_p = \frac{S_p (ZMV)_p}{\left(\dfrac{\sum_j S_j (ZMV)_j}{\tau_j} \right) \tau_p} \quad , \qquad \text{(Equ. 14)}$$

where w_p is the relative weight fraction of phase p in a material of j phases. S is the scale factor, Z the number of formula units per unit cell, M the mass of the formula unit and V is the volume of the unit cell. τ_j stands for the absorption factor of the respective phase [34].

3.7 TNM Structure Factor Considerations

The structure factor F of a crystal describes how the material scatters incident radiation. F is the Fourier transform of the crystallographic unit cell and is mathematically described as [39]:

$$F(\vec{G}) = \sum_{i}^{unitcell} b_i^c \cdot e^{-1\vec{G}\vec{r}_i} \ , \qquad \text{(Equ. 15)}$$

where $\vec{G}$ is the scattering vector and b_i^c is the coherent bound scattering length for the i-th atom.

For a bcc structure, i.e. the atom positions are $[100]$ and $\left[\frac{1}{2}\frac{1}{2}\frac{1}{2}\right]$, the 100-reflection with $\vec{G}_{100} = \frac{2\pi}{a}[100]$ is:

$$F(100) = b_1 \cdot e^{-i\frac{2\pi}{a}[100]\begin{bmatrix}1\\0\\0\end{bmatrix}\cdot a} + b_2 \cdot e^{-i\frac{2\pi}{a}[100]\begin{bmatrix}\frac{1}{2}\\\frac{1}{2}\\\frac{1}{2}\end{bmatrix}\cdot a} = b_1 \cdot e^{-i2\pi} + b_2 \cdot e^{-i\pi} = b_1 - b_2 \ . \qquad \text{(Equ. 16)}$$

For the 110-reflection, F results in $b_1 + b_2$.

This means that for disordered structures, where $b_1 = b_2$ the 100-reflection is extinguished and the 110-reflection is generally strong. For ordered structures $b_1 \neq b_2$ applies so that F(100) is generally very weak and F(110) is generally strong. This is valid for synchrotron diffraction.

The difference for neutrons is that the scattering length for Ti is negative, $b_{Ti} = -3.438$ fm and $b_{Al} = 3.449$ fm. The material exhibits a so-called “zero matrix” and the structure factors for disordered structures are almost zero, so that the usually observed intensities are extinguished. In this case only reflections from ordered structures can be detected, which are generally strong.

For a better comparability of synchrotron and neutron data, that have been recorded at different wave lengths, the patterns are usually displayed in the q-space, in dependence of the scattering vector q that is defined as follows [30]:

$$|q| = \frac{4\pi}{\lambda \cdot \sin\theta} \ . \qquad \text{(Equ. 17)}$$

The reciprocal lattice vector G_{hkl} is related to the lattice through the following relationship [30]

$$\left|G_{hkl}\right| = \frac{2\pi}{d_{hkl}} \ , \qquad \text{(Equ. 18)}$$

where d_{hkl} is the lattice spacing. For q=G the intensity shows strong Bragg peaks [30].

3.8 Experimental

3.8.1 Synchrotron

The synchrotron measurements in the present work were performed at the beamline ID15 at the European Synchrotron Radiation Facility (ESRF) in Grenoble, France. A custom-made furnace heated the samples up to 1400°C. The temperature was controlled by a pyrometer. The furnace is described in detail in [40], a sketch of the furnace is shown in Figure 22.

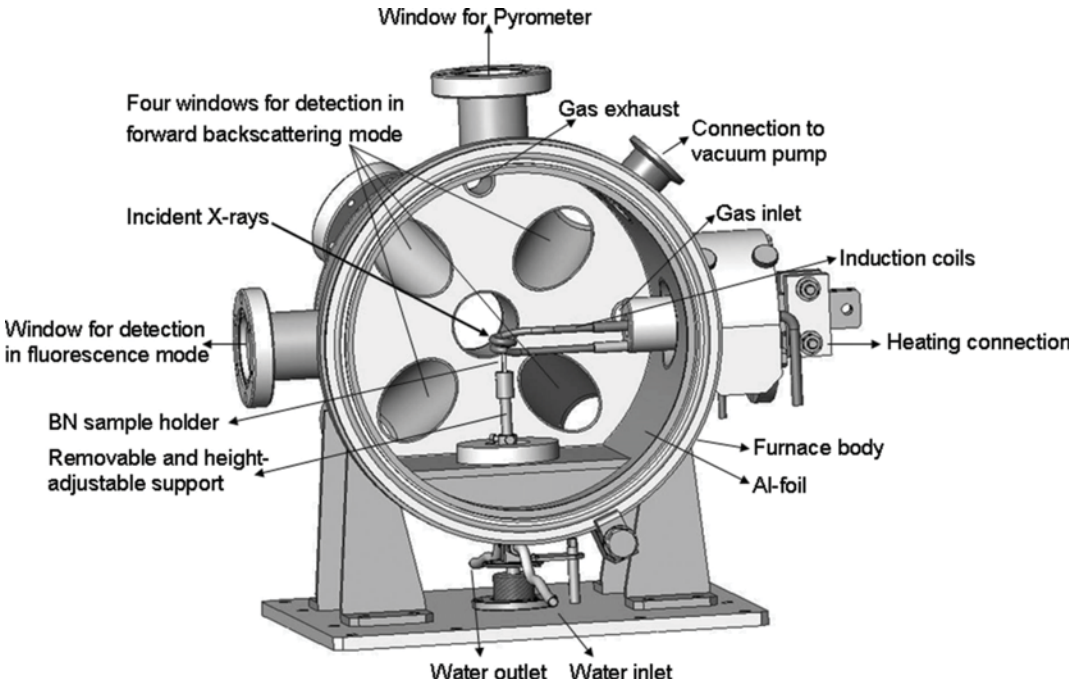

Fig. 22: Furnace at the ESRF beamline ID15 [40].

The oxygen partial pressure was reduced and the furnace was irrigated with Ar, to reduce oxidation during the measurements. The furnace's entrance hole for the

beam and the exit hole for the Debye-Scherrer rings were covered with polyimide foils for sealing. The specimens were mounted an a Al_2O_3 sample holder and rotated during the experiment in order to increase the homogeneity of the diffraction rings. Monochromatic synchrotron radiation with a nominal energy of 86.78 keV was used. A two-dimensional image plate detector with a resolution of 2640 x 1920 pixels and a pixel size of 154 x 154 μm^2 detected the scattered photons. The images were obtained with an exposure time of 12 s. The patterns covered a diffraction angle q from 1 to 10 nm^{-1}. The Debye-Scherrer rings were integrated for equal radial distances from the centre of the X-ray beam using the software program Fit2D by ESRF.

3.8.2 Neutrons

The neutron diffraction measurements were performed at the Structure Powder Diffractometer (SPODI) at the Forschungsneutronenquelle Heinz Maier-Leibnitz (FRM II) in Munich, Germany. The monochromator to sample distance was 5 m and the wavelength λ=1.5481 Å. The sample was heated up to 1400°C in a furnace and measured with a detector array of 80 He-3 detector tubes, covering a 160° scattering angle. The diffraction patterns were derived from the two-dimensional data by integration along the Debye-Scherrer rings [41].

3.8.3 Material and Temperature Programs

The materials investigated with synchrotron radiation are the alloys A, B and C, as described in section 2.2. Samples with a diameter of 4 mm and a length of 10 mm were taken from the material by spark erosion.
In the neutron experiments the TNM-B1 alloy was investigated with a sample diameter of 7 mm and a length of 35 mm. The samples were also spark eroded. Both materials were in the as-cast state.

The samples A, B and C were heated from 400°C to 1400°C in the synchrotron beam. They were first heated to 1000°C at a rate of 200 K/min, held at 1000°C for 3 min and then heated to 1050°C at 50 K/min where they were held for 30 s to compensate for temperature oscillations. After that, the samples were heated to 1400°C at a rate of 2 K/min. The temperature program is drafted in Figure 23.

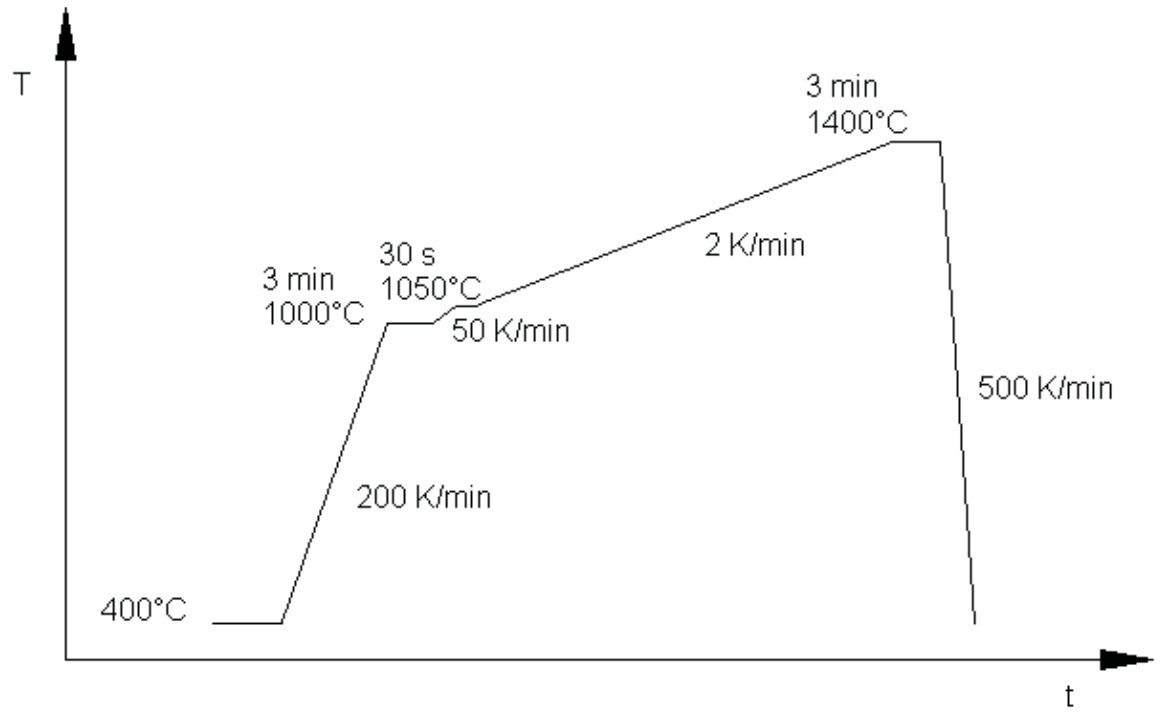

Fig. 23: Temperature program for the synchrotron measurements on alloys A, B and C at the ESRF.

The diffraction patterns were continuously measured every 12 sec. Diffraction patterns from selected temperatures were integrated and fitted by the Rietveld method using the TOPAS software package by Bruker, to evaluate the phase fractions as a function of temperature (see section 3.6).

The sample TNM-B1 was held in the neutron beam and measured isothermally for 3 h at several temperatures between 1000°C and 1450°C, namely 1000°C, 1100°C, 1200°C, 1250°C, 1275°C, 1300°C, 1350°C, 1400°C, 1425°C, and 1450°C, as schematically shown in Figure 24.

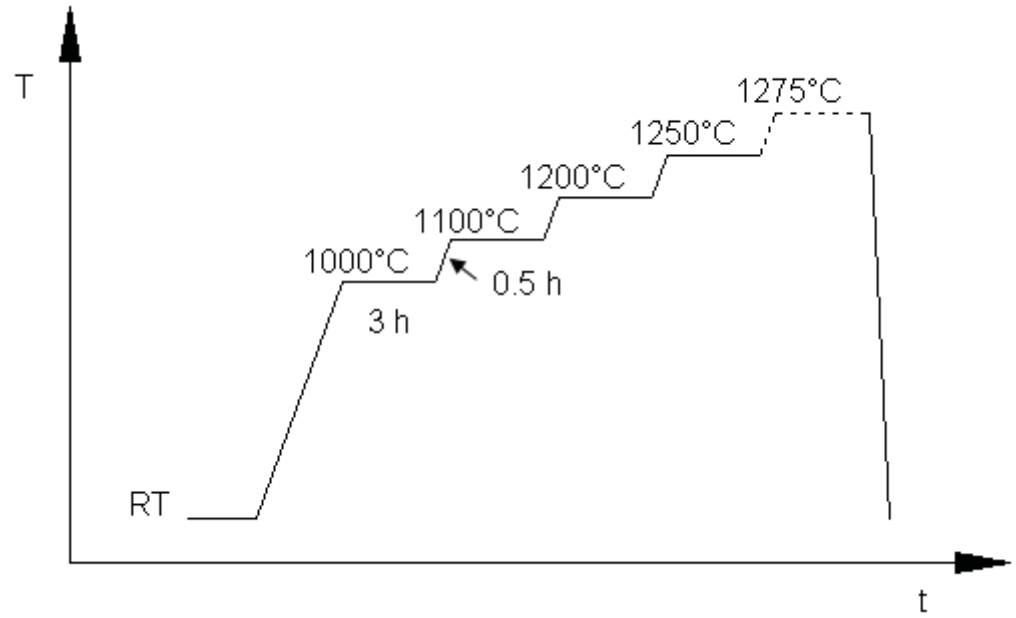

Fig. 24: Temperature program for the neutron diffraction measurements on alloy TNM-B1 at the FRM II.

3.9 Results and Discussion

3.9.1 Synchrotron Data – Alloys A, B and C

For each synchrotron experiment about 650 diffraction patterns were recorded in-situ. Rietveld evaluation of these patterns could not be conducted automatically, so that single files were fitted at selected temperatures. The samples showed grain growth above 1100°C. Therefore, not the whole patterns were integrated above this temperature. Those patterns showed spots with particularly high intensities which made it impossible to distinguish between adjacent reflexes. Only angular ranges that showed no evidence of coarse grains were integrated for those patterns. Additionally, peak shifts towards lower 2θ angles at higher temperatures could not always be detected correctly by the software and had to be adjusted manually.

For example, the detector image from alloy A recorded at 399°C is shown in Figure 25.

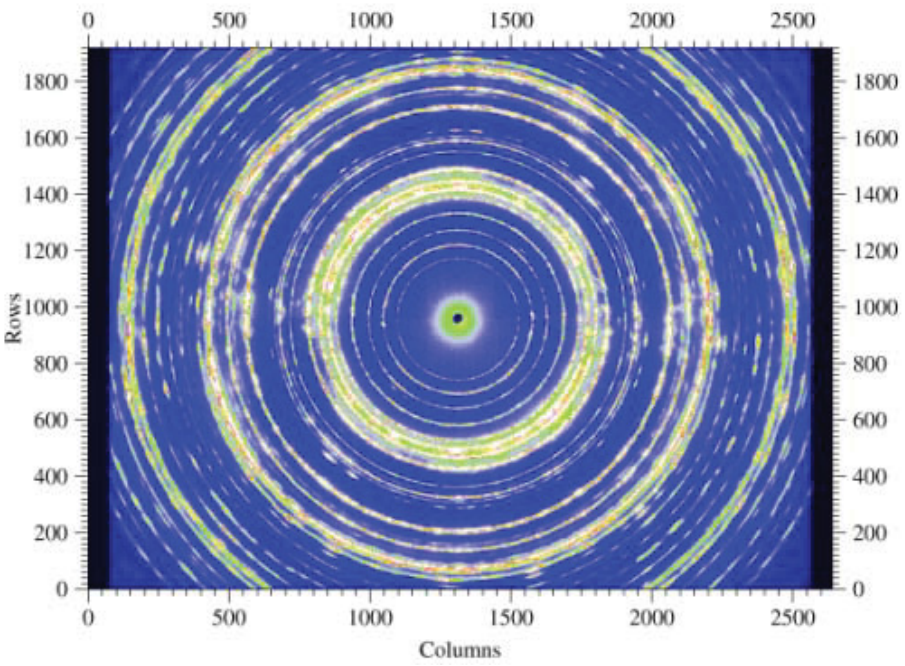

Fig. 25: Synchrotron detector image of alloy A at 399°C. The diffraction rings are homogeneous.

At low temperatures, around 400°C, the diffraction rings are relatively homogeneous and no strong reflections from single coarse grains can be seen on the detector image. The single reflections can be separated from each other and the data can be evaluated quantitatively.
The detector image for 1100°C is displayed in Figure 26.

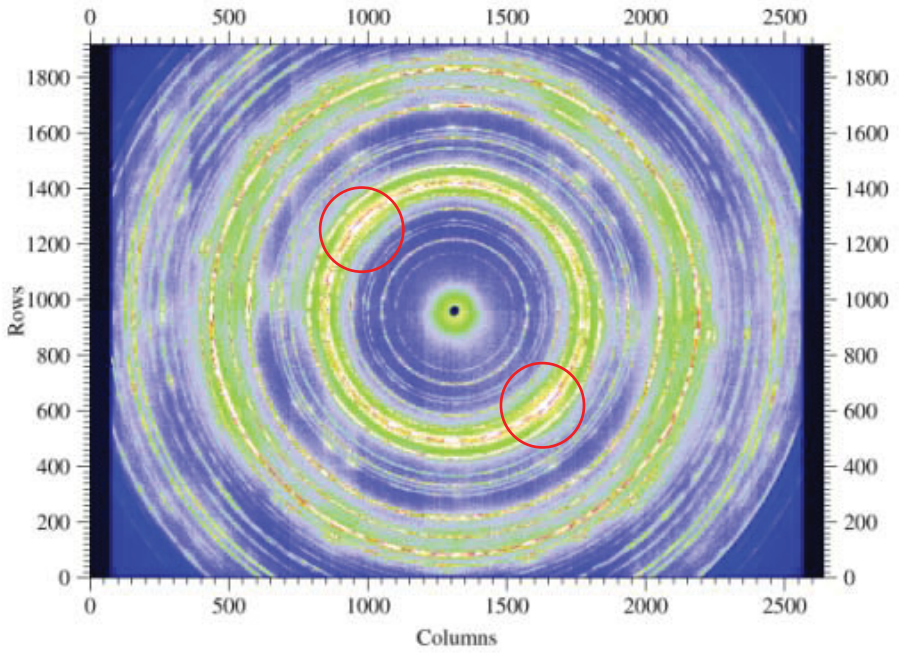

Fig. 26: Synchrotron detector image of alloy A at 1100°C. The red circles indicate spots with high intensities, where adjacent diffraction rings can no longer be distinguished.

Grain coarsening starts at temperatures above 1100°C and large grains cause intensity maxima along the diffraction rings. At the two positions marked with the red circles (see Fig. 26) the intensities are too high and cannot be ascribed to the relevant angular positions so that the reflections cannot be distinguished accurately. For this reason the images above 1100°C were only integrated along angular ranges between those incidents. Integrations were conducted for patterns recorded up to 1300°C. Above 1300°C, the diffraction rings are highly inhomogeneous and mainly consist of intensity spots of single grains. Such a detector image, recorded at 1310°C is shown in Figure 27.

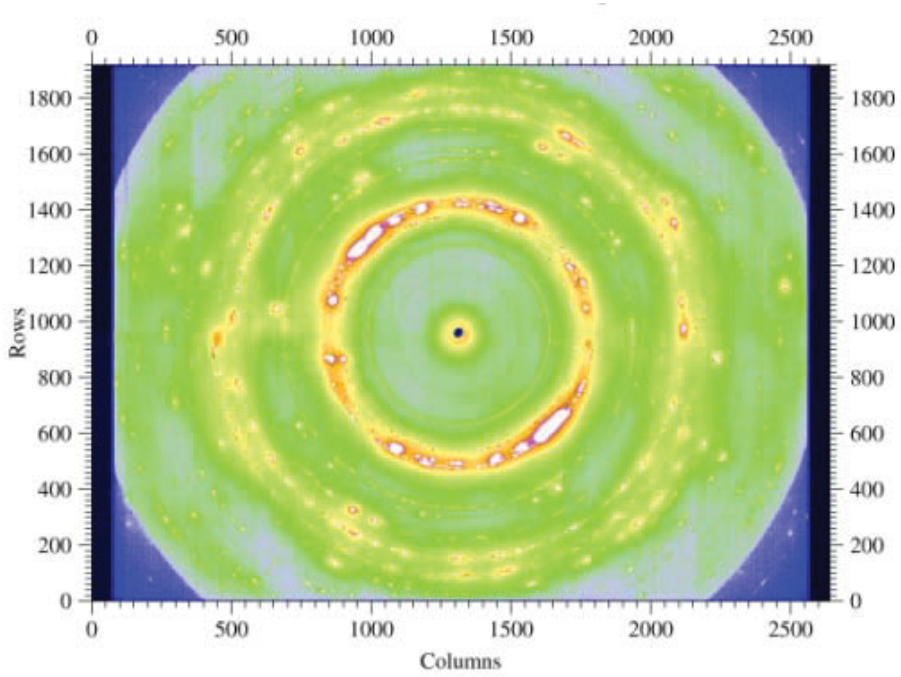

Fig. 27: Synchrotron detector image of alloy A at 1310°C. The diffraction rings are highly inhomogeneous.

The detector image obtained at room temperature was qualitatively evaluated and is shown in Figure 28.

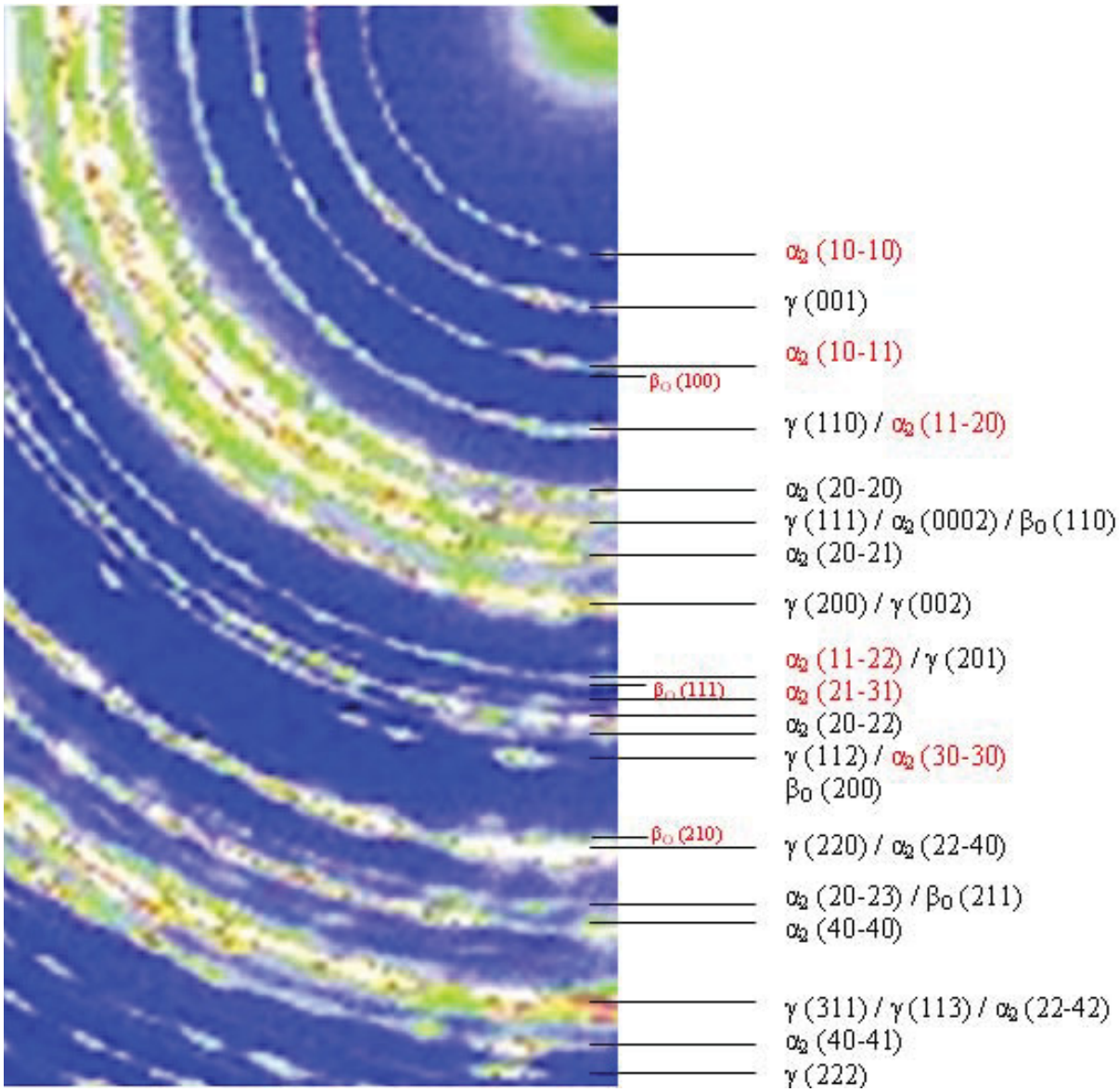

Fig. 28: Indexing of the Debye-Scherrer rings for alloy A at room temperature. Superstructure peaks are marked in red. The intensities of the β_O-superstructure peaks are too weak to be detected, their theoretical positions are marked in red.

Peaks that are marked with red indices are superstructure peaks. Due to the ordered structure the α_2-unit cell is bigger than the α-unit cell, which means that the α_2-unit cell is smaller in the reciprocal space. Furthermore the α_2-phase generates more reflections and the indices h and k are multiplied by two for α_2 compared to α.

In the ordered β_O-phase the Nb atoms are located on the Al-positions. They have a high electron density compared to the electron density of Al and that of Ti. Ti exhibits a value between the electron densities of Al and that of Nb. Therefore, the average electron density for the body centered Al(Nb)-position is similar to the electron density of the Ti position so that the intensity of the superstructure peaks is expected to be reduced drastically. The absence of β_O-superstructure peaks is

therefore no definite indication that no ordered β_O-phase is present in the material, because the β_O and the β-phase cannot be distinguished in the synchrotron measurement. As can be seen in Figure 28, the intensities of the β_O-superstructure peaks are weak and they vanish in the background. Their theoretical positions are marked in red letters. The changes in the Debye-Scherrer rings with increasing temperature are displayed in Figure 29.

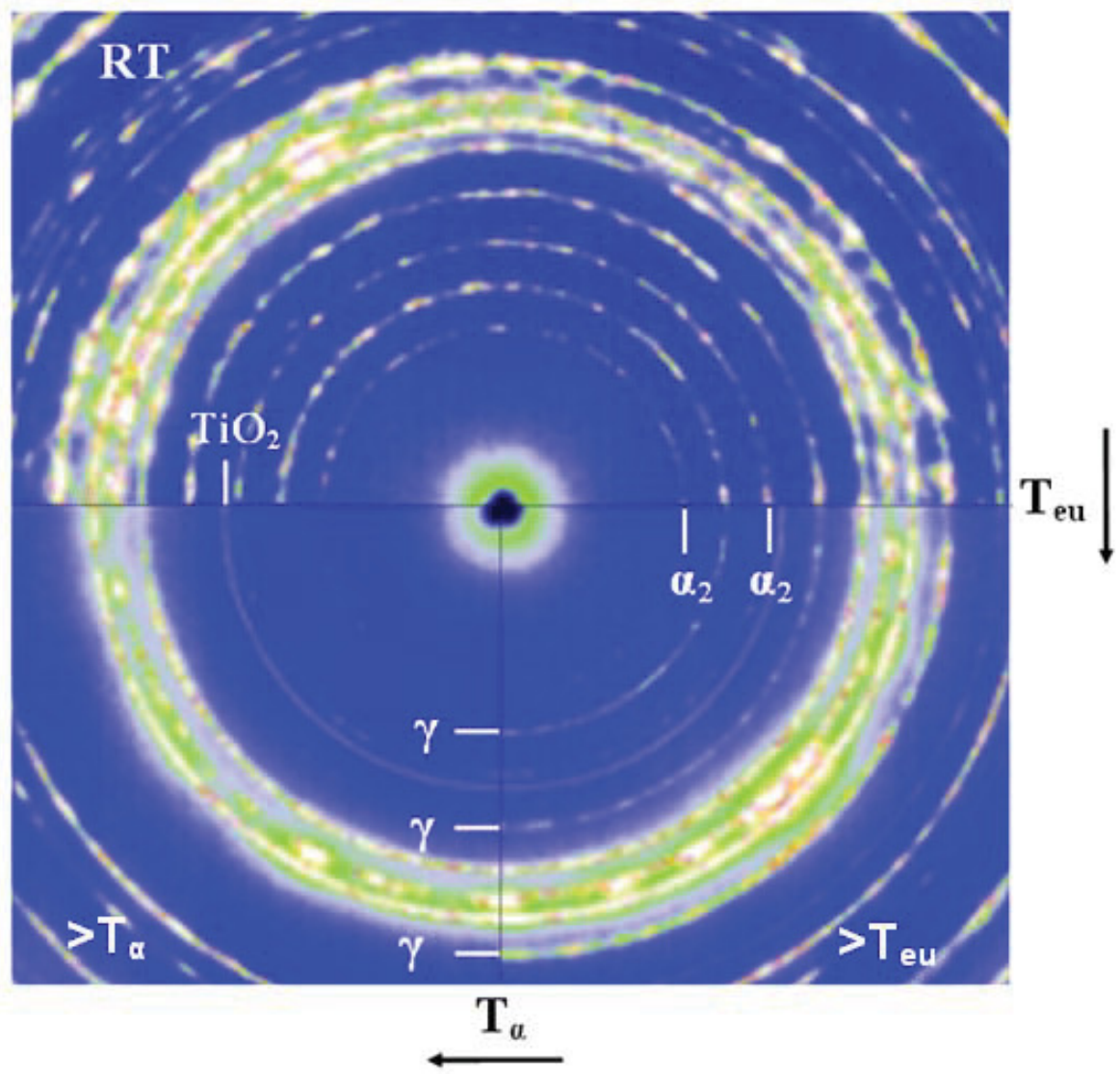

Fig. 29: Changes of the Debye-Scherrer rings with temperature. The upper half represents a pattern taken at room temperature. The disappearance of the α_2-peaks at T_{eu} and of the γ-peaks at T_α can be observed in the lower right and left quadrant, respectively. A TiO_2-peak appears at high temperatures in the lower half of the figure.

The diffraction rings at room temperature are displayed on the top half of Figure 29. A representative Debye-Scherrer pattern recorded above T_{eu} is shown in the lower right quadrant of Figure 29. The lower left quadrant shows the pattern of a sample annealed above T_α. For clearer presentability the image was corrected for temperature shift of the peaks. As illustrated, α_2 disorders to α at T_{eu} and the α_2

superstructure peaks that are marked in the image disappear. The γ-peaks disappear at T_α which can be seen in the lower left part of the figure.
An additional reflection appears in the lower half of Figure 29 that cannot be seen at room temperature. It first appears around 1000°C and is visible throughout the rest of the experiment without showing any indication of grain growth. This peak arises from TiO_2 that forms on the surface of the sample due to the atmosphere in the oven that is not completely inert.

Diffraction patterns derived from Debye-Scherrer rings at selected temperatures from room temperature to 1300°C are plotted in Figure 30. The shift of the peaks towards smaller q-values with increasing temperature results from thermal expansion.

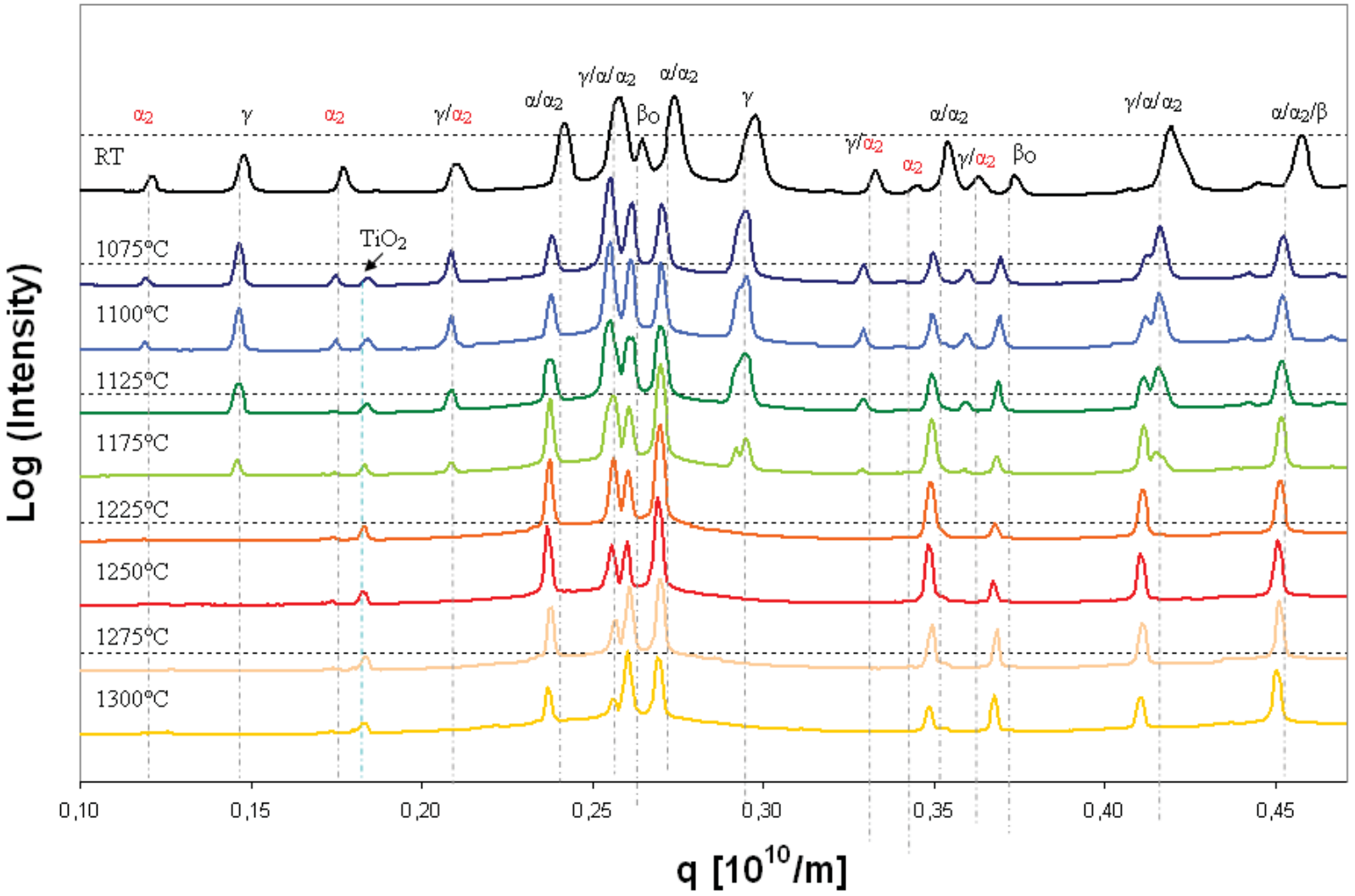

Fig. 30: Synchrotron diffraction patterns of alloy A at selected temperatures between room temperature and 1300°C. Note that the indicated temperatures are not "corrected temperatures" (see text). The TiO_2-peak that appears above 1000°C is marked with an arrow.

The α_2-peaks marked in red are superstructure reflections. Those peaks almost vanish at 1100°C. The intensities are plotted in a logarithmic scale so that the α_2-superstructure peaks at 1100°C are in fact very small compared to the other peaks. The last γ-peaks can be observed at 1175°C. The γ-peak that splits into two peaks at 1175°C at about q=3 consists of the γ(200)- and the γ(002)-peaks, that alter their locations with increasing lattice parameters due to the tetragonality of the γ-unit cell. At 1225°C the pattern comprises only α- and β-peaks. The intensities of the α-peaks decrease while the β-intensities increase with temperature. The peak marked with a turquoise dotted line is the TiO_2-peak that emerges around 1075°C. Its intensity and shape do not change significantly over the whole temperature range. It should be noted that the above stated temperatures are not so-called “corrected temperatures” (see further text).

For a quantitative evaluation of the prevailing phases in the alloys A, B and C depending on temperature, Rietveld fits were produced from the synchrotron data. The obtained results can be seen in Figures 31, 32 and 33.

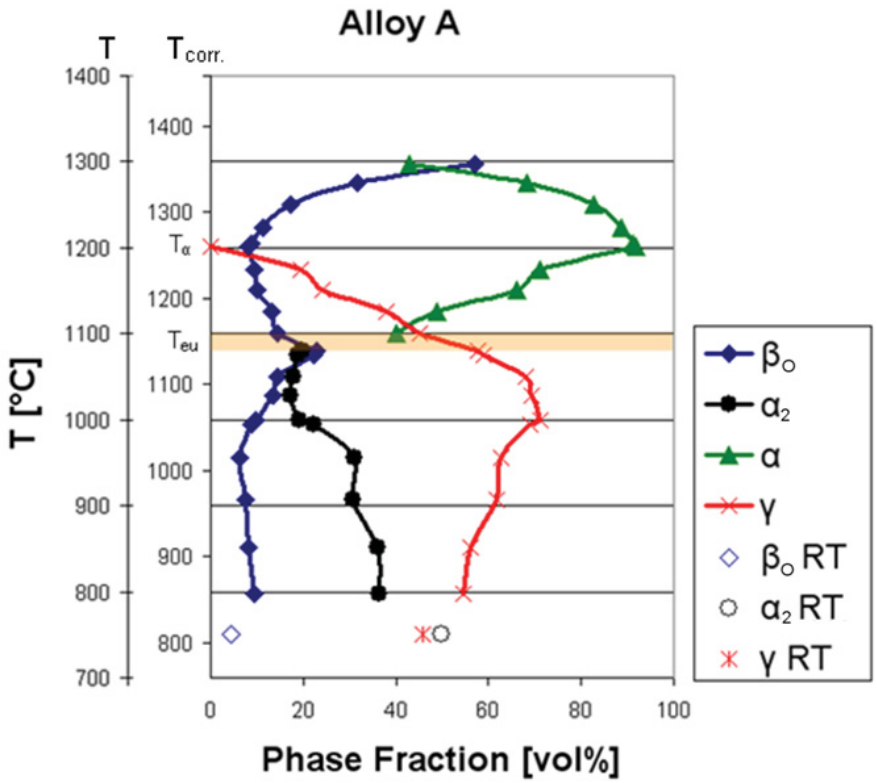

Fig. 31: Quantitative Rietveld evaluation of synchrotron data yielding phase volume fractions vs. temperature for alloy A.

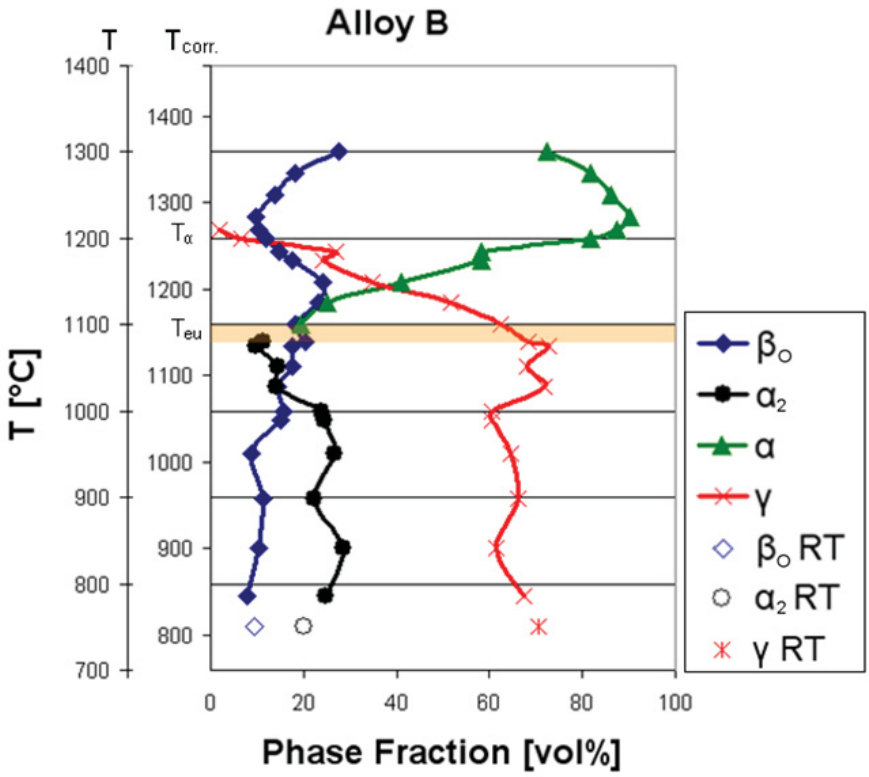

Fig. 32: Quantitative Rietveld evaluation of synchrotron data yieding phase volume fractions vs. temperature for alloy B.

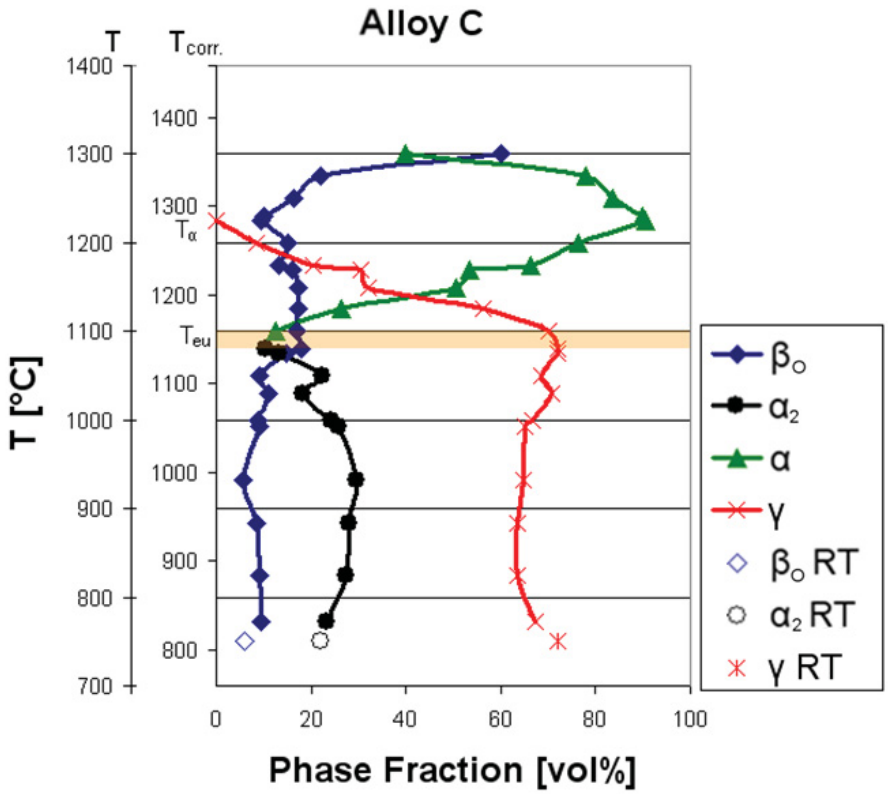

Fig. 33: Quantitative Rietveld evaluation of synchrotron data yielding phase volume fractions vs. temperature for alloy C.

The tendencies of the evolution of the phase fractions are in accordance with the thermodynamic calculations (see section 2.2). The synchrotron temperature record that was controlled by a pyrometer, however, differed slightly from the actual temperature and had to be adjusted. Liss et al. [42] found T_{α}=1269°C and $T_{eu=}$1169°C in neutron diffraction experiments for a TNM alloy containing 43.9 at% Al. Due to the higher Al-content T_{α} can be expected to be slightly higher for the alloy investigated by Liss et al.. The diagrams in Figures 31, 32 and 33 have two temperature axes. The right one, labelled $T_{corr.}$, shows the values corrected using the results of Liss et al.. After the temperature correction the results are also in agreement with the quantitative analyses of the β-phase content performed on the SEM-images using the software program Analysis (see section 2.5.1).
At room temperature the as-cast alloy A (see Fig. 31) is far from thermodynamic equilibrium and therefore the content of α_2 is higher and the γ-content lower than expected from thermodynamic calculations (see section 2.2). They approach their state of equilibrium as the sample is heated. However, it should be kept in mind that during the in-situ synchrotron experiments the samples were continuously heated, and therefore the system lacks the necessary time to attain equilibrium at any temperature investigated.
As calculated by Chladil [3], T_{α} as well as the temperature of the β-minimum are higher for alloys B and C than for alloy A. The same trend can be seen in the Rietveld fits. T_{α} for alloy A lies between 1260°C and 1265°C (see Fig. 31), which is in accordance with the value from the thermodynamic calculations by Chladil [3] using the modified database that determined T_{α}=1264°C (see section 2.2). The temperature of the ordering reaction $\alpha \rightarrow \alpha_2$, T_{eu}, is the same for all three alloys and lies at about 1160°C. This value lies considerably above the calculated value of T_{eu}=1117°C. This is also indicated by the quantitative analyses of the SEM micrographs (see Fig. 8), where the β-maximum is an indicator for T_{eu}.

Fluctuations in the course of the phase volume fractions have to be ascribed to the problems of the program to fit multiphase materials. Also, the locations of the alloying elements Nb and Mo are not entirely known, so that a simplified model had to be used to assess the phase fractions. In the model used for the fits, Nb occupies 50 % of the Al-positions in the β-phase. Mo is not accounted for. The same model was used to convert the phase fractions from m% to vol%, with the densities 3.79 g/cm^3 for γ, 4.06 g/cm^3 for α, 4.22 g/cm^3 for α_2, and 5.39 g/cm^3 for β_O [43].

Figure 34 summarizes the dependence of the β-phase volume fraction on temperature for the three investigated alloys.

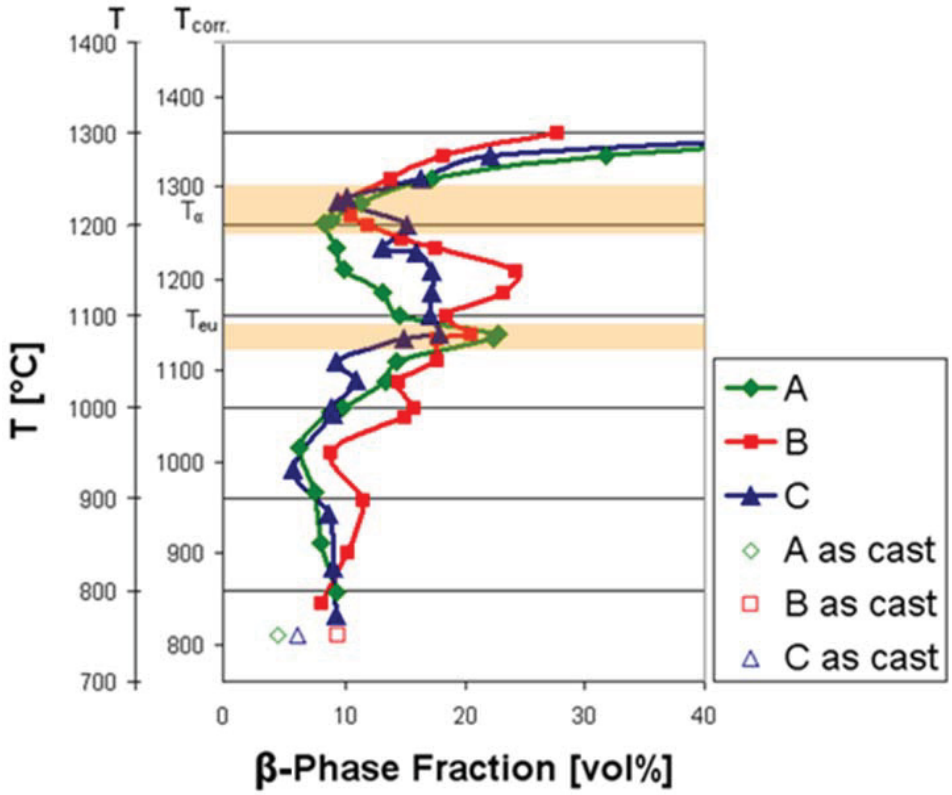

Fig. 34: Dependence of the β-phase volume fraction on temperature for alloys A, B and C. The results are obtained from quantitative Rietveld analyses of synchrotron data.

The β-minimum in alloy A possesses the lowest β-content with approximately 8.2 vol%. The β-contents for alloys B and C at T_α are 9.7 vol% and 9.4 vol%, respectively. The β-minimum temperature T_α for the two alloys, B and C, is also shifted to higher temperatures, lying at ca. 1260°C for A and 1285°C for B and C. Those values are higher than the calculated ones (see Fig. 2) that lie at ca. 1250°C for A and 1260°C for B and C using the original database. When comparing Figure 34 with Figure 2 it is evident that the experimentally determined minimum volume fractions of the β-phase are always smaller than the predicted ones. It is tempting to speculate that this behaviour is attributed to the relatively high heating rate during the experiment which renders the formation of β-phase difficult.

3.9.2 Neutron Data – Alloy TNM-B1

As already mentioned in section 3.7 the scattering lengths b_{Ti} and b_{Al} are very similar in their absolute value, but b_{Ti} is negative. In a disordered structure Ti and Al atoms are statistically arranged so that the average scattering length for every lattice site is almost zero and the diffraction signal disappears in the background. For ordered structures, however, there is a large difference in scattering length for Ti-positions and Al-positions which results in peaks with high intensity. The transition temperatures from ordered to disordered structures can therefore be rather easily determined using neutron diffraction.
Figure 35 shows neutron diffraction patterns of the TNM-B1 alloy for temperatures ranging from room temperature up to 1275°C.

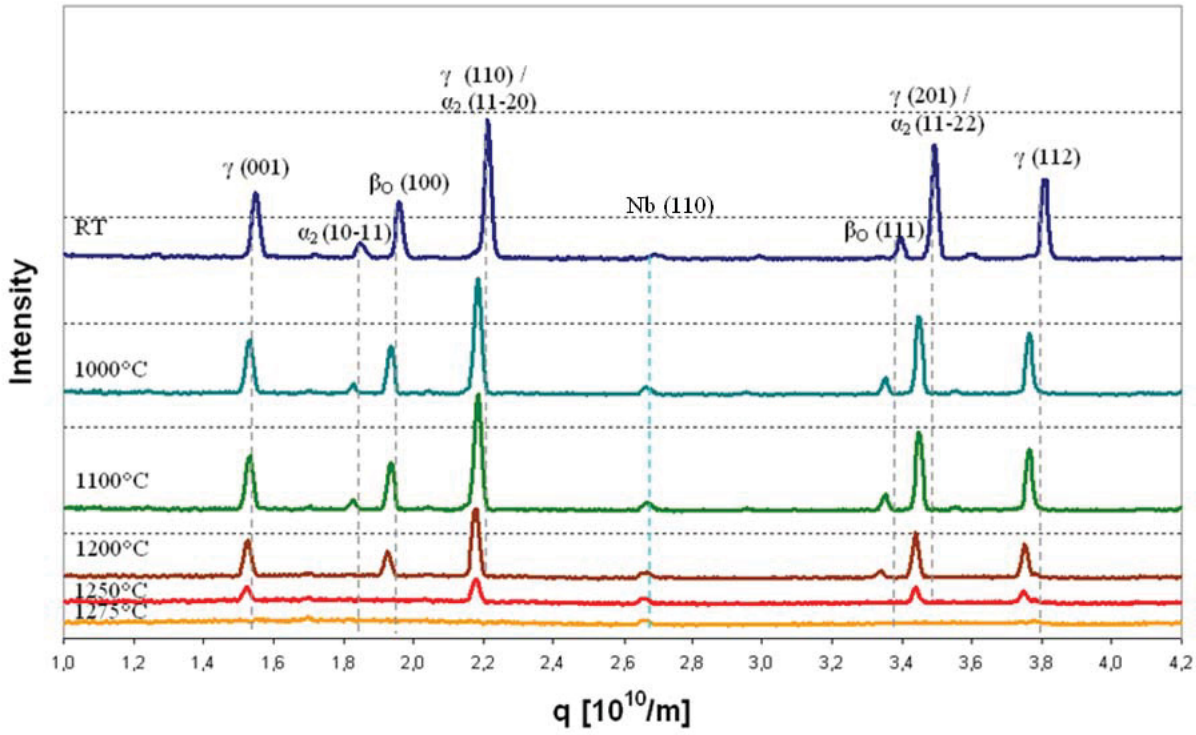

Fig. 35: Neutron diffraction patterns of the TNM-B1 alloy for different temperatures. The Nb (110) peak origins from the sample holders (see text).

All peaks in the patterns are superstructure peaks. At room temperature, 1000°C and 1100°C γ, α_2 and β_O are present. The small peak between q=2.65 and q=2.7, marked in the diagram with a turquoise dotted line, is a Nb (110) reflection from the sample holder used in the experiment. The only α_2-peak in the pattern that does not overlap with a γ-peak is the (10-11) peak at ca. q=1.85. It disappears between 1100°C and 1200°C so that the transition from α_2 to α, T_{eu}, must lie in this temperature range. Liss

et al. [42] investigated a TNM alloy containing 43.9 % Al in neutron diffraction measurements. At a heating ramp of 1 K/min T_{eu} was found to be at ca. 1169°C.
At 1200°C γ and β_O are still present, whereas at 1250°C only γ-peaks can be observed. Unlike predicted by the thermodynamic calculation for alloy A (see section 2.2), which has a composition very similar to TNM-B1, the $\beta_O \rightarrow \beta$ disorder takes place between 1200°C and 1250°C instead of 1445°C. This result is in agreement with the disorder temperature determined by Liss et al. [42] who found the $\beta_O \rightarrow \beta$ transition temperature at approximately 1212°C. At 1275°C the γ-peaks have disappeared as well so that only the disordered structures α and β remain in the material. Thus, T_α lies in the temperature range between 1250°C and 1275°C. Liss et al. [42] found T_α at ca. 1269°C.
A quantitative analysis of the data was conducted using the Rietveld method. The results are displayed in Figure 36.

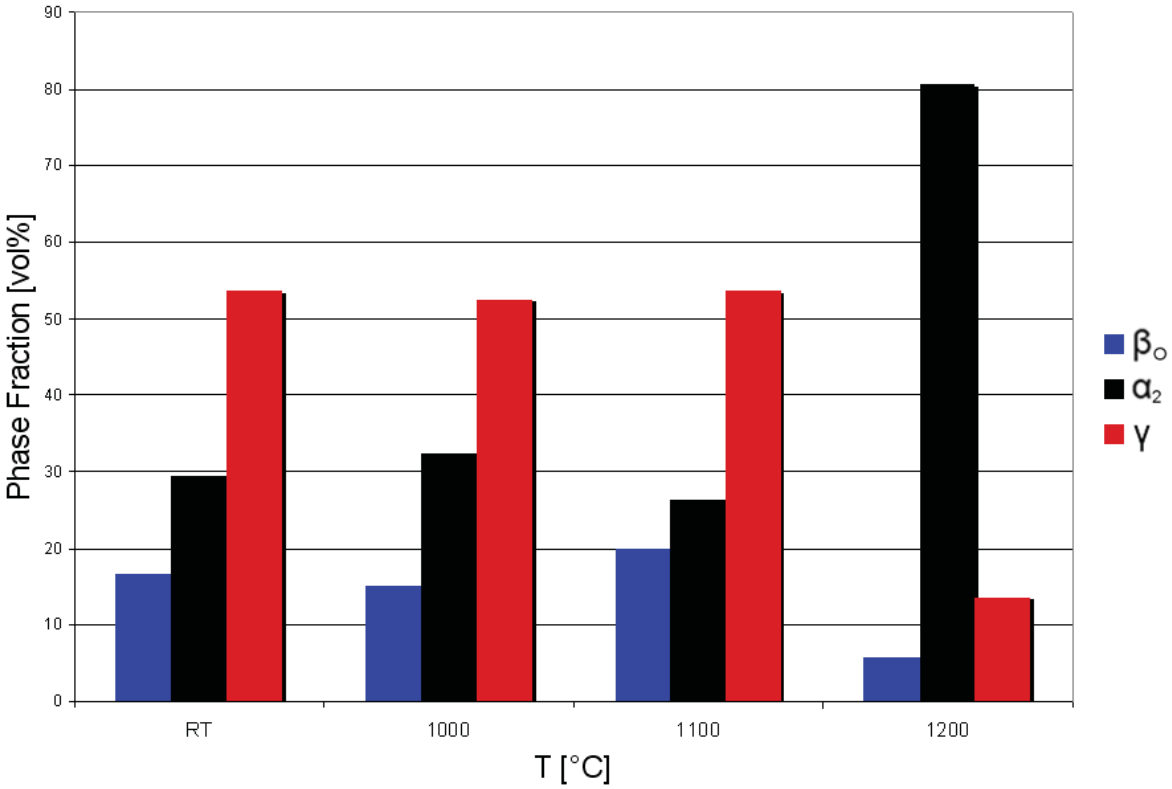

Fig. 36: Quantitative evaluation of phase fractions vs. temperature, obtained from neutron diffraction experiments.

The β_O-phase fraction as well as the γ-phase fraction decrease towards 1200°C. As expected, the α_2-phase fraction shows a strong increase from 1100°C to 1200°C.

3.9.3 Comparison of Synchrotron and Neutron Data

As described in sections 1.3.1 and 1.3.2 neutron and synchrotron radiation is scatterd differently by matter. In the special case of TiAl, possessing a so called “zero matrix” for neutrons, different information can be obtained from the two experiments.
High energy synchrotron radiation allows fast in-situ measurements. With those investigations modifications concerning the phase fractions can be uncovered as a function of temperature. Not all superstructure reflections can be observed though, so that neutron diffraction experiments are an adequate complement to synchrotron measurements. Because of the difference in scattering lengths of the two main alloying elements Ti and Al the material exhibits strongly pronounced superstructure peaks from neutron diffraction, whereas the “regular” peaks can not be distinguished from the background (see also section 3.7).
Figure 37 compares the diffraction patterns yielded by the two employed methods and illustrates that there are only a few peaks emerging from both. The red indices denote the superstructure peaks.

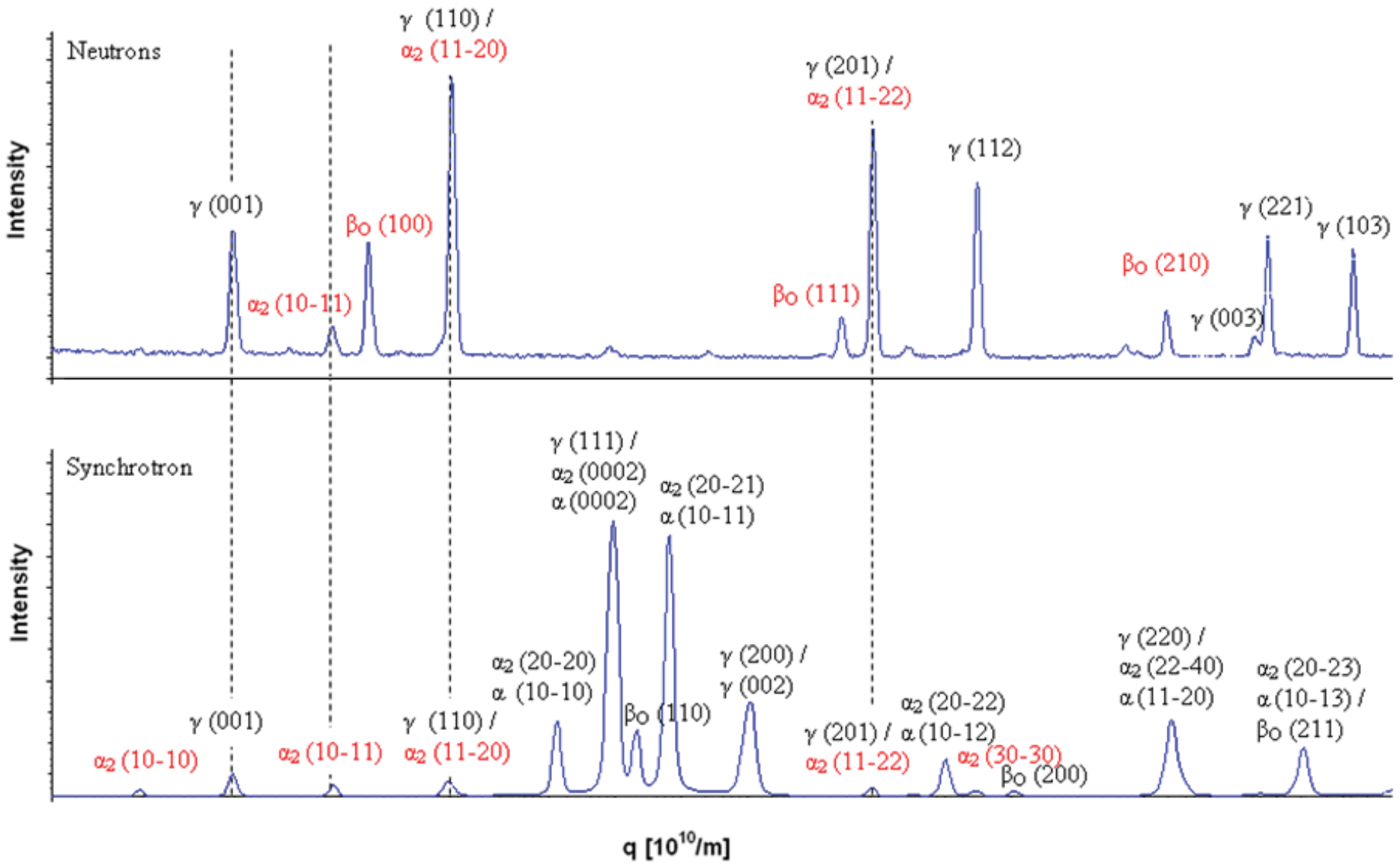

Fig. 37: Comparison of neutron and synchrotron diffraction patterns at room temperature.

All β_O- and α_2-peaks in the neutron diffraction pattern are superstructure peaks. The order → disorder transformations can therefore be observed at the temperatures where the peaks disappear. In the synchrotron diffraction pattern, however, general diffraction peaks can be observed, so that the occurrences of α and β can be quantitatively observed even above T_α.

4 Electron Backscatter Diffraction for Orientation Analysis

Electron Backscatter Diffraction (EBSD) is a microstructure characterization technique based on the evaluation of diffraction patterns, namely Kikuchi patterns. Those patterns can be obtained from crystalline samples in the SEM and the TEM. Their formation is based on the Bragg reflection of electrons that are inelastically scattered in the observed bulk material. Thus, the patterns provide the overall crystallographic information of the examined specimen, including the crystal structure and the orientation of the individual grains [44].
SEM Kikuchi patterns are nowadays indexed automatically through commercially available software packages that have been developed over the last 50 years. This is the main reason that EBSD has become a routine technique in materials science, since manual indexing is a laborious and time-consuming procedure [44].

4.1 Formation of Kikuchi Lines

For a more descriptive demonstration of the formation of Kikuchi lines their formation in the TEM will be described here first, since for reasons of geometry their formation is more easily understood from a simplified model. Referring to this first model, the connection to Kikuchi line formation in the SEM will be drawn.

When an electron beam enters a crystal, diffuse inelastic scattering of the electrons occurs in all directions, with a maximal intensity in the direction of the primary beam. The emerging scattered beams only marginally differ in energy and thus in wavelength and can be considered as new ”primary beams“ [45].
The new ”primary beams“ arrive at the lattice planes from every angle for every set of lattice planes, as shown in Figure 38.

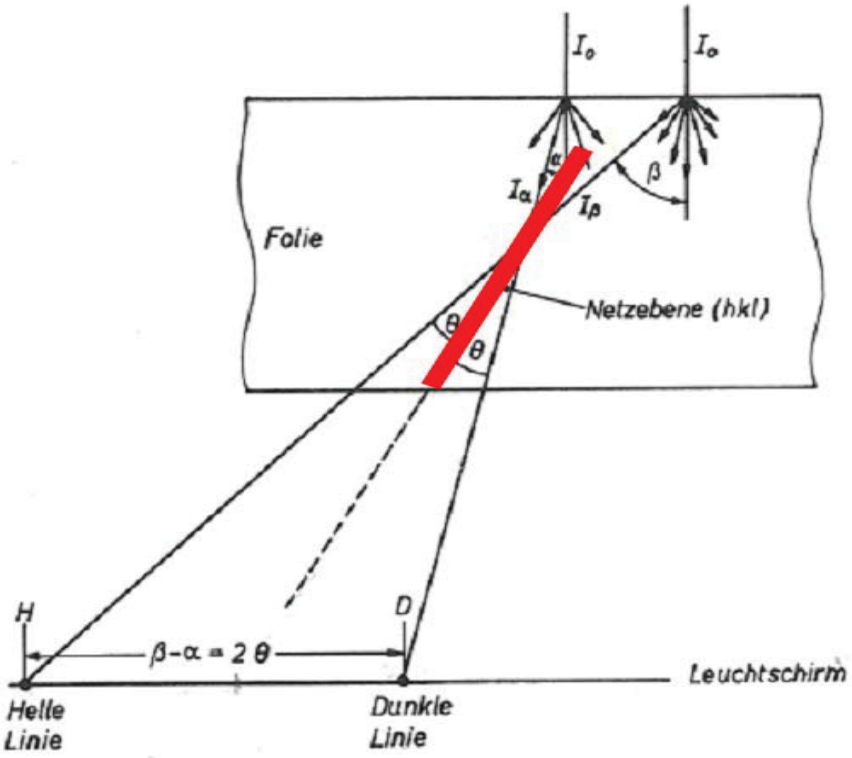

Fig. 38: Geometry of the scattered electron beam in a TEM sample [45].

The electrons arriving at the Bragg angle θ_B are thus diffracted forming a cone, called Kossel cone, around the normal of the lattice plane on both sides of the plane with the apex angle of $2(90° - \theta_B)$. The wavelength λ of the electron radiation can be found by inserting typical values for the accelerating voltage U into Equation 19 that is deduced from the de Broglie relation:

$$\lambda = \frac{h}{\sqrt{2meU}} = \frac{h}{\sqrt{2m_0eU \cdot \left(1 + \frac{eU}{2m_0c^2}\right)}} \qquad \text{(Equ. 19)}$$

With λ and the lattice parameter d of the analyzed material inserted into Equation 20, Bragg's law,

$$n \cdot \lambda = 2d \cdot \sin\theta_B \qquad \text{(Equ. 20)}$$

the Bragg angle θ_B can be assessed to be very small, resulting in an apex angle of the Kossel cone of almost 180°. Figure 39 illustrates a schematic sketch of the described geometry [44,45].

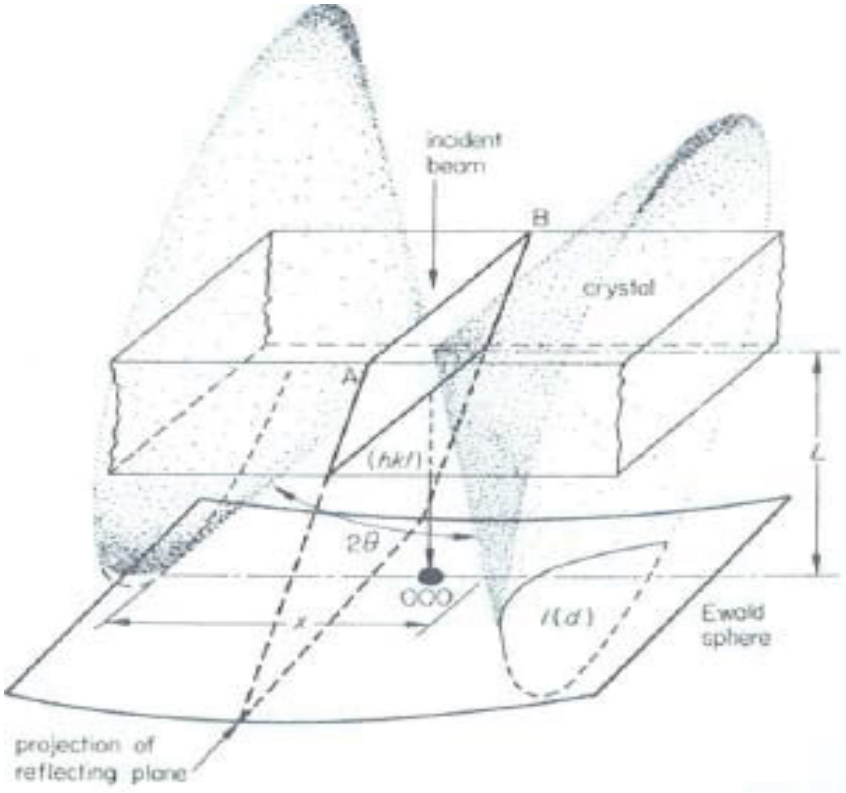

Fig. 39: Formation of a Kikuchi band in the TEM [45].

The resulting intersections of the Kossel cones with the recording screen are called Kikuchi lines, which, due to the very big apex angle of the cones, appear to be straight, parallel lines.

Since electron beams that are scattered at a higher angle show lower intensities, for every set of lattice planes one dark line (defect line) and one bright line (excess line) can be seen on the Kikuchi pattern, resulting from the Kossel cones reflected on the two sides of the plane. This occurrence is sketched in Figure 38 showing the two electron beams scattered at angles α and β. The beam scattered at the smaller angle α shows only a minimal change in direction compared to its original direction. Consequently, it loses intensity only marginally and results in the excess line of the Kikuchi band. The second beam is scattered at the bigger angle β and results in the less intense defect line. The angular distance between the defect line and the excess line is $2\theta_B$ and therefore proportional to the inter-planar distance as can be seen in Figure 38.

A Kikuchi pattern, as shown in Figure 40 comprises parallel pairs of lines, so-called bands, that consist of an excess and a defect line.

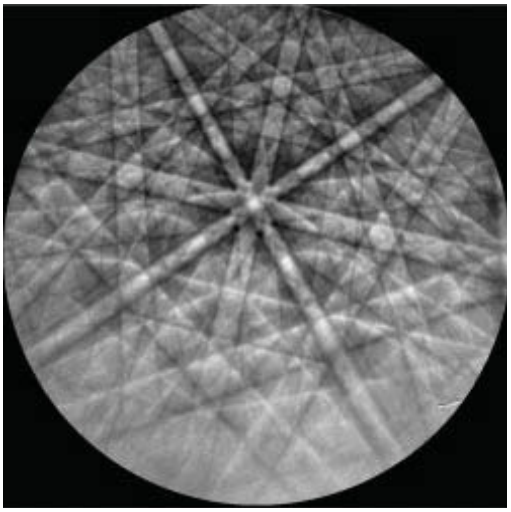

Fig. 40: Example of EBSD Kikuchi pattern [46].

In the Kikuchi pattern the zone axes of the crystal are displayed as the intersections of those so called bands that show the angular relationships in the crystal and hence embody the crystal symmetry [44,46].

To compare the formation of Kikuchi lines in the TEM and the SEM, Figure 41 shows the optical path of the electron beam for the formation of one pair of Kikuchi lines corresponding to one lattice plane in the SEM.

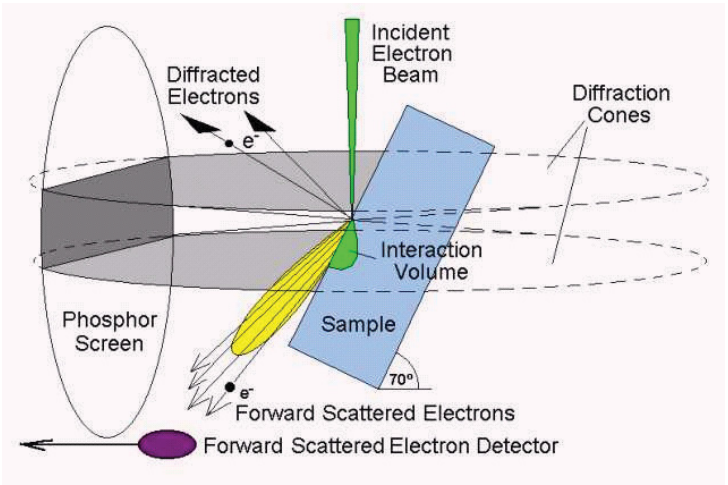

Fig. 41: Sketch of the formation of one Kikuchi band in SEM [47].

In this case, the electron beam is not transmitted through the specimen, but the backscattered ”primary beams“ only interact with the lattice planes in the surface area. In order to increase the intensity of the detected backscattered electrons on the screen, the specimen is tilted at 60-70° from the horizontal so that more electrons can be diffracted and travel towards the detector [44].

4.2 Comparison of Kikuchi Patterns in TEM and SEM

A major division of texture determination techniques into macrotexture techniques, that are based on X-ray and neutron diffraction, and microtexture techniques, that are based on electron diffraction, is made by V. Randle and O. Engler [44]. The primarily used technique for microtexture imaging is through the evaluation of Kikuchi patterns. Other possibilities exist, including selected area diffraction or the micro-Kossel technique that will not be further discussed in this work.
Though formed under different conditions, the principles of formation are equal for TEM and SEM Kikuchi patterns, so that they can be interpreted following the same principles [44].

4.3 Evaluation of EBSD Patterns

To improve the pattern quality the background that forms due to electrons of all energies scattered from the sample has to be removed from the recorded image prior to the evaluation of the patterns. This background can be recorded by screening several grains to average out the background information that is subsequently subtracted from or divided into the original pattern image [44,46].
For automated pattern recognition and evaluation Krieger Lassen et al. [48] and Kunze et al. [49] adopted the Hough transform to EBSD patterns after several other attempts to overcome problems with the recognition of low contrast bands [44]. For an easier detection by computer codes, lines in the image space are transformed into points in the Hough space under consideration of their intensities. The description of a straight line by the parameters k and d of the linear equation y=kx+d, where k is the slope and d the axis intercept on the y axis, seems to be the most apparent transformation, though problems arise from this method for lines parallel to one of the axes. It is therefore better to parameterize a line using the angle θ that describes the angle between the normal to the line and the x-axis, and the distance ρ between the straight line and the origin of the coordinate system. The equation of the line is then [46]:

$$\rho = x \cdot \cos\theta + y \cdot \sin\theta \qquad \text{(Equ. 21)}$$

The thereby generated sinusoid in the Hough space corresponds to one point in the image space, to which it is unique. If two curves in the Hough space are

superimposed, their intersection corresponds to the parameters for the line that passes through the two points in the image space, as outlined in Figure 42 [46].

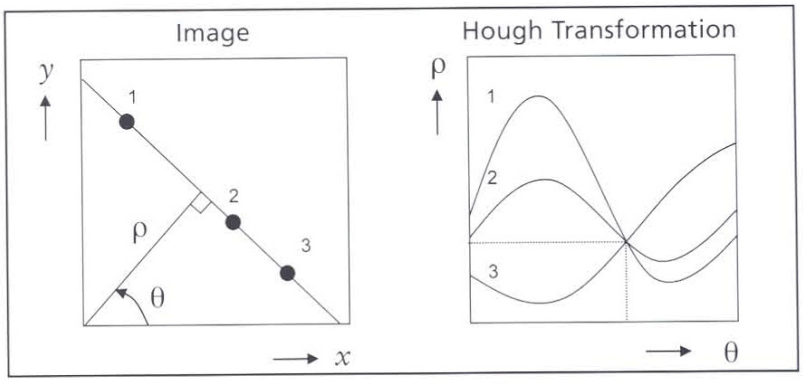

Fig. 42: Principle of the Hough transform [46].

For automated indexing of the Kikuchi diffraction pattern, the points in the Hough space and their values for θ and ρ can be determined through the implementation of a specific filter. Additionally, the knowledge of an average ”standard profile“ of the peaks in the Hough space is necessary to identify them and relate them to the lines in the original image [44].

4.4 Experimental Setup in the SEM

The basic system components of the employed EBSD experimental setup are as follows:

- A tilted sample,
- A phosphor screen on which the pattern forms due to the fluorescence caused by the reflected electrons from the sample,
- A sensitive charge coupled device (CCD) camera to map the pattern on the phosphor screen,
- A vacuum interface to arm the CCD camera and the phosphor screen on the SEM (This device can be retracted into the SEM chamber when not in use),
- Electronic hardware to control the SEM and a computer that controls the EBSD experiment and analyses and displays the results [46].

Figure 43 shows the components of an EBSD system in the experimental setup.

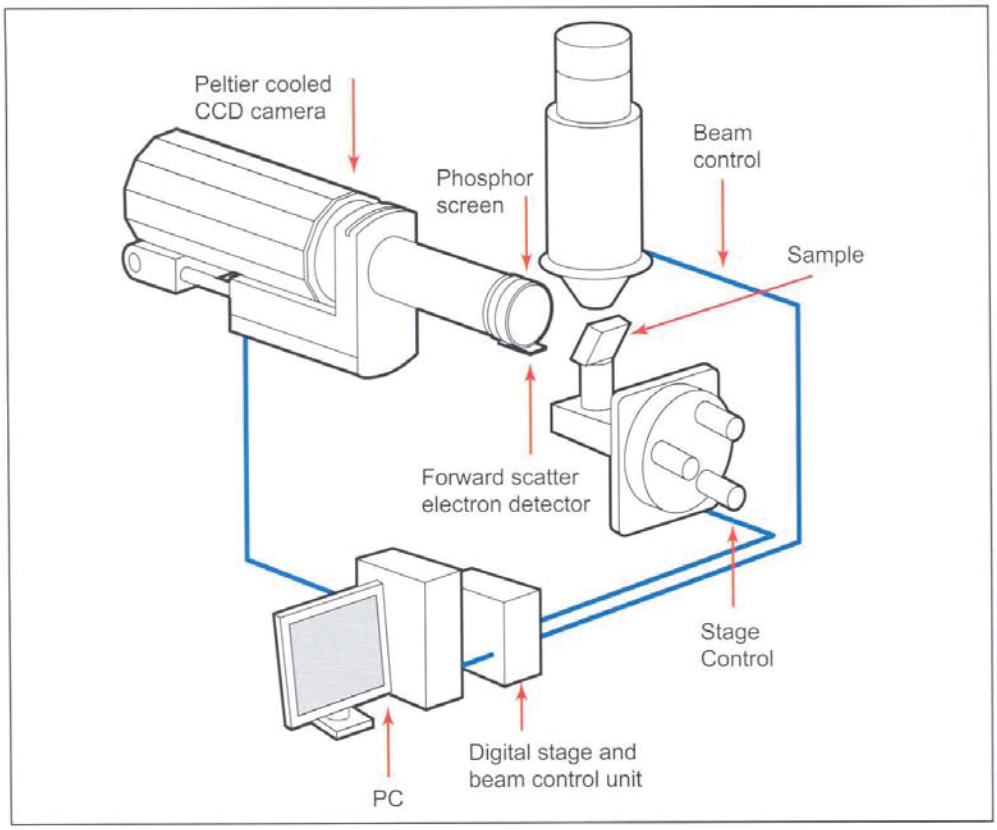

Fig. 43: EBSD experimental setup [46].

4.5 Operating Conditions

The accuracy of the generated pattern does not only depend highly on the operating conditions in the microscope but also on the material and the sample preparation [44,46]. Those influencing factors will be discussed in the following.

4.5.1 Material and Sample Preparation

With increasing atomic number of the investigated material the rate of backscattered electrons also increases, leading to clearer and more detailed patterns. Since the sample is tilted at ca. 70°, the electron beam only interacts with the top 10-15 nm of the specimen. Therefore, the area close to the specimen surface has to be representative of the material. Surface deformation that can occur due to grinding and polishing can unfavorably influence the diffraction pattern and lead to misinterpretation of the acquired data. Depending on the material it can therefore be necessary to polish the specimen electrolytically in order to avoid mechanical damage to the surface region. Care must be taken to prevent the formation of

embossment and resulting impairment of the pattern recording, especially at grain boundaries [44].
If the specimen has to be mounted for preparation, conductive hot mounting resin should be used. This improves the working conditions in the SEM compared to establishing an electrical contact through conductive tape or a sputtered surface layer. Materials that contaminate and oxidize easily may have to be prepared immediately prior to EBSD examination or can alternatively be plasma cleaned [44].

4.5.2 SEM Geometry

The main adjustable parameters in the geometric experimental set-up are the specimen tilt, the working distance and the camera position. The camera position usually remains fixed, whereas the specimen tilt and the working distance are adjusted in order to improve the contrast and the pattern quality [44,46].
The working distance has to be chosen in order to detect the backscattered electrons on the camera. Very short working distances should be avoided to exclude the risk of collision with microscope hardware. The recommended working distance lies in a range of 15 – 25 mm [44].
Kikuchi patterns can be monitored above tilt angles of 45°. Higher tilt angels are usually adopted to further shorten the electrons' path lengths in the material and to raise the pattern contrast. Due to the anisotropy and image distortion arising from tilt angles above 80° a tilt of 70° has been found to be a good compromise [44]. Because of the specimen tilt, the working distance changes as the beam scans down the sample. Therefore, the image defocuses and is foreshortened. Some EBSD systems can counteract those effects if working distance calibration is carried out at two different distances. Those systems automatically adjust the focus and possible shifts in the pattern centre by interpolation [46].

4.5.3 Microscope Setting

The interaction volume of the electron beam with the sample changes linearly with the accelerating voltage, so that a small accelerating voltage allows good spatial resolution, as required for fine-grained or deformed material. A higher accelerating voltage can be applied for high atomic number elements. The advantages of high accelerating voltages are the increasing efficiency of the phosphor screen with increasing electron energy producing a brighter diffraction pattern, reduced interference from surrounding electromagnetic stray fields and the further penetration of the electron beam into the specimen, which diminishes surface contamination and

damage effects. There are also drawbacks to a high accelerating voltage, which contain the reduction of spatial resolution and the necessity to coat samples that are bad conductors or are very easily damaged by the electron beam. 20 kV can be seen as a general reference value for the accelerating voltage, though the actual value depends highly on the examined material and the sample condition [44].
The probe current is adjusted to the light sensitivity of the camera and usually not modified for the improvement of the spatial resolution, except in cases where the accelerating voltage has to remain a fixed value. Furthermore, the best absolute resolution, i.e. the smallest probe current, does not correspond to the best working condition, since a small interaction volume entails insufficient pattern clarity. This deteriorates the automatic pattern recognition and indexing which means that a compromise has to be found between resolution and pattern clarity. Under optimum operating conditions, grains down to dimensions of 10 nm can be determined [44,46].

4.6 Lamellar Structure Formation in TiAl

During cooling α_2+γ-lamellar colonies are formed from the α-phase field by the precipitation of γ-lamellae. The lamellae are related according to the Blackburn orientation relationship (see Equ. 3). At T_{eu} the remaining α-lamellae order to α_2. All α_2-lamellae in one colony exhibit the same orientation since only one possible orientation variant exits for the $\alpha \rightarrow \alpha_2$ transformation. The habit planes of the two crystal structures that are aligned parallel to each other are the closest packed planes, $\{111\}_\gamma$ and $(0001)_{\alpha_2}$. During this precipitation the stacking sequence ABAB in the hexagonal phase is shifted to ABCABC of the face centered structure [50]. The ordering of the γ-phase leads to the tetragonality of the γ-phase and to the formation of three different orientation variants since the <110] direction and the other two <011] directions are not equivalent in the tetragonal structure. Figure 44 shows a γ-unit cell indicating the different sequences of atoms [50]. Given those three possible domains and the two twins, resulting from the two different stacking sequences there are six possible orientation variants for the γ–lamellae [50,51]. The nucleation and ordering of the γ phase is further discussed in [52]. It should be kept in mind that in the samples investigated in this thesis the γ-lamellae are mainly precipitated from the supersaturated α_2-grains. It is not in the scope of this work to describe this particular process. For further information the reader is referred to [53].

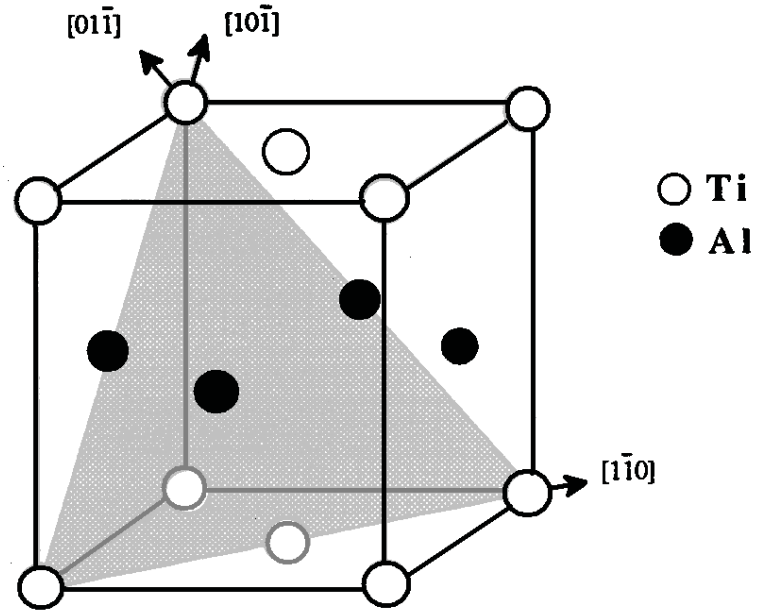

Fig. 44: γ-TiAl unit cell [50].

It has, however, been observed by Denquin et al. [15] that after discontinuous precipitation, every secondary lamella is a single variant and does not show any order domain boundary.

4.7 EBSD Experimental Setup and Sample Preparation

The EBSD measurements were performed on a Zeiss SEM EVO50. The usual experimental setup was used as described in section 2.4. Pixel sizes between 0.02 and 0.05 μm^2 were achieved at an accelerating voltage of 25 kV.
The samples were first grinded and polished using standard metallographic techniques. In order to obtain a deformation-free surface the specimens were then polished electrolytically on a Lectro Pol-5 polishing unit using the A3 electrolyte, both provided by Struers. Viable results were obtained for polishing for 10 s at 20°C, 40V and a flow rate of 7. For an optimised pattern quality the material was plasma cleaned for 1 h before the measurements in order to minimise contaminations.

4.8 Results and Discussion

Is has been discussed in section 2.5.2 that upon a two step heat treatment the alloy TNM-B1 exhibits a cellular reaction starting at 900°C that is completed after 100 h at 1100°C. To learn more about this process, EBSD measurements were performed in order to find orientation relationships of the emerging phases. The EBSD technique is not able to distinguish the six possible tetragonal γ-variants, since the c/a-ratio of the lattice parameters of the γ-phase is too close to one [10].

Figure 45 shows a SEM image of a lamellar colony consisting of secondary α_2 and γ-lamellae after the first heat treatment at 1230°C for 1 h.

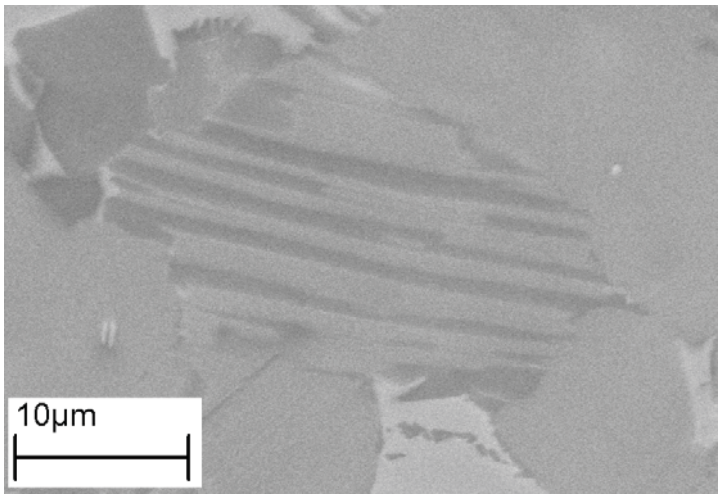

Fig. 45: SEM-BSE image of a secondary α_2+γ-colony after 1 h at 1230°C and AC.

The phases shown in Figure 45 are displayed separately with the respective pole figures in Figure 46.

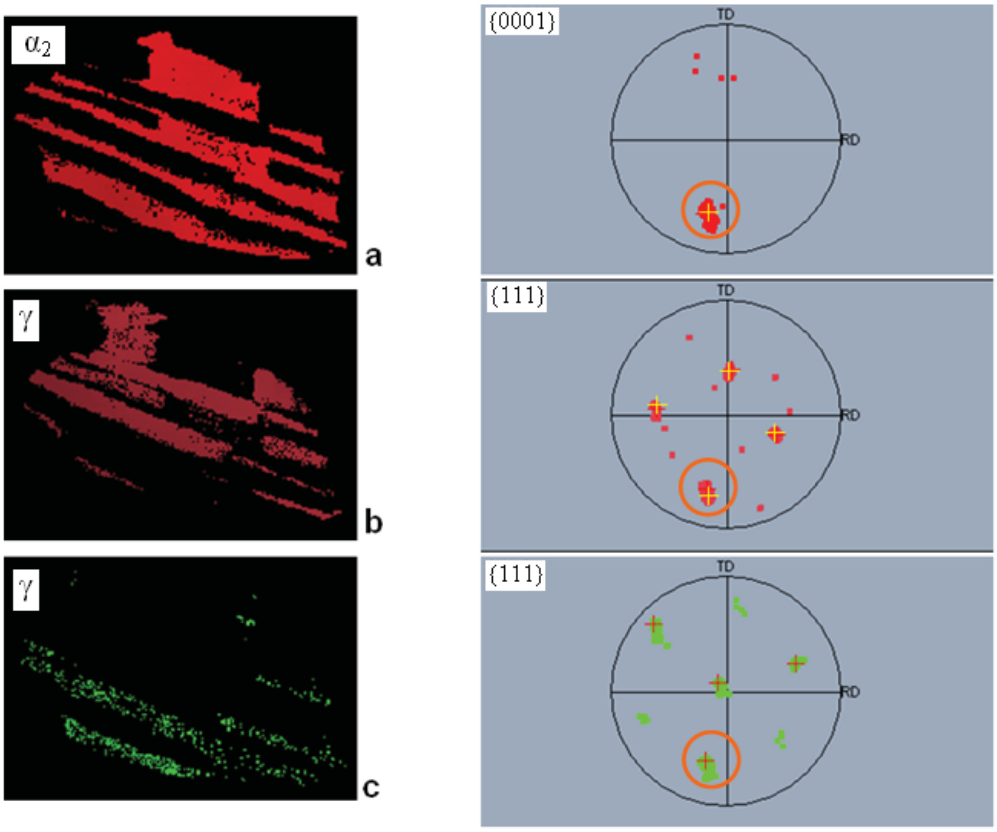

Fig. 46: Orientation of secondary α_2- and γ-lamellae in a specimen heat treated for 1 h at 1230°C followed by cooling. a) displays the α_2-lamellae, b) and c) show two variants of γ-lamellae. The orange circles in the pole figures indicate the reflection of parallel close packed planes, i.e. $\{0001\}_{\alpha_2} \| \{111\}_{\gamma}$.

Figure 46a shows secondary α_2-laths and the corresponding stereographic pole figure of the {0001}-orientation. Figures 46b and c show γ-laths and their pole figures for the {111}-planes. Both exhibit different orientations that are related to the orientation of the α_2-lamellae through the Blackburn orientation relationship (see section 2.1). The orientation shown in the pole figure of 46c is a twin of a different domain of the γ-orientation in the pole figure of 46 b. The orange circle marks the respective reflex of the parallel planes.

A β_O-grain with precipitated γ-particles can be seen in Figure 47. The reason for the observed decomposition process can be attributed to the high β-content present at temperatures above T_α. During AC the β-fraction is reduced by the formation of γ-phase.

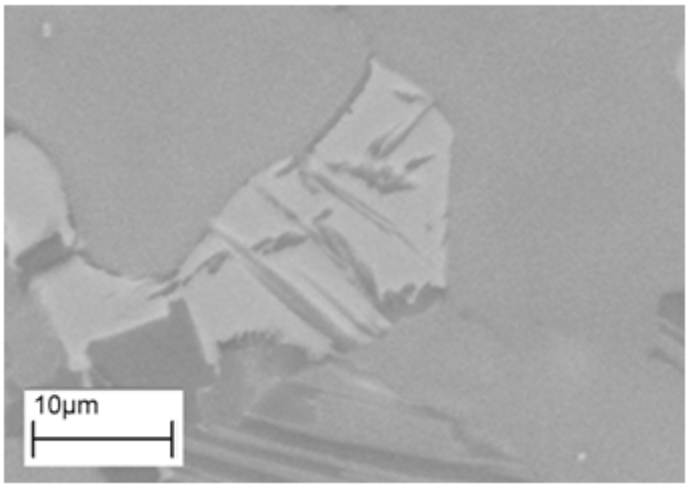

Fig. 47: SEM-BSE image of a β_O-grain after 1 h at 1230°C and AC showing precipitated lens-shaped γ-particles.

The corresponding pole figures are displayed in Figure 48a and b. Figure 48a shows the remaining β_O-grain and its pole figure. Figure 48b shows the emerged γ-phase and its orientation.

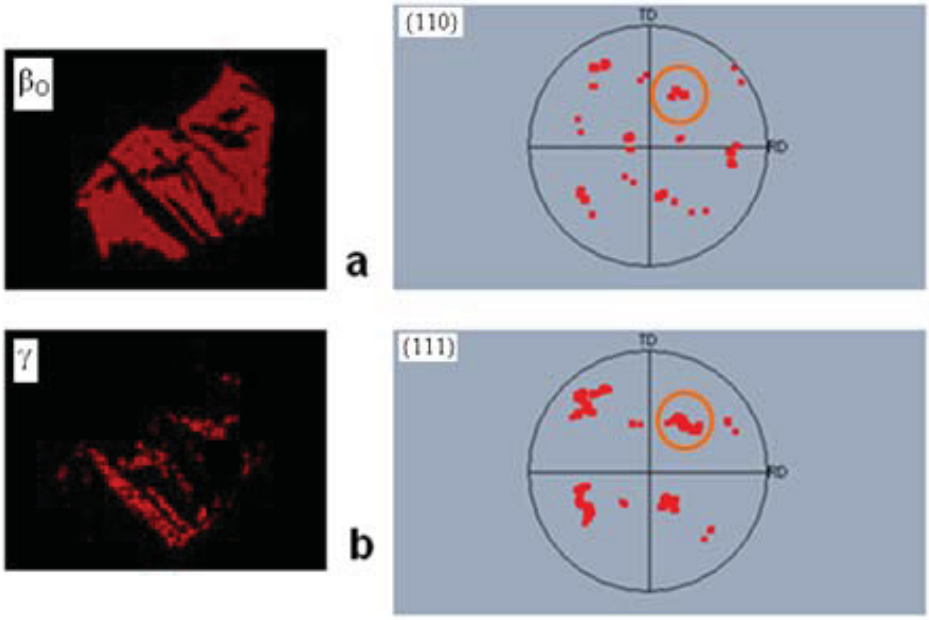

Fig. 48: Pole figures of a β_O-grain in a) and of γ that precipitates in β in b).

Since β_O is cubic and γ is tetragonal, not all the reflections appear at the exact same angles. However, the following orientation relationship can be observed:

$\{111\}_{\gamma} \| \{110\}_{\beta_O}$.

Figure 49 shows a β_O-grain after a two-step heat treatment.

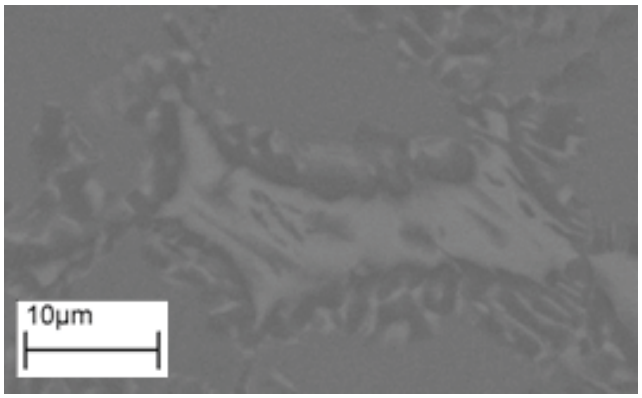

Fig. 49: SEM-BSE image of a β_O-grain decomposing into β_O+γ after 1 h at 1230°C/AC and 6 h at 950°C/FC.

The corresponding pole figures for β_O and γ are displayed in Figure 50.

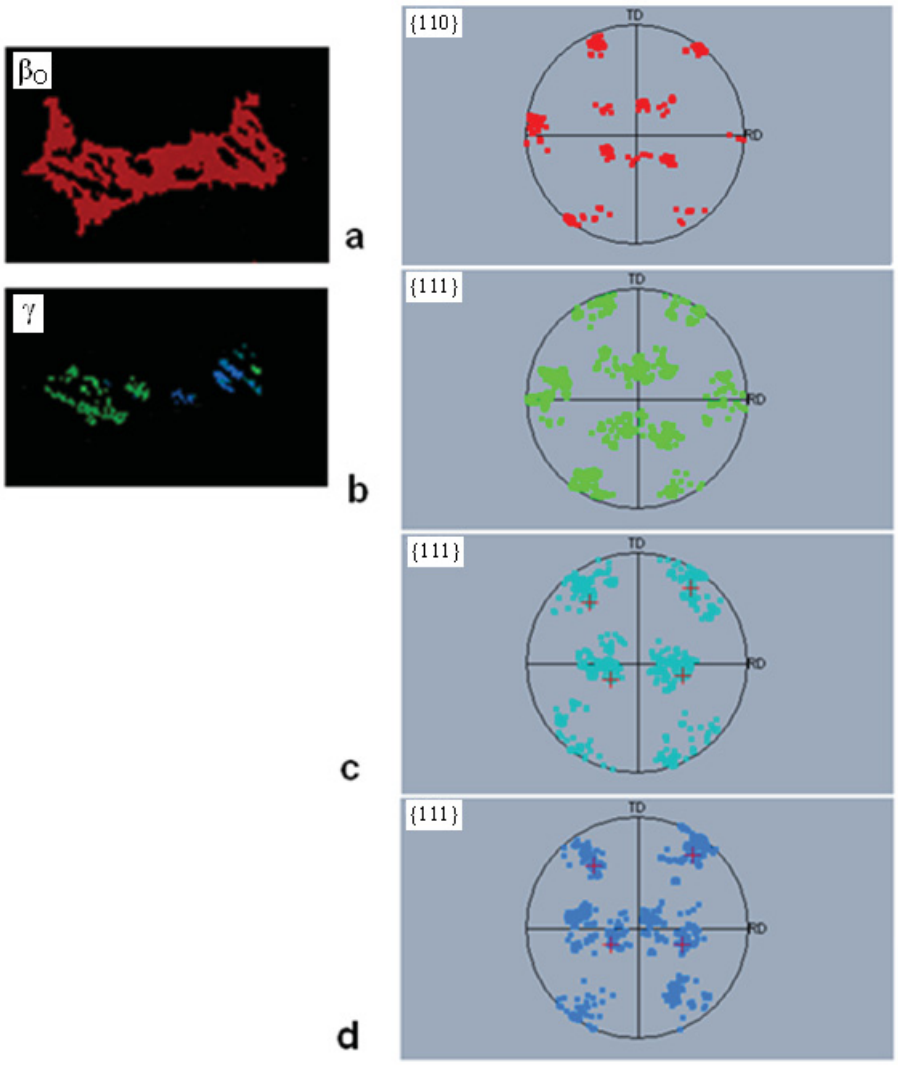

Fig. 50: a) {110} pole figure of the β_O-grain, b) to d) show the {111} pole figures of the appearing γ-variants.

The $\{110\}_{\beta_o}$ -pole figure that gives evidence of the occurrence of twins can be seen in Figure 50a. The {111}-pole figures of γ-variants emerging from the β_O-grain are displayed in Figures 50b, c and d. Different domains and twins occur in γ that exhibit the same orientation relationship with the original β_O-grain as described in the last paragraph.

A part of the microstructure that underwent a cellular reaction after annealing at 1230°C for 1 h and subsequent air cooling followed by 6 h at 950°C and furnace cooling can be seen in Figure 51, where α_2, γ and β_O are present.

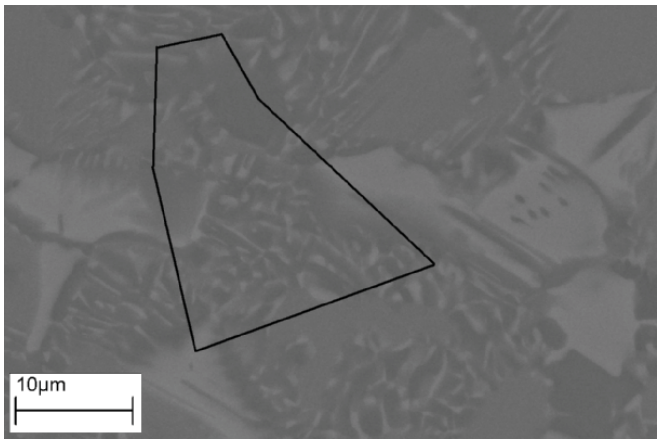

Fig. 51: SEM-BSE micrograph of the EBSD working range for the pole figures summarized in Figure 52. The selected area shows the presence of cellular reaction.

The marked area depicts the working range for EBSD analysis. Figure 52 shows the associated pole figures for α_2 in Figure 52a, γ in Figure 52b as well as β_O in Figure 52c.

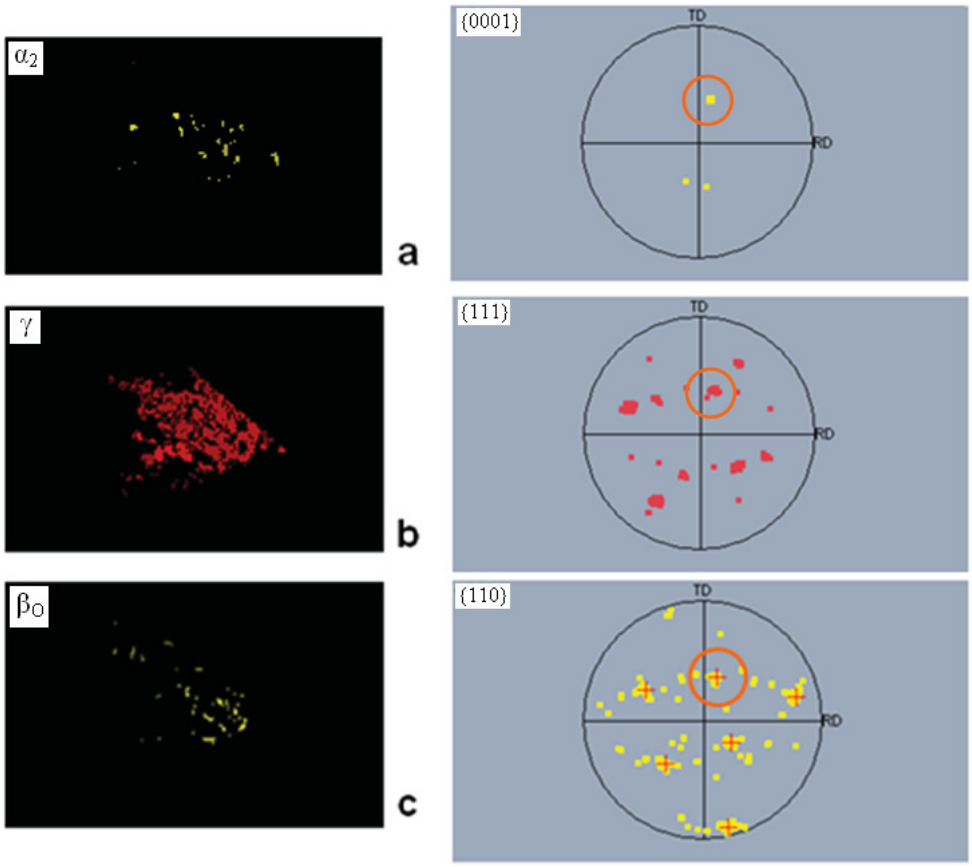

Fig. 52: Pole figures of an area transformed by cellular reaction. The orange circles in a), b) and c) show the orientations of the parallel close packed planes of α_2, γ and β_O, respectively.

The respective closest packed planes are parallel and the three phases are related through the following orientation relationship:

$\{0001\}_{\alpha_2} \| \{111\}_{\gamma} \| \{110\}_{\beta_O}$. The orange circles in Figure 52 mark the reflection from the respective parallel planes. Similar results of orientation relationships in γ-TiAl based alloys have been reported by [54].

An indication of the formation of γ-grains through recrystallization concurrently to discontinuous precipitation is given by EBSD measurements of a sample after 100 h at 1100°C (SEM micrograph see Fig. 14d). The EBSD pole figures are displayed in Figures 53 and 54, respectively.

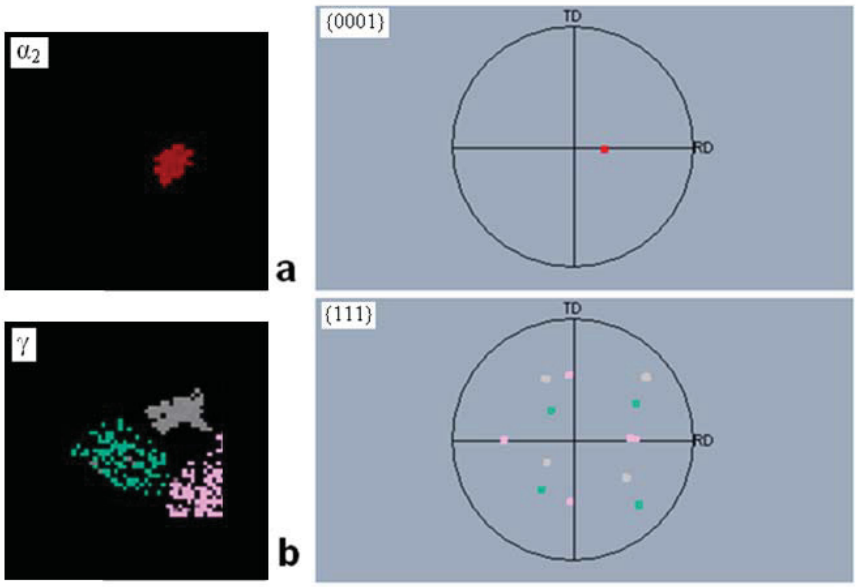

Fig. 53: a) α_2-grain with pole figure; b) adjacent γ-grains and corresponding pole figure. They show no orientation relationship.

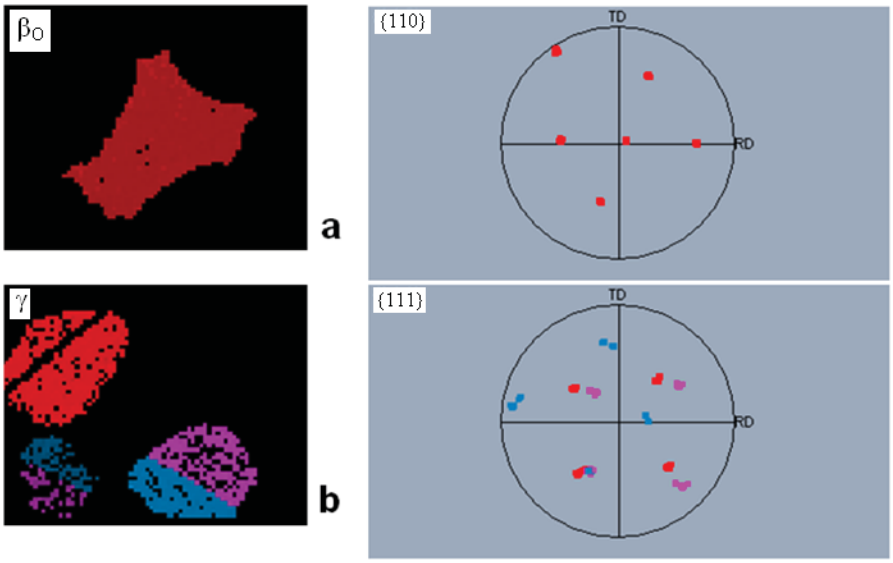

Fig. 54: a) β_O-grain and corresponding pole figure; b) γ-grains with their pole figure. No orientation relationship can be observed.

From the pole figures it is evident that adjacent α_2- and γ-grains as well as β- and γ-grains show no special orientation relationship.

5 Microstructure and Properties

In order to describe the lamellae formation and relate the lamellae spacing to mechanical properties TEM investigations, hardness measurements and XRD-scans were performed on specimens of the TNM-B1 alloy FD_MTU05 out of the same heat as FD_MTU03, in the present work called TNM-B1. The performed heat treatments are listed in Table 4:

Tab. 4: Heat treatments conducted on FD_MTU05 material.

	1st heat treatment step				2nd heat treatment step		
# 1	1230°C	1h	AC				
# 2	1230°C	1h	AC	+	850°C	6h	FC
# 3	1230°C	1h	AC	+	900°C	6h	FC
# 4	1230°C	1h	AC	+	950°C	6h	FC

Those investigations were motivated by the observation that specimens heat treated according to # 4 show a higher tensile ductility at room temperature than specimens heat treated according to # 2. The room temperature tensile tests were conducted by Gopal Das [23] at Pratt & Whitney, USA. The results of the tensile tests are summarized in Table 5.

Tab. 5: Mechanical properties of FD_MTU05 material obtained from room temperature tensile tests after heat treatments at different temperatures [23].

Heat treatment	Tensile Strength [MPa]	Yield Stress [MPa]	Modulus [GPa]	Total Strain to Failure [%]	Plastic Strain to Failure [%]
# 2	972	793	157	1.95	1.55
# 4	1046	868	157	3.5	3.1

Figure 55 shows XRD-scans of the TNM-B1 alloy at the four heat treatment states listed in Table 4.

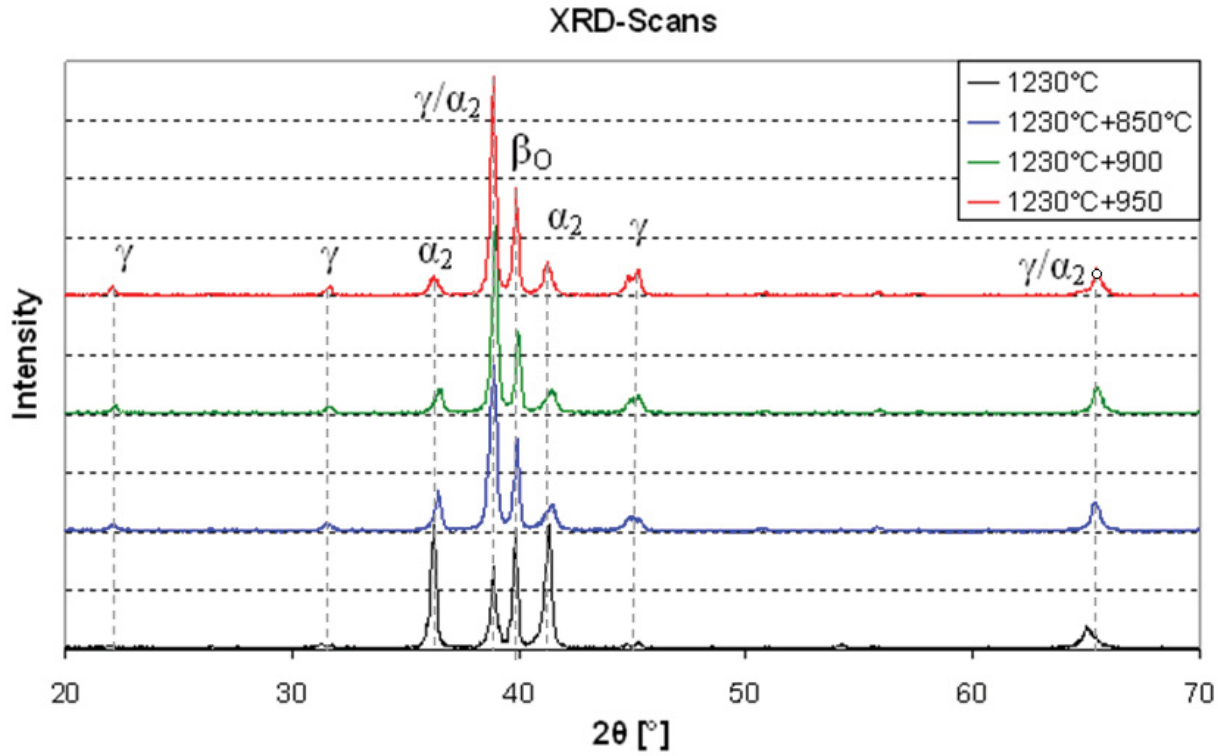

Fig. 55: XRD-scans of samples in the four heat treatment states (see Table 4). The intensities of the γ-peaks increase, the intensities of the α_2-peaks decrease with increasing temperature of the second heat treatment.

After the first heat treatment at 1230°C the intensities of the γ-peaks are very low and only little γ can be found in the material. The α_2-peaks exhibit high intensities after the first heat treatment, indicating a high amount of oversaturated α_2-grains. After a second heat treatment at 850°C the γ-amount increases considerably at the expense of α_2. For heat treatments 3 and 4, at 900°C and 950°C, respectively, the patterns do not show significant changes and the phase distributions stay almost identical. A β_O-peak can be observed in the XRD-pattern that does not considerably change its intensities after the different heat treatments, meaning the volume fraction of β_O-phase remains constant.
During extrusion and forging most of the deformation is provided by the β-phase. β exhibits a bcc structure with high stacking fault energy. As a consequence, dynamic recovery takes place predominantly and dynamic recrystallization of the β-phase is impeaded, therefore the deformation texture of the β-phase persists. It is hence very difficult to perform Rietveld analysis of XRD-data of this material, so that the patterns shown in Figure 55 can only be evaluated quantitatively in terms of phase fractions.

The γ that forms during those heat treatments precipitates in the oversaturated α_2-grains in form of very fine lamellae. This can be observed in TEM micrographs taken

for different heat treatment states. The TEM images of lamellar colonies after heat treatments at 1230°C/1h/AC, 1230°C /1h/AC + 850°C/6h/FC and 1230°C /1h/AC + 950°C/6h/AC are shown in Figures 56a to c, respectively. The micrographs were recorded in the $<110]_{\gamma} \parallel [2\bar{1}\bar{1}0]_{\alpha_2}$ zone axis [25].

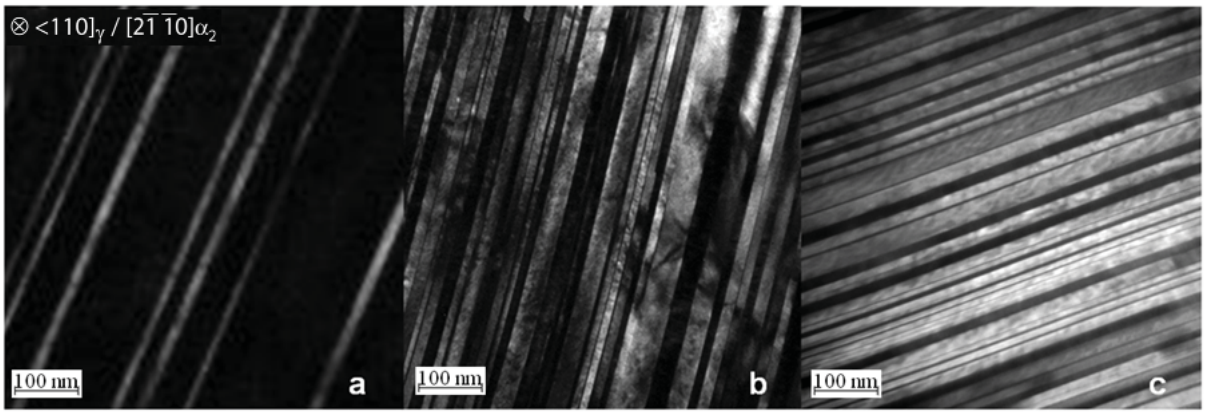

Fig. 56: TEM-images of α_2/γ-lamellae after heat treatments at 1230°C/1h/AC, 1230°C/1h/AC + 850°C/6h/FC and 1230°C/1h/AC + 950°C/6h/FC in a), b) and c) respectively [25].

γ-phase precipitates in the form of very fine lamellae within the α_2-grains in the course of the first heat treatment at 1230°C, as shown in Figure 56a. During the second heat treatment the γ-fraction increases at the expense of α_2 by the formation of further γ-lamellae, as can be seen for the second heat treatment at 850°C in Figure 56 b. At higher temperatures, i.e. in this case 900°C and 950°C for heat treatments 3 and 4, the amount and spacing of the γ-lamellae does not change considerably. The average interlamellar spacing is about 15 nm for specimens after the second heat treatment, as determined by Cha [25].

Those observations correspond to the model of the lamellae formation suggesting that lamellae coarsening is insignificant at low aging temperatures and that at higher temperatures the formation of few more fine γ-lamellae takes place, as described by Cha et al. [53]. A model is drafted in Figure 57.

Fig. 57: Model of lamellar colony formation in TNM-B1. After the first heat treatment few fine γ-lamellae can be found in the α_2-grains. During the second heat treatment more γ-lamellae nucleate. The interlamellar spacing does not change considerably for higher temperatures in the second heat treatment. The only difference between T_2 and T_3 is the higher volume fraction of γ at T_3.

A decrease in interlamellar spacing usually causes an increase in hardness. Vickers hardness measurements with a load of 5 kg were therefore performed on samples in the four heat treatment states. The results are displayed in Figure 58.

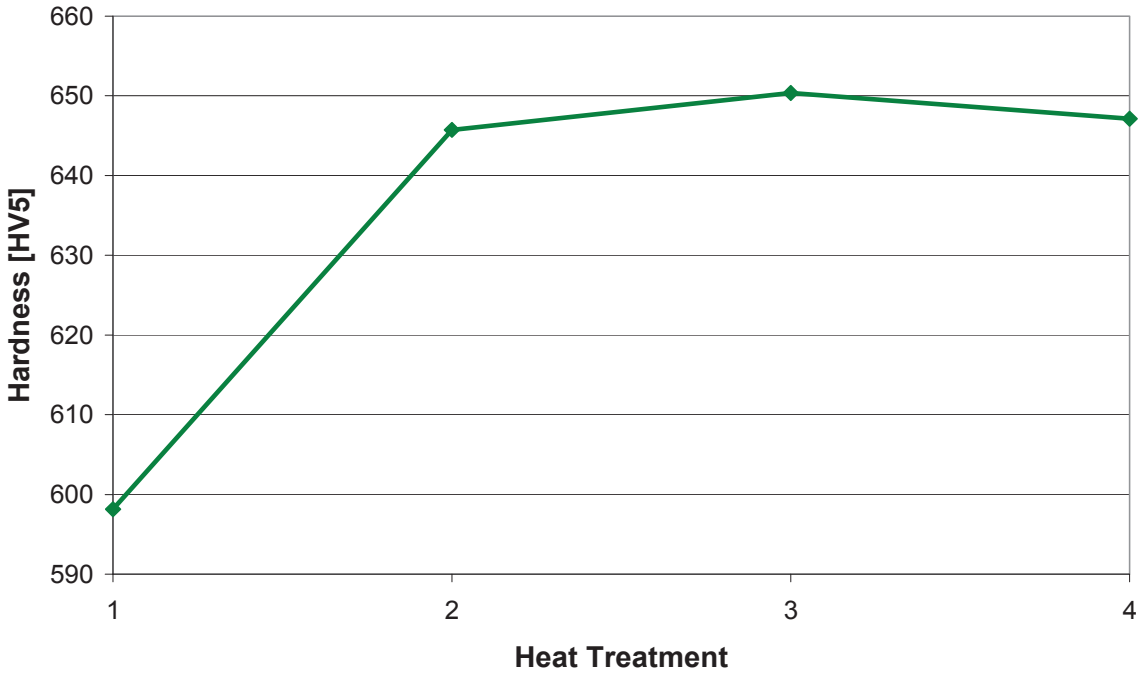

Fi

Fig. 58: Vickers hardness (HV5) against heat treatments as listed in Table 4. The hardenss is considerably higher for the materials after a two-step heat treatment, where fine γ-lamellae precipitate in the α_2-grains in heat treatments 2, 3 and 4.

A comparatively high increase in hardness can be observed from heat treatment 1 to 2, that goes along with a high increase in γ-phase in the form of fine lamellae, as can be seen from the XRD-scans and the TEM-micrographs (see Figs. 55 and 56). It is well known that the strength of γ-TiAl-based alloys with lamellar microstructure is determined by the occurring lamellar spacing [53]. The hardness varies only slightly for the heat treatments 2 to 4, corresponding to the almost constant average lamellar spacing. The small decrease in hardness for heat treatment 4 can be ascribed to the presence of a fair amount of areas transformed via a discontinuous precipitation. Figure 59 shows SEM-micrographs of the material in the four heat treatment states.

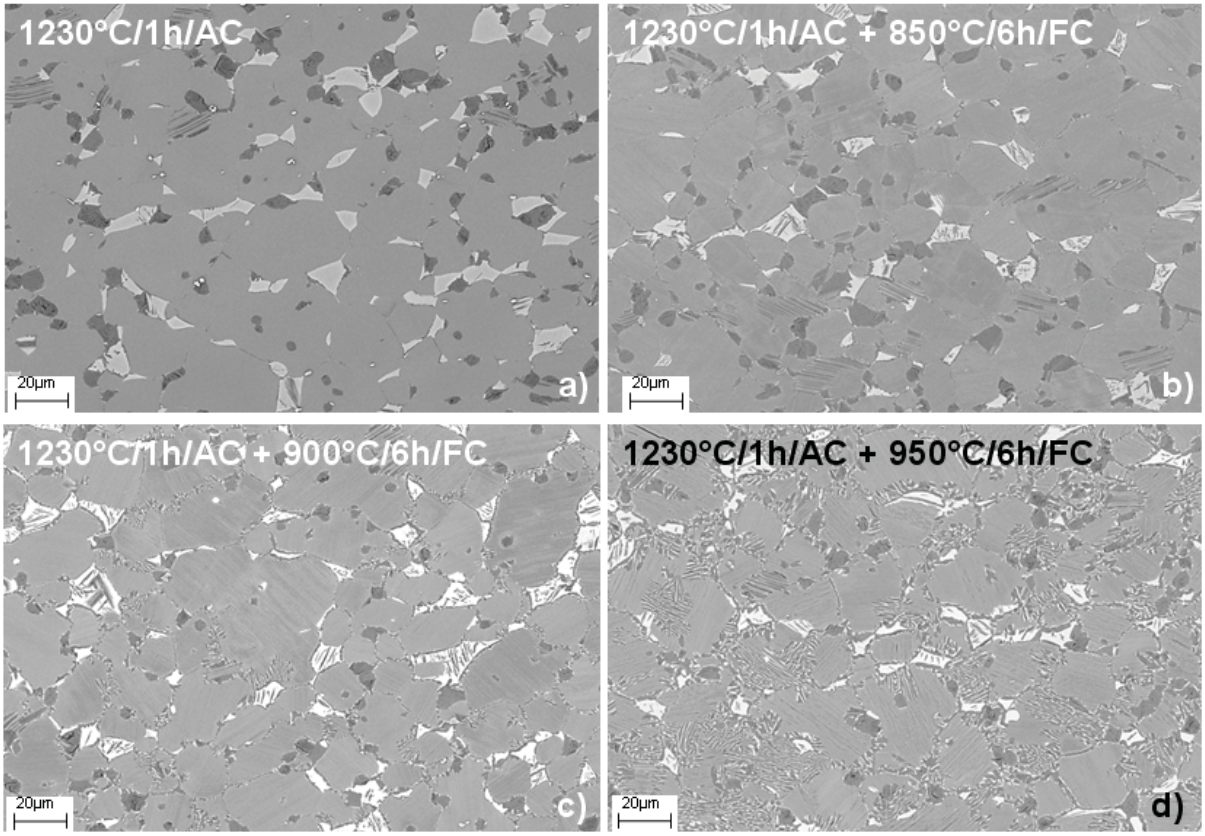

Fig. 59: SEM micrographs of the TNM alloy after the four different heat treatments (see Table 4) show different extents of microstructure transformed via discontinuous precipitation. All images were taken in BSE mode.

Figure 59a mainly shows oversaturated α_2-grains surrounded by β_O- and γ-grains. After heat treatment # 2 at 850°C for 6 h discontinuous precipitation is triggered at the grain boundaries. The fraction of the microstructure transformed via discontinuous precipitation increases with increasing temperature of the second heat treatment and is more advanced for heat treatments # 3 and # 4 (see Figs. 59c and d).

The increased tensile ductility (see Table 5) is therefore ascribed to the increasing extent of transformed microstructure after the second heat treatment. The influence of the prevailing β-phase on the observed tensile ductility at room temperature seems to be insignificant since the volume fraction remains almost the same after the different heat treatment steps.

6 Summary and Outlook

The starting point for this work, investigating variants of newly developed TNM alloys, were thermodynamic calculations conducted by Chladil [3]. Several methods were used to verify those predictions and to further characterize the material. DSC measurements performed by Böck [8] had already indicated that the eutectoid temperature calculated for the TNM alloy was too low. The same finding was obtained in the present work.

For a first comparison heat treatments were performed on the alloys on which thermodynamic calculations had been performed. SEM micrographs of heat treated samples were analyzed quantitatively regarding the β-phase volume fraction. The results confirmed the trend found in the calculations, though exact temperatures were hard to determine due to the small number of data points. An exception was the eutectoid temperature, which was denoted to be higher than calculated. It was proved, as predicted by Chladil, that the β-content in the material increases with increasing Nb and Mo contents and that Mo is a stronger β-stabilizer than Nb.

For further determination of the evolution of the phase fractions as a function of temperature, in-situ experiments were performed at the ESRF in Grenoble. The obtained data were evaluated quantitatively through the Rietveld method for selected temperatures from 800°C to 1300°C, leading to the determination of T_α and T_{eu}. Due to inaccurate temperature control during the experiment the temperature scale had to be adjusted using experimental results from neutron diffraction obtained by Liss et al. [42]. T_α, that had been predicted at ca. 1264°C by thermodynamic calculations was experimentally found to lie between 1260°C and 1265°C by Rietveld analyses of in-situ synchrotron data. The α_2-superstructure peaks disappeared between 1150°C and 1170°C during neutron diffraction, so T_{eu} lies within this temperature range. A comparison of the course of the β-phase with temperature for the investigated alloys showed the same trend as the thermodynamic calculations as well as the quantitative analyses performed on the SEM micrographs after heat treatments. Higher Nb and Mo-contents increase the β-volume fraction and the temperature of the β-minimum.

Due to the large difference in neutron scattering lengths of Ti and Al, order transition temperatures can be determined by neutron diffraction experiments. Since the recording of one pattern is time consuming, only selected temperatures were investigated. T_α was determined to lie between 1100°C and 1200°C, $\beta \rightarrow \beta_O$ was found to lie between 1200°C and 1250°C, a lot lower than originally predicted above 1400°C. Those results are in accordance with results elaborated by Liss et al. [42].

Quantitative Rietveld analyses of the neutron diffraction data accord with the results from the synchrotron experiments.

A cellular reaction, also known as discontinuous precipitation (DP), takes place in the α_2+γ-colonies at certain heat treatments. This reaction could be observed in SEM micrographs. DP starts at lamellar colonies containing oversaturated α_2. In a first heat treatment step the β-content is reduced to a minimum. Due to the annealing temperature at T_α a large amount of oversaturated α is produced during this heat treatment. The second heat treatment steps were performed at different temperatures to describe the progress of the DP. First evidence of the DP could be found for a heat treatment at 900°C after 1 h. The amount of microstructure transformed via the DP increases with time and temperature. After 100 h at 1100°C the cellular reaction is virtually completed and the microstructure is composed of globular grains. Long term heat treatments at 800°C performed by Wallgram [13] showed no indication of discontinuous precipitation even after 3000 h.

For a more detailed study of these microstructural transformations EBSD measurements were performed. As described in the literature, the Blackburn orientation relationship between the α_2 and γ lamellae persists through the DP and could be detected between the secondary lamellae. γ-particles that precipitate within the β_O-grains exhibit a special orientation relationship with the β_O-grains they emerge from, showing parallel aligned close packed lattice planes. In areas where α_2, γ and β_O form during the DP all the close packed planes are aligned in parallel direction to each other.

Before a cellular reaction occurs upon heating in a sample containing oversaturated α_2-grains, the precipitation of extremely fine γ-lamellae can be observed. Heat treatments between 850°C and 980°C for 6 h were performed on such samples. TEM micrographs showed that with increasing temperature the lamellae coarsen only insignificantly and the precipitation of further γ-lamellae is nucleated. The interlamellar spacing of the primary lamellae is almost the same for the samples annealed between 850°C and 950°C for 6 h. The only difference is the volume fraction of the γ-phase which is the highest at 950°C. Hardness measurements confirmed these findings showing an increased hardness after a second heat treatment. The influence of the prevailing β-phase on the observed tensile ductility at room temperature seems to be insignificant because the volume fraction remains almost the same after the different heat treatment steps.

Further TEM investigations of the α_2+γ-colonies are in progress and thus not included in this work. Those investigations aim at verifying the model of lamellae formation within oversaturated α_2-grains upon heating and the onset of DP. For more

detailed information on the lamellae formation in-situ experiments will have to be performed and evaluated. Additional TEM and XRD measurements can also give further evidence whether ω is present in TNM alloys or not.

7 References

[1] H. Kestler, H. Clemens, editors: M. Peters, M. Leyens, Titanium and Titanium Alloys, Weinheim Wiley-VCH (2003) p. 351.
[2] H. Clemens, W. Wallgram, S. Kremmer, V. Güther, A. Otto, A. Bartels, Design of novel β-solidifying TiAl Alloys with adjustable β/B2-Phase Fraction and excellent Hot-Workability, Advanced Engineering Materials (2008) 10, No.8.
[3] H.F. Chladil, Entwicklung und Charakterisierung von hoch Niob-haltigen γ-Titanaluminid Legierungen, PhD thesis, Montanuniversität Leoben, Austria (2007).
[4] R.M. Imayev, V.M. Imayev, M. Oehring, F. Appel, Alloy Design Concepts for refined Gamma Titanium Aluminide based Alloys, Intermetallics 15 (2007) 451-460.
[5] F. Appel, U. Brossmann, U. Christoph, S. Eggert, P. Janschek, U. Lirenz, J. Müllauer, M. Oehring, J.D.H. Paul, Recent Progress in the Development of Gamma Titanium Aluminide Alloys, Advanced Engineering Materials 11 (2000) 699-720.
[6] U. Brossmann, M. Oehring, U. Lorenz, F. Appel, H. Clemens, Evolution of the Microstructure during Hot Working of γ-based TiAl Alloys, Zeitschrift für Metallkunde/Materials Research and Advanced Techniques, 92 (2001) 8, 1009-1014.
[7] H. Clemens, H.F. Chladil, W. Wallgram, G.A. Zickler, R. Gerling, K.-D. Liss, S. Kremmer, V. Güther, W. Smarsly, In and ex situ Investigations of the β-Phase in a Nb and Mo containing γ-TiAl Based Alloy, Intermetallics 16 (2008) 827-833.
[8] B. Böck, Untersuchung und Verifizierung des quasibinären Zustandsdiagramms für β-erstarrende TNM-Legierungen auf Basis von Ti-(41-45)Al-4Nb-1Mo-0.1B, Diploma thesis, Montanuniversität Leoben (2008).
[9] H. Clemens, H.F. Chladil, W. Wallgram, B. Böck, S. Kremmer, A. Otto, V. Güther, A. Bartels, A β-stabilized γ-TiAl based Alloy for improved Processing Performance, Structural Aluminides for Elevated Temperatures, eds. Y.W. Kim, D. Morris, R. Yang, C. Leyens (New Orleans, LA. TMS 2008), 217-228.
[10] S.R. Dey, E. Bouzy, A. Hazotte, EBSD Characterization of massive γ Nucleation and Growth in a TiAl-based Alloy, Intermetallics 14 (2006) 444-449.
[11] M.J. Blackburn, The Science, Technology and Application of Titanium Alloys, eds. R.I. Jaffee, N.E. Promisel, Plenum Press New York (1970) 633.
[12] N. Saunders, Gamma Titanium Aluminides 1999, eds. Y-W. Kim, D.M. Dimiduf, M.H. Loretto (Warrendale, PA: TMS 1999), 183-194.
[13] W. Wallgram, Charakterisierung einer β-erstarrenden γ-Titanaluminid Basislegierung für Strahltriebwerksanwendungen, Diploma thesis, Montanuniversität Leoben, Austria (2008).

[14] S. Mitao, L.A. Bendersky, Morphology and Growth Kietics of discontinuous Coarsening in fully lamellar Ti-44Al (at%) Alloy, Acta Materialia 45 (1997) 11, 4475-4489.
[15] A. Denquin, S. Naka, Phase Transformation Mechanisms involved in Two-Phase TiAl-based Alloys - II. Discontinuous Coarsening and massive-type Transformation, Acta Materialia 44 (1996) 1, 353-365.
[16] K.-D. Liss, A. Bartels, H. Clemens, S. Bystrzanowski, A. Stark, T. Buslaps, F.-P. Schimansky, R. Gerling, C. Scheu, A. Schreyer, Recrystallization and Phase Transitions in a γ-TiAl-based Alloy as observed by ex situ and in situ high-energy X-ray Diffraction, Acta Materialia 54 (2006), 3721-3735.
[17] P.Zieba, W. Gust, Local Characterization of the Diffusion Process during Discontinuous Precipitaion: A Review, Zeitschrift für Metallkunde, 92 (2001) 7, 645-654.
[18] M. Talach-Dumanska, P. Zieba, A. Pawlowski, J. Wijewoda, W. Gust, Practical Aspects of discontinuous Precipitation and Dissolution, Materials Chemistry and Physics, 80 (2003), 476-481.
[19] D.A. Porter, K.E. Easterling, Transformations in Metals and Alloys, second Edition, Neslon Thornes Ltd (2001), 322-326.
[20] A. Denquin, S. Naka, Phase-Transformation Mechanisms in Two-Phase TiAl-based Alloys, eds. Y.-W. Kim, R. Wagner, M. Yamaguchi, (Las Vegas, NV. TMS 1995), 141-148.
[21] K.-D. Liss, A. Stark, A. Bartels, H. Clemens, T. Buslaps, D. Phelan, L.A. Yeoh, Directional atomic Rearrangements during Transformations between the α- and γ-Phases in Titanium Aluminides, Advanced Engineering Materials, 10 (2008) 4, 389-392.
[22] D.-H. Gosslar, Thermische Nachbehandlng walzharter TiAl-Bleche, Diploma thesis, Technische Universität Hamburg-Harburg (2007).
[23] G. Das, Pratt & Whitney, unpublished Results (2008).
[24] F. Appel, M. Oehring, J.D.H. Paul, Advanced Engineering Materials, 8 (2006) 371-376.
[25] L. Cha, Montanuniversität Leoben, unpublished Results (2008).
[26] A. Ide-Ektessabi, Application of Synchrotron Radiation. Micro Beams in Cell Micro Biology and Medicine, Springer, (2007), p. 1-7.
[27] A.L. Robinson, X-Ray Data Booklet, Center for X-Ray Optics advanced Light Source, Second Edition, (2001), p. 2.2-17.
[28] G. Margaritondo, Introduction to Synchrotron Radiation, Oxford University Press, (1988), p. 1-49.

[29] G.A. Zickler, H. Clemens, A. Schreyer: Werkstoffuntersuchung mit Synchrotronstrahlung, BHM, 152 (2007), Heft 9.
[30] W. Reimers, A.R. Pyzalla, A. Schreyer, H. Clemens (eds.), Neutrons and Synchrotron Radiation in Engineering Materials Science. From Fundamentals to Material and Component Characterization, WILEY-VCH, (2008), p. 79-112.
[31] W. Gudat, K. Sturm, M. Loewenhaupt, 18. IFF-Ferienkurs Synchrotronstrahlung in der Festkörperforschung 16.-27. März 1987, Kernforschungsanlage Jülich, (1987), p. 1.1-.26, 12.1-.62, 36.1-.18.
[32] G. Schatz, A. Weidinger, Nukleare Festkörperphysik, Teubner Studienbücher, (1997), p. 226-257.
[33] S.W. Lovesey, Theory of Neutron Scattering from condensed Matter, Volume 1, Oxford Science Publications, (2004), p. 1-33.
[34] G. Will, Powder Diffraction, Springer Berlin Heidelberg New York, (2006).
[35] R.A. Young, The Rietveld Method, Oxford University Press, (2000).
[36] R. Allmann, Röntgernpulverdiffraktometrie, Rechnergestützte Auswertung, Phasenanalyse und Strukturbestimmung, Springer Berlin Heidelberg New York, (2003).
[37] L.B. McCusker, R.B. Von Dreele, D.E. Cox, D. Louer, P. Scardi, Rietveld Refinement Guidelines, Journal of Applied Crystallography, 32 (1999) 36-50.
[38] G. Caglioti, A. Paoletti, F.P. Ricci, Choice of Collimators for a crystal Spectrometer for neutron Diffraction, Nuclear Istruments 3, (1958) 223-228.
[39] G. Faninger, U. Hartmann, Physikalische Grundlagen der quantitativen röntgenographischen Phasenanalyse (RPA), HTM 27 (1972).
[40] S.G. Eeckhout, B. Gorges, L.Barthe, O. Pelosi, O. Safonova, G. Giuli, A high-temperature Furnace for in situ Synchrotron X-ray Spectroscopy under controlled atmospheric Conditions, Journal of Synchrotron Radiation, 15 (2008) 1-6.
[41] M. Hoelzel, A. Senyshyn, R. Gilles, H. Boysen, H. Fuess, The Structure Powder Diffractometer SPODI, Neutron News, 18, 4 (2007) 23-26.
[42] K.-D. Liss, I. Watson, Australian Nuclear Science and Technology Organisation, unpublished Results (2008).
[43] A. Stark, Technische Universität Hamburg-Harburg, unpublished Results (2008).
[44] V. Randle, O. Engler, Introduction to Texture Analysis Macrotexture, Microtexture and Orientation Mapping, Gordon and Breach Science Publishers, (2000), p. 3-12, 125-145, 153-188.
[45] M. von Heimendahl, Einführung in die Elektronenmikroskopie, Vieweg, Braunschweig (1970).
[46] Electron Backscattered Diffraction, Oxford Instruments Analytical - technical Briefing.

[47] K. Dicks, An Introduction to EBSD - the Technique and Applications, EBSD Workshop Dept. Metallkunde und Werkstoffprüfung der Montanuniversität, Leoben, Oxford Instruments Analytical, (2004).
[48] N.C.K. Lassen, D.J. Jensen, K. Conradsen, Image processing Procedures for Analysis of Electron back scattering Patterns, Scanning Microscopy, 6 (1992) 115.
[49] K. Kunze, S.I. Wright, B.L. Adams, D.J. Dingley, Textures and Microstructures, 20 (1993) 41.
[50] S. Zghal, S. Naka, A. Couret, A quantitative TEM Analysis of the lamellar Microstructure in TiAl based Alloys, Acta Materialia 45 (1997) 7, 3005-3014.
[51] S.R. Dey, A. Morawiec, E. Bouzy, A. Hazotte, J.J. Fundenberger, A Technique for Determination of γ/γ Interface Relationships in a (α_2+γ) TiAl base Alloy using TEM Kikuchi Patterns, Materials Letters 60 (2006) 646-650.
[52] A. Denquin, S. Naka, Phase Transformation Mechanisms involved in two-phase TiAl-based Alloys – I. Lamellar Structure Formation, Acta Materialia 44 (1996) 1, 343-352.
[53] L. Cha, C. Scheu, H. Clemens, H.F. Chladil, G. Dehm, R. Gerling, A. Bartles, Nanometer-scaled lamellar Microstructures in Ti-45Al.7.5Nb-(0;0.5)C Alloys and their Influence on Hardness, Intermetallics 16 (2008) 868-875.
[54] T.T. Cheng, M.H. Loretto, The Decomposition of the Beta Phase in Ti-44Al-8Nb and Ti-44Al-4Nb-4Zr-0.2Si Alloys, Acta Materialia 46, 13 (1998) 4801-4819.